EXPERIMENTAL STUDY OF SHOCK-DRIVEN, VARIABLE-DENSITY TURBULENCE USING A COMPLEX INTERFACE

A Thesis
Presented to
The Academic Faculty

by

David Reilly

In Partial Fulfillment
of the Requirements for the Degree
Master of Science in the
Woodruff School of Mechanical Engineering

Georgia Institute of Technology
December 2015

EXPERIMENTAL STUDY OF SHOCK-DRIVEN, VARIABLE-DENSITY TURBULENCE USING A COMPLEX INTERFACE

Approved by:

Dr. Devesh Ranjan
Woodruff School of Mechanical Engineering
Georgia Institute of Technology

Dr. Sheldon Jeter
Woodruff School of Mechanical Engineering
Georgia Institute of Technology

Dr. Paul Neitzel
Woodruff School of Mechanical Engineering
Georgia Institute of Technology

Dr. Jacob McFarland
Mechanical and Aerospace Engineering
University of Missouri

Date Approved: November 16, 2015

This thesis is dedicated to my sister, Allison Reilly, for without her guidance and support early in life I would not be where I am today.

ACKNOWLEDGEMENTS

There have been many people who have helped me to succeed in graduate school while I was pursuing my Master's degree. First is my graduate advisor, Dr. Devesh Ranjan, who was never too busy to talk through an idea with me, no matter how late at night. He showed commitment in developing me as a student even as I interned in the laboratory as an undergraduate student during an REU program. He taught me how to see issues from alternative perspectives and effectively communicate my ideas to others. His advice will serve me well for years to come. I would also like to thank Dr. Jacob McFarland, who was like a second advisor to me. He designed and built the inclined shock tube facility and taught me almost everything I know about it. Thank you to all of my committee members for reviewing my work and giving me advice.

I would like to thank all of my lab mates at Georgia Tech for working long hours in the lab with me and also helping me to have fun along the way. I extend a special thanks to John Carter for his diligence in developing our PLIF correction codes. He was the most committed student I worked with during my graduate studies. Mohammad Mohaghar contributed greatly to our notch filtering code and helped with several experiments. Vladimer Tsiklashvili helped me with gas dynamics codes as well as with theoretical understanding of hydrodynamic instabilities. Whenever I needed help when I was writing my thesis, or with any problem, I could always rely for Stephen Johnston for help.

At Texas A&M University there were several more students who I both enjoyed working with and learned much from. Dr. Bhanesh Akula and Dr. Sarat Kuchibhatla both

have deep understandings of fluid mechanics and were always willing to spend time to teach me. Sarat was my "go-to person" for both LaTex and Matlab. Skylar Creel helped me with many experiments and helped me with the logic involved in writing Matlab codes. He also expanded my taste in music. Chris McDonald helped me learn the basics of operating the shock tube when I was still an undergrad in the lab. Chris is a great leader and communicator. I have great respect for him and believe he will go far in life.

Dr. Ricardo Mejia-Alvarez from Los Alamos National Laboratory was a key part of the proper orthogonal decomposition analysis presented in this work. He was always willing to provide expert feedback on any issues our lab had.

Lastly, I would like to thank all of the undergraduate researchers who helped conduct experiments and design facility upgrades. Brandon Conner, Debapriya Bhattacharjee, and Cody Huggins all allowed this work to be more productive. A special thanks to Cody for his excellent work in designing and manufacturing our dual-plane calibration plate used for simultaneous PLIF and stereo PIV.

TABLE OF CONTENTS

LIST OF TABLES

LIST OF FIGURES

NOMENCLATURE

A	Atwood number
a	Turbulent mass flux
b	Density self-correlation
$\vec{B}$	Body forces
c	Speed of sound in the medium
k	Wavenumber
k_y	Wavenumber in spanwise direction
M	Mach number
R	Gas constant
T	Temperature
t	Time
u'	Streamwise velocity fluctuation
v'	Spanwise velocity fluctuation
w_i	Incident shock wave speed
η	Amplitude of perturbation

λ	Wavelength of perturbation
θ	Angle of inclination
Γ	Circulation
$\vec{\omega}$	Vorticity
γ	Ratio of specific heats
ρ_h	Density of heavy gas
ρ_l	Density of light gas
τ	Nondimensionalized time

SUMMARY

The overarching goal of this work is to advance the current knowledge of hydrodynamic instabilities (namely, Richtmyer-Meshkov and Kelvin-Helmholtz instabilities) and associated turbulent mixing phenomena which is important for several emerging technologies and verification/validation of numerical models being developed to study these phenomena. Three experimental campaigns were designed to focus on understanding the evolution of the instability under different impulsive acceleration histories and highlight the impact of initial conditions on the developing turbulent flow environment. The first campaign highlights the importance of initial baroclinic torque distribution along the developing shocked interface in a twice-shocked variable-density flow environment. The second campaign is a parametric study which aims at providing a large dataset for validating models in literature as well as simulations. In the last study, a new type of initial condition was designed to study the effect of initial conditions on late time turbulent flows. A description of the optical diagnostic techniques developed in our laboratory in order to complete these studies will be given. Now each campaign will be introduced.

In the first campaign, an inclined interface perturbation is used as the initial condition. The Mach number (1.55), angle of inclination (60^o), and gas pair (N_2/CO_2) were held constant. The parameter which changed was the distance that the initial condition was placed relative to the end of the shock tube (i.e., the end of the test section). Three distances were used. The vorticity distribution was found to be very

different for the most developed case after reshock. Furthermore, the most developed case started to develop an inertial range before reshock.

The second campaign is parametric and seeks to test a proposed inclined interface scaling technique. The data is also useful for comparing to Ares simulation results. The parameter space covered Mach number (1.55 and 2.01), inclination angle (60^o and 80^o), and Atwood number (0.23 and 0.67). PLIF was developed and used to collect data for four cases before and after reshock. Linear and nonlinear cases developed very differently before reshock, but their mixing widths converged after reshock.

The last campaign involves a new perturbation technique which generates what will be referred to as a complex interface. Counter-flowing jets were placed near the interface exit ports to create shear. The perturbation was made more complex by also injecting light (heavy) gas into the heavy (light) one. Density and velocity statistics were collected simultaneously. The complex case retained a signature of the inclined interface perturbation at late time before reshock and developed a larger inertial range than its inclined interface counterpart. Important parameters for a variable-density turbulence model are also presented.

CHAPTER 1: Background

INTRODUCTION

The overarching goal of this work is to advance the current knowledge of hydrodynamic instabilities (namely, Richtmyer-Meshkov and Kelvin-Helmholtz instabilities) and associated turbulent mixing phenomena which is important for several emerging technologies and verification/validation of numerical models being developed to study these phenomena. Three experimental campaigns were designed to focus on understanding the evolution of the instability under different impulsive acceleration histories and highlight the impact of initial conditions on the developing turbulent flow environment. The first campaign highlights the importance of initial baroclinic torque distribution along the developing shocked interface in a twice-shocked variable-density flow environment. The second campaign is a parametric study which aims at providing a large dataset for validating models in literature as well as simulations. In the last study, a new type of initial condition was designed to study the effect of initial conditions on late time turbulent flows. An overview of the optical diagnostic techniques developed in our laboratory in order to complete these studies will be discussed.

The first study is related to inertial confinement fusion (ICF) which has the potential to provide a long-lasting supply of clean energy on a global level. As will be discussed in more detail in the next section, there are three hydrodynamic instabilities which occur in ICF. Researchers are currently trying to determine if these instabilities are responsible for limiting the energy yield from ICF. Two of those instabilities will be studied to see how development affects vorticity deposition after reshock.

The second study is important for models which have been developed in an attempt to scale data from the experimental facility used in this work. A parametric experimental study has been conducted which can be used to validate this model. Furthermore, simulations have been conducted using the same conditions as those chosen for the experiments, so the agreement between the two can be determined.

The third study and main focus of this work could potentially lead to a paradigm shift in this field of fluids research. In supersonic combustion applications, such as in a scramjet engine, shock-driven compressible mixing is important for efficient mixing of the fuel and oxidizer. If possible, it would be beneficial if turbulence could be designed in order to enhance this mixing. The traditional view is that the signature of initial conditions is lost (loss of memory) after turbulence develops to a universal end state. However, recent work at Los Alamos National Laboratory (LANL) suggests that the signature of the initial condition persists in turbulent flows at late time [1]. Our laboratory collaborated with LANL on a water channel experiment where this hypothesis was tested. Figure 1 shows how the wavelengths present in the initial condition dominate the mixing process at late time. The present study will begin to test this hypothesis in a shock-driven environment (non-Boussinesq) using the inclined shock tube facility at Georgia Institute of Technology. The hypothesis is that initially seeded, small-amplitude, long-wavelength perturbations persists in the flow field at late time in shock-driven flows and be used to control turbulence transport and material mixing. To test this hypothesis, two overarching goals must be met; the first to understand the impact of initial conditions on energy deposition in shock-driven flows; and the second to evaluate how initial conditions affect intermediate to late-time mixing. Completing these goals is of primary interest to

multiple research groups but is beyond the scope of this work. Progress will be made in achieving these goals through the design of a new experiment and the development of required diagnostics.

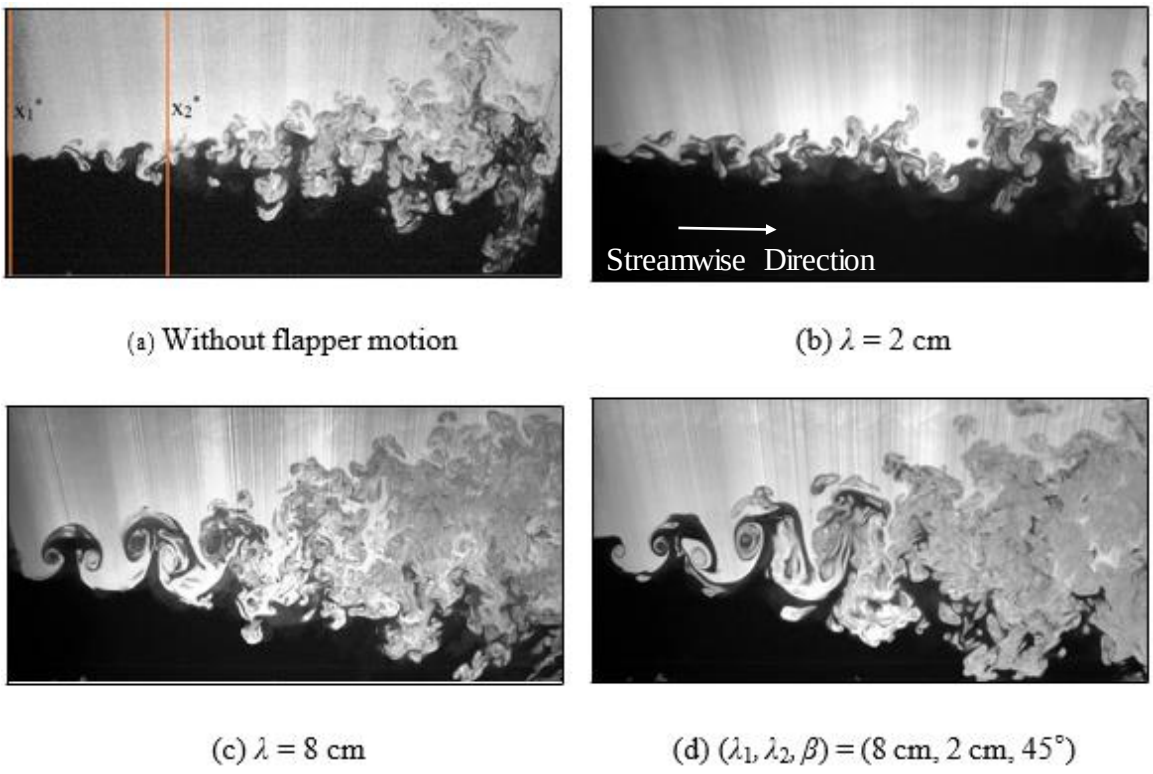

Figure 1: Water channel experiments showing that initial conditions with long wavelengths dominating the overall growth and evolution of the interface. Wavelengths measured in the streamwise direction and angles measured relative to the horizontal.

1.1 Applications of Shock-Driven Mixing

1.1.1 Inertial Confinement Fusion

The introduction to this section began with a few applications for shock-driven mixing, but there are many more applications which broadly fall under the category of shock-driven mixing (this class of problems will later be defined as the Richtmyer-Meshkov instability). One important application is inertial confinement fusion (ICF) which is being studied at the National Ignition Facility housed at Lawrence Livermore National Laboratory. A fuel pellet only a few millimeters in diameter is placed in a gold hohlraum (Figure 2). The fuel (on the order of micrograms) is made of two hydrogen isotopes - tritium (^{3}H), with one proton and two neutrons, and deuterium (^{2}H), with one proton and one neutron. The fuel pellet is frozen and encapsulated in an inert ablative material (e.g., beryllium) prior to being placed in the hohlraum. The hohlraum is heated by 192 lasers operating at 0.35 μm wavelength which produce a peak energy of 1.8 MJ/beam [2]. The laser energy is absorbed by the hohlraum after which it is converted and emitted as x-rays. X-rays heat the outside of the DT (Deuterium-Tritium) fuel pellet rapidly, which causes the outside of the capsule to blow off and the formation of a spherical shock wave moving towards the center of the pellet. A spherical shock wave propagates inward to the center of the pellet, achieving rapid compression. Ideally, sufficient temperature and density (100,000,000 ^{o}C and 110 g/cm^3, which is 100 times the density of lead) will be achieved and a thermonuclear burn will result in an energy output many times larger than the laser energy input. However, in practice this is very difficult to achieve.

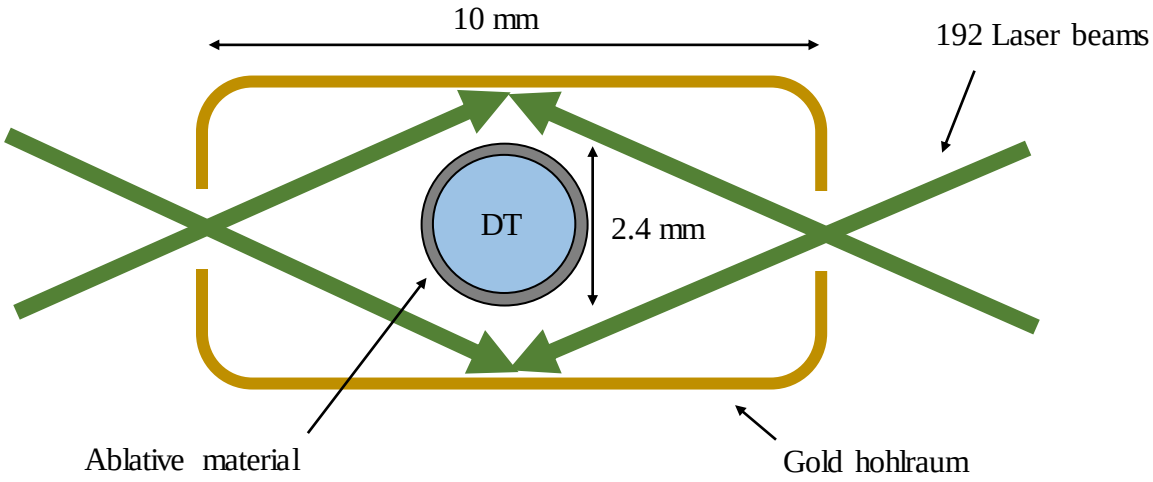

Figure 2: Diagram showing gold hohlraum holding deuterium-tritium (DT) fuel target about to be bombarded by 192 laser beams at the National Ignition Facility.

One of the aspects of the process which may be limiting the compression is the mixing between the ablative material and the DT fuel core as the shock wave passes through the imperfect, rough interface between them. Laser-plasma instabilities can also limit NIF yield as shown in Figure 3. Additional mixing will occur when the shock wave reflects off itself at the center of the core and passes through the material interface a second time (referred to as "reshock") as it leaves the fuel pellet. The hydrodynamic instability responsible for this mixing is the focus of this work.

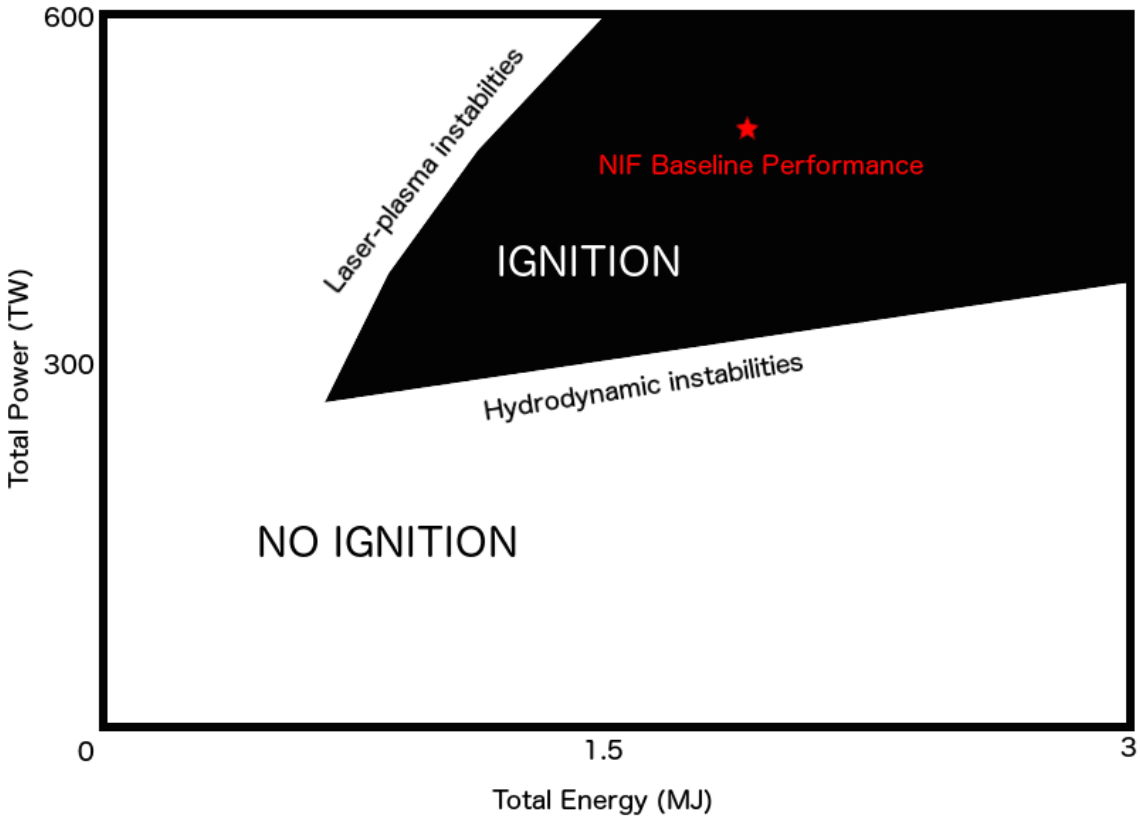

Figure 3: Expected performance of NIF at the time of its design. The performance specifications (red star) were achieved, but the simulations used to compute the black area were proven incorrect by eventual NIF experiments [3].

Another application of shock-driven mixing is the supernova which is an exploding star — a star violently dies when the nuclear fuel at the its core is depleted. The sudden initiation of the explosion can either occur from a rapid re-ignition of the nuclear fusion process or a gravitational collapse in a sufficiently large star. One of the first observed and recorded supernovae was seen by Johannes Kepler in 1604 in the Milky Way galaxy [4]. Although there have been no other supernovae observed in the Milky Way galaxy since Kepler's time, others have been documented in neighboring galaxies, the brightest being in 1987. These celestial events which last between several weeks to months release an enormous amount of energy, over 10^{21} times the amount of

energy that the Sun releases every second [4]. During the explosion, radiation ejects all of the star's material into the surrounding interstellar medium at speeds up to 10% of the speed of light, which leads to the formation of a shock wave [5]. As the shock wave propagates through interstellar space (Figure 4), it passes through variable-density compressible materials and generates mixing. This mixing is generated by the hydrodynamic instability investigated in this work. One of the reasons this phenomenon is of interest to scientists is that this shock-driven mixing and ejection of mass due to the vortex motion can lead to the formation of new stars.

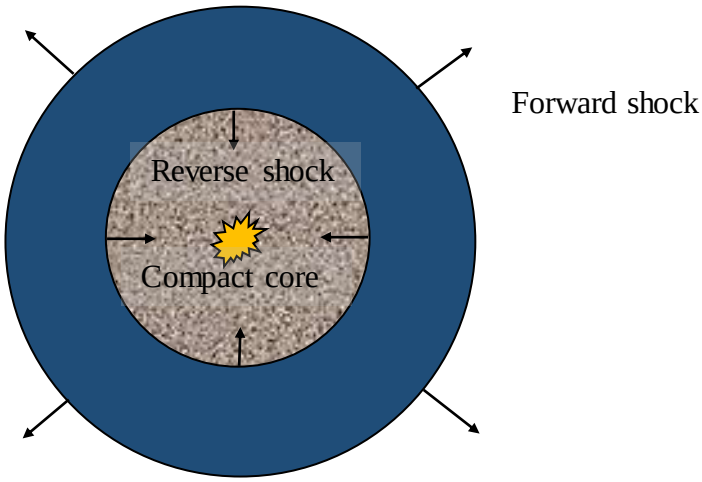

Figure 4: Major parts of a supernova including the forward and reverse shocks and compact core.

1.1.3 Scramjet Engine

An application which was alluded to earlier was the scramjet engine. This is perhaps the most relevant application for the specific research done in this work on the complex material interface. Scramjets is a supersonic combustion ramjet engines used in aircraft that travel at supersonic speeds; theoretical top speeds have been calculated to be

between Mach 12 and Mach 24 [6]. As shown in Figure 5, a scramjet consists of three main sections: (1) an inlet where supersonic compression occurs, (2) fuel injectors and flame holders where combustion occurs, and (3) a nozzle to eject the supersonic exhaust. Since the exhaust is supersonic, the nozzle is actually expanding, unlike subsonic nozzles. Air enters through the inlet and passes through a series of standing shocks before mixing with the fuel. The hydrodynamic instability studied in this work is important for understanding the mixing phenomenon in these geometry which can provide homogenous distribution of oxidizer and fuel in the combustion chamber. Turbulent mixing would be useful for enhancing the fuel/oxidizer mixing, but it is not known if it is possible to design this type of mixing. It is the goal of this work to determine if a signature of the initial condition persists to late time. If this can be shown, it may be possible to develop more efficient scramjet designs which make use of predictable turbulence.

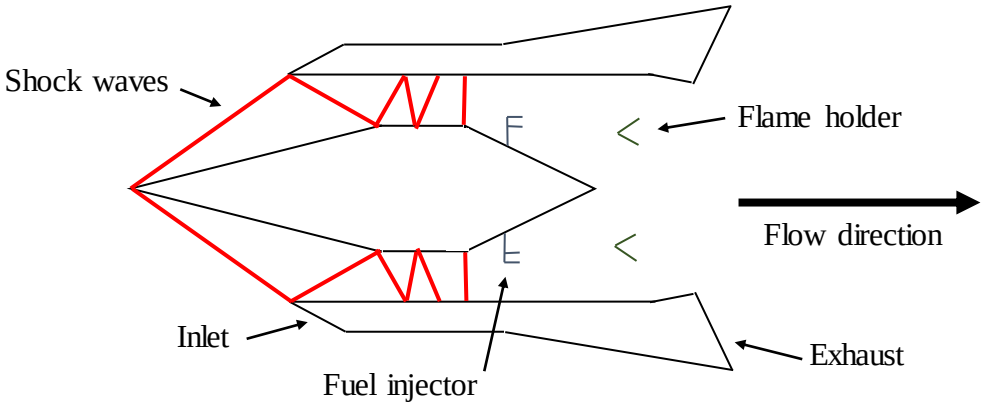

Figure 5: Scramjet/ramjet air intake and fuel injection system.

1.1.4 Other Applications

Other smaller, niche applications of the shock-driven hydrodynamic instability studied in this work were left to this section. One example from everyday life is shaking sauce out of a bottle [7]. An impulsive acceleration is created when a person taps the

back of the bottle which helps initiate the fluid flow. A very useful application of this research is needleless vaccine delivery using micro-shock waves [8]. Small mechanical devices are used to generate a micro-shock wave which carries the vaccine through the epidermis of the patient's body. These devices have the advantage of being both sterile and economical for deployment in third-world countries. The greatest benefit of all is that this needleless delivery device can deliver the vaccine at a more shallow depth under the skin compared to a needle, and therefore less of the vaccine is required to achieve the same concentration in the bloodstream. The dermis and epidermis in humans are rich in antigen-presenting cells which make processing the vaccine much more efficient. Shock waves are also used in the medical field to fragment gallstones and kidney stones [9], [10], [11]. Shock waves are used in the oilfield services industry to locate reservoirs of oil/gas and to detonate explosives used to form perforations in rock formations [12]. A shock-driven instability has recently been used to estimate metal strength at very high strain rates [13].

1.2 Theory of the Richtmyer-Meshkov Instability

The Richtmyer-Meshkov instability (RMI) [14], [15] is part of a family of hydrodynamic instabilities which includes the Kelvin-Helmholtz instability (KHI) [16], [17] and the Rayleigh-Taylor instability (RTI) [18], [19]. The RMI can be viewed as the impulsive limit of the RTI, so it is helpful to examine the RTI first. The RTI (named after Lord Rayleigh and G.I. Taylor) forms when a heavy fluid is placed over a light as shown in Figure 6.

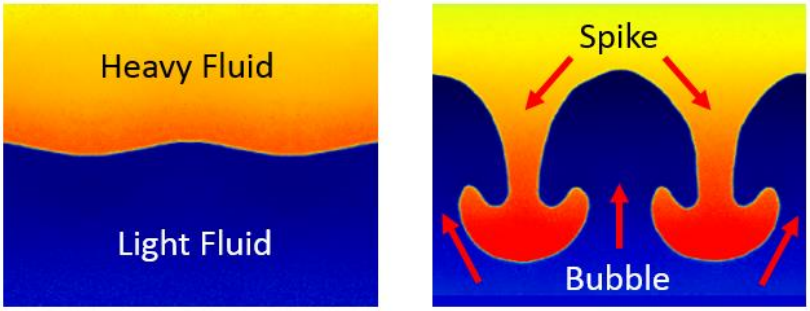

Figure 6: Single-mode Rayleigh-Taylor instability initial condition (left) and growth into mushroom structure (right). Adapted from v1.jmlab.jp.

The RTI occurs whenever a greater density fluid is placed over a smaller density fluid in a gravitational field. The necessary and sufficient condition for this instability is $\nabla p \cdot \nabla \rho < 0$, where ∇p is the pressure gradient and $\nabla \rho$ is the density gradient across the two fluid interface. Any small perturbations present at the two-fluid interface are unstable and grow in time. The pressure gradient is due to the gravitational acceleration which pulls the heavier fluid into the lighter fluid. When a heavy fluid is placed over a lighter fluid, the strength of the density gradient can be quantified using a non-dimensional number called the Atwood number. The Atwood number is

Equation 1

$$\boldsymbol{A = \frac{\rho_h - \rho_l}{\rho_h + \rho_l}}$$

where ρ_h is the density of the heavy fluid and ρ_l is the density of the light fluid. The strength of the gradient of pressure and density, as well as their level of misalignment, will determine the amount of vorticity deposited on the interface. This is explained by the vorticity equation (Equation 2)

Equation 2

$$\frac{D\vec{\omega}}{Dt} = (\vec{\omega}\cdot\nabla)\vec{u} - \vec{\omega}(\nabla\cdot\vec{u}) + \frac{1}{\rho^2}\nabla\rho\times\nabla p + \nabla\times\left(\frac{\nabla\cdot\tau}{\rho}\right) + \nabla\times\vec{B}$$

Vortex stretching (vel. gradient) | Vortex stretching (compressibility) | Baroclinic term | Viscous diffusion | Body forces

The first term on the right hand side of the equation explains how vorticity can be generated by stretching or tilting due to velocity gradients whereas the second terms explains how vorticity can be generated by stretching due to compressibility effects. The first term is essential for the discussion of three-dimensional turbulence and mixing. The vortex stretching and tilting is absent in two-dimensional flows. The second term is only important in the case of high Mach number experiments for highly compressible fluids. The third term is called the baroclinic term, and it describes how vorticity is produced when there is a misalignment between a density gradient and a pressure gradient. In the case of the RTI, the pressure gradient is provided by gravity. The fourth term describes how vorticity can be diffused due to viscous effects. Finally, body forces are included in the last term.

The Richtmyer-Meshkov instability is an impulsive limit of the Rayleigh-Taylor instability; in other words, the time scale for the pressure gradient has greatly reduced to the point that it is applied instantaneously. However, it should be noted, that the RMI induced turbulence will proceed irrespective of interface satisfying the $\nabla p\cdot\nabla\rho < 0$ criteria (whether it is heavy over light configuration or light/heavy configuration). This impulsive pressure gradient is generally provided by a shock wave, which is a type of

propagating pressure disturbance traveling faster than the speed of sound. The strength of the shock wave is quantified by a non-dimensional number called Mach number

Equations 3

$$\boldsymbol{M = W/c}$$

$$\boldsymbol{c = \sqrt{\gamma RT}}$$

where W is wave speed, c is the speed of sound of the medium through which the shock is propagating, γ is the ratio of specific heats, R is the gas constant, and T is the temperature. These equations are only valid for ideal gases. In the most general case, the speed of sound is defined as $c^2 = \left(\frac{dP}{d\rho}\right)_s$, where P is pressure, ρ is density, and s denotes that the derivative is taken with entropy held constant. A shock wave can be viewed as an extremely thin sheet. Its thickness has been estimated to be 200 nm, which is on the order of the free mean path of a gas molecule [20]. An example pressure trace showing an idealized instantaneous pressure jump at the location of the shock wave is shown in Figure 7.

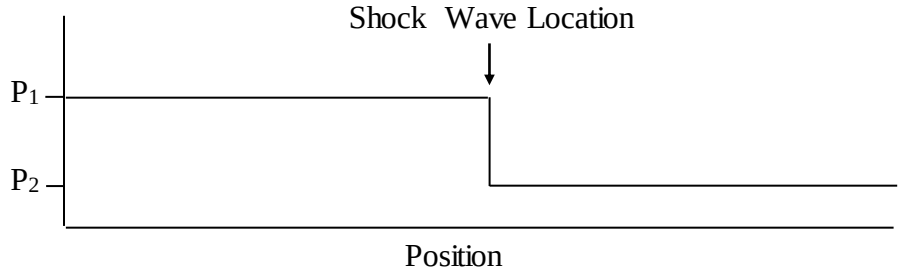

Figure 7: Pressure trace showing the location of a shock wave.

When a shock wave interacts with a misaligned density interface, the interface will become RM unstable. An example scenario of how this can occur is shown in Figure 8. A lighter fluid is placed over a heavier fluid to create a density gradient; the strength of

the density gradient is measured with the Atwood number the same as for the RTI. A shock wave travels through the interface, creating a pressure gradient. The two gradients have a non-zero angle between them. This will contribute to the baroclinic term highlighted in the vorticity equation (Equation 2). In the case where there is no misalignment between the gradients, no instability would result. The RMI is responsible for the initial vorticity deposition on the interface, but as the interface develops the shear between the two (or more) fluids may result in the formation of Kelvin-Helmholtz vortical structures, which can contribute to secondary vorticity deposition. The growth of these secondary structures is greatly influenced by the RTI.

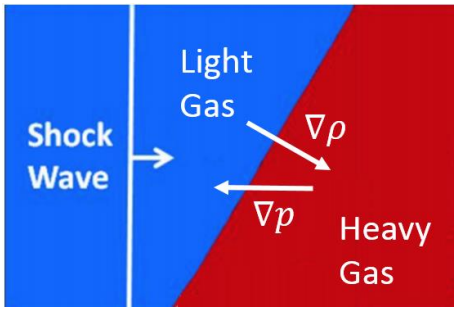

Figure 8: Shock wave impacting a density interface with pressure and density gradients shown.

An *x*-*t* plot is useful in tracking shock waves, contact surfaces, and refraction waves within a shock tube as well as estimating times for experiments (Figure 9). The horizontal axis represents distance along the length of the shock tube with zero occurring at the top of the driver. The diaphragm is located at the end of the driver (x = 1.53 m). When the diaphragm ruptures, an expansion fan travels into the driver while compression waves travel into the driven section. The contact surface between the driver and driven gases will also travel down the shock tube. When the shock wave impacts the interface dividing the two gases in the test section, part of the incident shock will reflect and part will transmit. The amount that will be reflected and transmitted is determined by the

acoustic impedance (ρc). The acoustic impedance is a thermodynamic property, and it is specific to the propagation medium. The acoustic impedance is a measure of the stiffness of a material, in the sense that it is the proportionality constant between impressed velocity and applied pressure (the usual elastic moduli however correspond to ρc^2). The transmitted shock wave will reflect off of the bottom of the shock tube and impact the evolving first-shocked interface for the second time (this process is generally referred to as reshock). Similar to the incident shock wave interaction with the interface, part of this shock wave will be transmitted and part will be reflected. Eventually, the expansion fan from the driver will make its way down to the interface in the test section. When this happens, the experiment is over because the purpose of these experiments is to study the flow dynamics associated with shocks passing through an interface, not expansion waves. The experiment time can be increased by increasing the length of the driver.

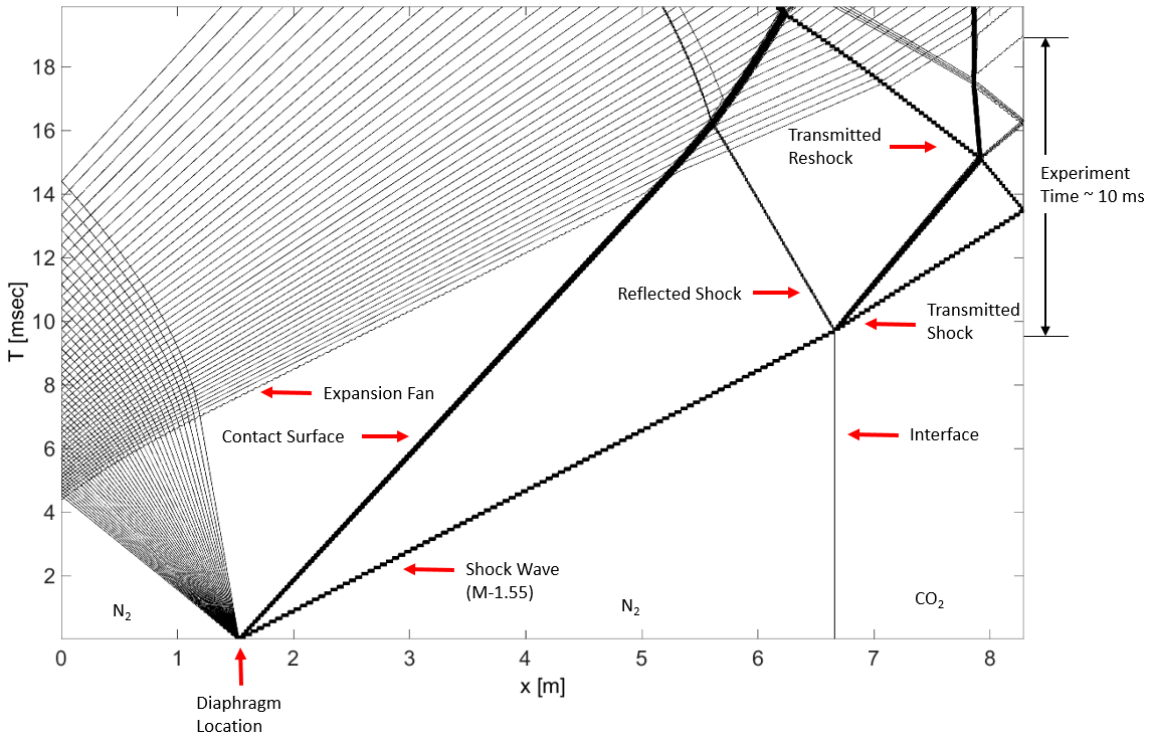

Figure 9: *x-t* diagram for inclined shock tube facility with features labeled. Code used to generate this plot was written by Vladimer Tsiklashvili.

An *x-t* plot can also be configured to display pressure. An example *x-t* plot showing pressure is shown in Figure 10. The driver and driven pressures at initial time are labeled as well as the pressure behind the incident shock and the pressure after reshock. The pressure after reshock is the highest pressure the test section is exposed to and is thus the pressure most often used for design purposes. All pressures are calculated using 1D gas dynamics and will therefore not be an exact match to the experiments which are not ideal and have some 2D and even 3D effects.

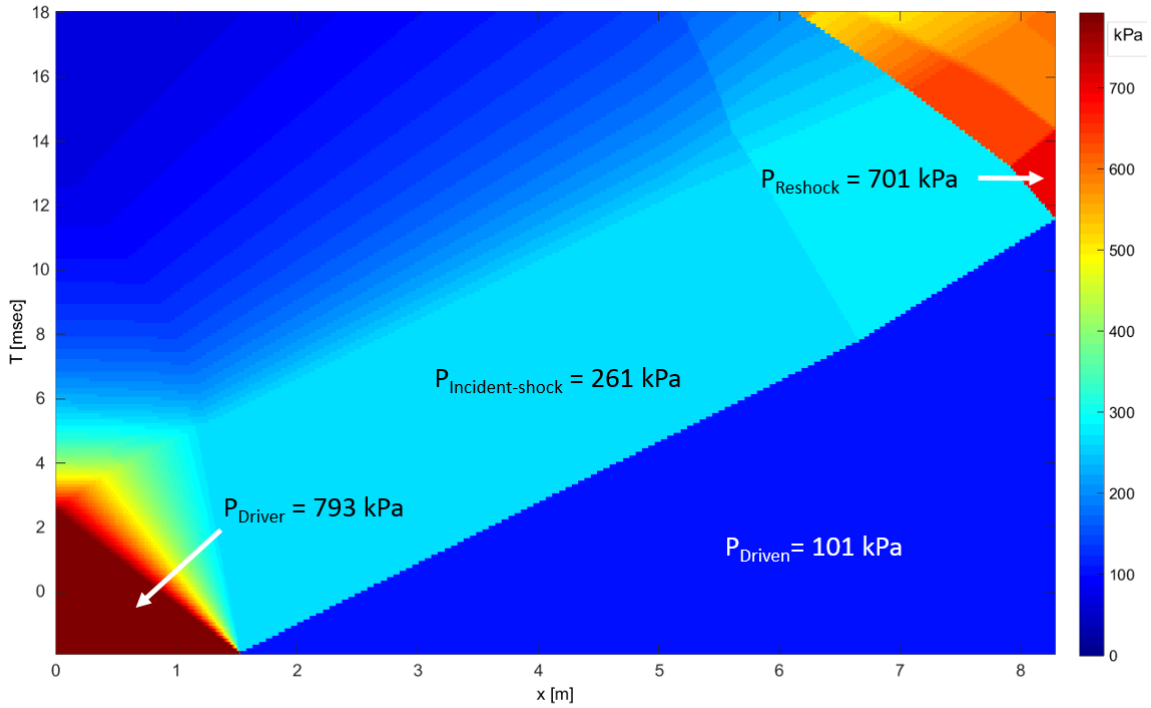

Figure 10: *x-t* plot for inclined shock tube facility configured to display pressure. This example uses *M*-1.55 and N_2 over CO_2. Code used to generate this plot was written by Vladimer Tsiklashvili.

1.3 Literature Review

In order to provide a background for the current research on the RMI presented in this thesis, a literature review of previous work will be provided. They are divided between experimental and theoretical/simulation works, although there is some overlap between the two. Experimental works are discussed first because experiments provide a basis for simulations and verifying theory. Without high-fidelity experiments, the appropriate boundary conditions cannot be determined and results cannot be validated. However, some of the theory was developed before experiments were performed. Even so, theory and simulations will be grouped together and discussed second for simplicity of presentation.

1.3.1 Experimental Works

This section will begin with a discussion of the first experiments which were critical to discovering and proving the existence of the RMI. Then a brief review of several of the experiments which have had the greatest impact on the field will be discussed. These will be divided up based upon the method used to drive the acceleration required for the RMI - the methods being (1) laser-driven, (2) mechanically-driven, or (3) shock-driven.

The Richtmyer-Meshkov instability was actually pre-discovered by Jahn [21] who experimentally studied the refraction of plane shock waves using an oblique density interface. However, the focus of the author's work was on the physics of shock-refraction and boundary layer development, and not the hydrodynamic instability developing on the gaseous interface. Therefore, the RMI was experimentally observed but not understood in 1956, thirteen years before the seminal experiments of Meshkov [15]. Meshkov was a Russian scientist, who in 1969 verified the theory for the RMI put forth by Richtmyer [14] nine years earlier.

More recently experiments have been conducted to study shock compression of a DT (Deuterium-Tritium) fuel capsule at Lawrence Livermore National Laboratory (LLNL). As discussed in the Applications section, several laser beams are used to drive the energy required to form a spherical shock wave which compresses the fuel capsule. Before the 3D spherical shock wave enters the fuel, it must pass through an ablative material which could be beryllium or some other inert material [22]. All three of the hydrodynamic instabilities mentioned in the Theory section occur during this process, including RMI [23], RTI [24], and KHI [25]; this, along with the small time scale and

high temperature (100,000,000 ^{o}C) and pressure (10 Mbar), make this a challenging experiment. The goal of this research is to increase the technical readiness of Inertial Confinement Fusion (ICF) so that it can be used as a clean, sustainable energy source.

Next, experiments which use mechanically-driven impulsive acceleration will be discussed. One such method was used by Jacobs' research group at the University of Arizona. In one of their experiments, a tank holding two fluids is attached to a sled and dropped after which it will be accelerated by a spring at the bottom of its trajectory [26], [27]. When the system is accelerated upwards off of the spring at the bottom, the instability is allowed to evolve in the absence of gravity. These experiments were done at low-Atwood numbers with miscible two-liquid systems. The interface between the two fluids initially has a sinusoidal shape (single-mode), which will invert and grow in amplitude after the impulsive acceleration is applied. Good agreement was found between linear stability theory predictions and the actual measured amplitude growth rate. Similar mechanical methods to generate the acceleration have also been used, including rockets [28], [29] and linear electric motors [30].

The last and most common method for providing the required acceleration is to launch a shock wave from the high-pressure side of a shock tube into the low pressure side. The rest of the experiments discussed in this thesis utilize this type of acceleration. Some of the first experiments performed using this method used a membrane to create an interface between the two or more gases being studied. Meshkov [15] was the first to use a membrane to shape the fluid interface in his experiments which reinforced the theory put forth by Richtmyer [14]. This method of separating the fluids and shaping the interface has several problems including that it can influence the physics of the flow

development when the membrane breaks and fragments are sent downstream. The membrane fragments are also problematic as they can be obstructions for the laser-based diagnostics, namely Particle Image Velocimetry (PIV) and Planar Laser-Induced Fluorescence (PLIF), as well as other optical diagnostics [31], [32], [33], [34]. It was found that the effect of the membrane is the greatest at the initial stages of the RMI when the amplitude of the perturbations is small; however, the effect was less noticeable after reshock when the amplitudes had a longer time to grow. Also, when the fragments block the laser sheet, there are holes in the data collected. One of the strengths of using a membrane to form the gaseous interface is that a wide variety of shapes can be achieved. One such shape is the chevron interface which is in a "v" shape [35]. The research group at the Atomic Weapons Establishment (AWE) studied an inverse chevron interface with and Air-SF_6-Air configuration with a Mach number of 1.26 and Atwood number of 0.67 [35]. The gases were held in place using a microfilm membrane supported on a fine wire mesh. Both horizontal and vertical wires were used which were 25 um in diameter with 4 mm spacing giving a total flow blockage of 1.25%. One benefit of this experiment compared to the inclined interface experiments which will be discussed later is that additional wavelengths can be studied with the wall boundary layers having a smaller effect. They found good agreement between the large-scale features in the Mie scattering images obtained experimentally and the images generated from the TURMOIL 3D code.

A technique was developed by the group at the University of Wisconsin at Madison (UWM) to shape the interface using a soap bubble so that a traditional membrane could be avoided [36], [37], [38], [39], [40], [41]. A fluid is blown into the bubble and placed in shock tube filled with a gas of different density. The density of the

gas in the bubble can be greater or less than the density of the surrounding gas. The arm that supports the bubble retracts before the shock wave impacts the bubble. This problem was studied in a vertical shock tube of square cross section capable of producing planar shock waves $2 < M < 3.8$. It was found that the early phase of interaction of the planar shock wave with the bubble of gas is dominated by the formation of a primary vortex ring due to baroclinic vorticity deposition. At later time, secondary and tertiary vortex rings were observed.

Another experimental technique developed without the need for a membrane is the varicose gas curtain used at Los Alamos National Laboratory [42], [43],[44], [45], [46], [47], [48], [49]. The gas curtain or columns of gas are injected from the ceiling of a horizontal shock tube and sucked from the floor. Experiments have been performed for a gas curtain of SF_6 with the surrounding gas being air at Mach numbers 1.1 and 1.2. Good agreement was found between experimental integral mix widths and a mixing width model. Simultaneous PLIF/PIV diagnostics have also been implemented at this experimental facility. This is important as compressible turbulent mixing is an example of what Dimotakis referred to as Level II mixing where the velocity and density fields are coupled due to acceleration applied to a variable-density flow field [50]. In order to understand the interaction between the two fields, they must be measured simultaneously. The group at Los Alamos has also computed parameters including the density self-correlation and turbulent mass flux for the BHR (Besnard, Harlow, and Rauenzahn) model, which was developed to model variable-density turbulence problems [51].

The group at the University of Arizona developed a technique where gases are flowed into a vertical shock tube (the light gas from above and the heavy gas from below)

so that the light gas rests on top of the heavy gas [52],[53], [54], [55]. The gases are allowed to exit the shock tube through exit ports in the walls. Additional perturbations can be added to this type of interface by shaking the whole shock tube. However, the shock strengths, which can be used for experiments in this shock tube is limited to just M ~1.2. Another variation which was used in this setup was the use of an innovative speaker assembly to create small-wavelength, large amplitude Faraday waves on the interface. The multimodal interface was created with air over SF_6, and was shocked with a $M \sim 1.2$ shock wave. Integral penetration growth prior to reshock exhibited power-law behavior. The results from these experiments were limited to just interface width measurements.

The group at UWM also created a single-mode interface without the need for a membrane. One of their techniques was to use a set of pistons (installed in the sides of a vertical shock tube) to "push" the interface from either side [56]. This resulted in a repeatable interface that could be shocked and studied using the Mie scattering technique. The experiments covered a parameter space of $0.29 < A < 0.95$, $1.1 < M < 3$, and $3.1 \times 10^4 < Re < 1.4 \times 10^7$. A growth reduction factor was needed to obtain good agreement between simulations and experiments for amplitude growth rate. This was due to the effect of a diffuse interface for which the simulations did not accurately account. These were the first experiments which documented bubble-growth suppression due to shock proximity.

Another technique this group used was to place a sinusoidal metal plate between the gases which would retract before the arrival of the shock wave [57]. If a heavy gas is placed above a lighter gas, the two will mix upon the removal of the plate due to the Rayleigh-Taylor instability. Experiments were performed with carbon dioxide over air

with a Mach 3 shock wave. The initial amplitude-to-wavelength ratio used was large enough that the interface evolution very quickly entered the nonlinear growth regime as measured with planar Mie scattering images. One of the drawbacks of this technique is that when the plate retracts, shear is imparted on the interface. Depending on the rate at which the plate is retracted, this could be non-negligible.

There has been more interest recently within the RMI community on more complex multimodal interfaces which are more challenging to model and better represent conditions faced in real-world applications. The UWM group created an interface with additional modal components by co-flowing a heavy gas over a light gas at the interface [58], [59]. The experimental results published in 2012 used argon over helium (A~0.7) and a Mach 1.6 shock wave. Just 2.1 ms after shock acceleration, the interface was shown to be fully turbulent based on PLIF measurements. Furthermore, the mixing structures were shown to be isotropic at late time. Scalar variance energy spectra showed a $k^{-5/3}$ inertial range at late time, where k is wavenumber. There is still debate in the RMI community regarding if $k^{-5/3}$ or $k^{-3/2}$ should be seen as turbulence induced by the RMI is an example of decaying turbulence, which does not have to abide by the guidelines of classical turbulence.

The group at LANL also created a multimodal interface. Although they also co-flowed gases near the interface, they added a flapper plate to create a multimodal and multidirectional interface [60]. The flapping oscillations were composed of three different amplitudes and frequencies superimposed upon each other. This resulted in an initial condition with a wide variety of velocity scales. A Proper Orthogonal Decomposition (POD) was used to analyze the energy contained in each mode. A

collection of 300 velocity fields were used in the analysis. It was found that only the first 36 modes were required to capture 80% of the total kinetic energy contained in the flow for the initial condition.

All of the shock tube facilities discussed thus far have either been horizontal or vertical. However, an inclined shock tube offers several key advantages. It can operate in either the horizontal or vertical configurations, but it can also be used to control the cross product between the gradients of pressure and velocity (see the baroclinic term in the vorticity equation). The first inclined shock tube reported in the literature was developed at Polytech Marseille in France [61]. The facility was reported to have a Mach number range between 1.05 and 4 with the ability to reach any inclination angle. Shadowgraphy and high-speed cameras were used to obtain data at a rate of 20 kHz. Although the authors discussed the possibility of studying the RMI by launching an oblique shock through a diffuse interface, sadly no publications on this work ever resulted. The group did, however, study shock-bubble interactions using the shadowgraphy diagnostic [62]. They studied negative, zero, and positive density jumps across the shocked bubble for weak Mach numbers. Linear growth was seen after the initial bubble compression stage.

The group at the University of New Mexico also developed an inclined shock tube to study a gas column accelerated by an oblique shock wave [63], [64]. The facility can produce shock waves between Mach 1.13 and 2.0 when the driver is charged with helium. When the driver is close to the rupture pressure, a spear mechanism bursts the diagram. Lasers at 266 nm are used to excite acetone molecules placed in the heavy gas within the cylinder. They used the PLIF diagnostic to study 3D vorticity deposition on

the heavy gas column. The streamwise extent of large-scale counter-rotating vortices was found to be unchanged for the oblique shock case compared with the planar shock case.

Finally, the current work utilizes an inclined shock tube with a larger cross-section (11.43 cm x 11.43 cm) and Mach number (3.0) capability than the previous facility. It has been used to study the evolution of an inclined interface after incident shock interface using Mie scattering and PIV diagnostics [65] and after reshock [66]. High resolution Mie scattering images prior to reshock revealed secondary vortex structures which contributed to secondly vorticity deposition (characterized with PIV measurements). After reshock, the streamwise component of the turbulent stress was shown to be dominant. The reshock wave caused an amplification of energy as shown by the Turbulent Kinetic Energy (TKE) spectrum. The TKE spectrum began to develop an inertial range for the most developed case even before reshock occurred.

1.3.2 Simulations and Theoretical Works

This section is devoted to the simulations and theoretical works which the previous experiments can validate. The works reviewed will be limited to those related to modeling the RMI.

The first theoretical basis for the RMI was put forward by Richtmyer [14]. Richtmyer built off the work of Taylor but assumed that the acceleration was impulsive (modeled as the Dirac delta function) and that compressible effects could be neglected. He found that the growth rate was proportional to the velocity jump induced by the source of impulsive acceleration (Equations 4). His earlier theory focused mainly on a

sinusoidal interface between the binary fluid system. It was not until ten years later that Meshkov followed with experiments [15].

Equations 4

$$\frac{d^2\eta(t)}{dt^2} = kgA\eta(t)$$

$$A = \frac{\rho_h - \rho_l}{\rho_h + \rho_l}$$

$$\dot{\eta} = k[v]A\eta_0'$$

$$\eta_0' = \eta_0\left(1 - \frac{|[v]|}{w_i}\right)$$

This impulsive growth model depends strongly on the linearity of the perturbation. This accounts for some of the disagreements Meshkov found in his experiments, some of which had non-linear perturbations. Typically, if the amplitude-to-wavelength ratio is less than 0.1, then the perturbation is considered linear. The growth of a perturbation can be described in terms of the bubble growth (the light fluid penetrating into the heavy one) and spike growth (the heavy fluid penetrating into the light fluid). In cases where the Atwood number is greater than zero, the spike growth rate will dominate. Next, a discussion of simulation attempts will be given.

There have been many efforts to use simulations to study the RMI. Ares has been used to study the inclined interface perturbation [67], [68], [69], [70]. Ares is a staggered mesh arbitrary Lagrange Eulerian (ALE) hydrodynamics code developed at Lawrence Livermore National Laboratory. The Lagrange time advancement is second-order predictor and uses the Gauss Divergence theorem to give the discrete finite difference equations [67]. The numerical differences are all fully second order in space. All of the simulations used a fixed Eulerian mesh. Ares employs adaptive mesh refinement (AMR) with the resolution increasing by a factor of three for each level of refinement. A

parametric study was conducted where the Mach number ($1.2 < M < 2.5$), shock tube inclinational angle ($30^o < \theta < 60^o$), and gas pair were all varied (Air-SF_6 and He-SF_6). An adaption of the Richtmyer impulsive model scaling was presented which allowed for the collapse of nondimensional mixing widths for both linear and nonlinear perturbations.

Olson and Greenough at LLNL investigated shock-induced mixing in a binary gas system using both Large Eddy Simulations (LES) and Direct Numerical Simulations (DNS) [71]. They sought to examine the effects of physical dissipation of the velocity field and species mass fraction as well as numerical dissipation arising from numerical errors in the method used. Parameters studied include grid resolution, Reynolds number, and numerical method. DNS was used with two different codes using both high- and low-order numerical methods, and convergence was found for both temporal and spectral quantities. The framework the authors created can be used in future studies to estimate the effective Reynolds number as well as quantify the impact of numerical dissipation on RMI mixing problems. Finally, the resolution required for such simulations is also provided.

The group at the University of Arizona collaborated with Cabot and Greenough at LLNL to simulate the sinusoidal interface experiments performed in a vertical shock tube [55]. The interface is generated by gases flowing out of two exit slots in the shock tube and oscillating the tube to create a standing wave on the interface. A strong density gradient was created by placing air over SF_6. A small acceleration was provided by a Mach 1.2 shock wave. Simulations with Ares and Miranda codes from LLNL suggest that some of the acceleration observed in the experiments is due to the growth of the boundary layers. This is one of the reasons our shock tube has a large internal cross

section. This effect is minimized in our shock tube experiments. When this effect is taken into account, better agreement was found between experiments and the Richtmyer-Meshkov buoyancy-drag model. Circulation measurements made with PIV also compared well with what the two codes predicted. It should be noted that a compressible version of the Miranda code was used that solves the Navier–Stokes equations for compressible ideal gases. Grid-dependent artificial viscosity and diffusivity needed to be used to accurately capture small scales.

Shilling and Latini used higher-order (9^{th} order) 3D Weighted Essentially Nonoscillatory (WENO) simulations to study a reshocked Richtmyer-Meshkov instability at late times and compared results to experimental data [72]. These higher-order simulations are better suited for shock-driven flows which contain a large range of scales and complex structures. The computational domain was selected to be 513×257^2. The simulations were set up to model the Vetter and Sturtevant experiments [31]. The Mach number was 1.5 and the gas pair was air and SF_6. Random noise was used in the initial condition to break symmetry. TKE was plotted at three different times including before and after reshock. Reshock provided an amplification of TKE and further development of an inertial range.

Hahn, Dirkakis, Youngs, and Williams [73] conducted a numerical study to investigate the turbulent mixing which resulted from a shock wave interacting with an inverse chevron interface. The Mach number was 1.26, and the gases were SF_6 and air. The realistic interface perturbation from the experiments was modeled using a summation of individual wave modes involving sines and cosines. The amplitudes where chosen so that they followed a Gaussian distribution. The numerical approach used was implicit

large eddy simulation (ILES). This approach assumes that certain features in the nonlinear numerical method locally produce similar effects to when explicit subgrid models are used in traditional LES [73]. The authors cite that the leading order of kinetic energy dissipation rate is proportional to $u^3/\Delta x$ for a modified scheme. This dissipation rate is used as the subgrid model for the ILES simulations [73]. The key finding of this study was that although short wavelength surface irregularities lead to more mixing at early times, they cannot support turbulent mixing at late times.

Hill, Pantano, and Pullin [74] used LES to study a multiscale RMI after reshock. They also designed their simulations to model the experiments of Vetter and Sturtevant [31]. The sidewalls of the shock tube were replaced with periodic boundary conditions which allowed for calculating planar spectra. The interface was modeled using the 'egg-carton' perturbation described by a summation of sinewaves. The numerical method used tuned centre-difference (TCD) stencils to integrate the equations of motion along with a Runge-Kutta time-stepping scheme [74]. All three experiments simulated showed good agreement for growth rates of the mixing region both before and after reshock. The mixing widths at the end of the simulations deviated at most between 4% and 10% from experimental values. This discrepancy can be attributed to the modeling of the initial conditions.

To summarize, the experimental, computational, and theoretical research effort studying the RMI has been mainly directed towards determining the interface growth rate. There are only a couple of experiments which has looked at the turbulent mixing environment by conducting simultaneous density/velocity measurements. The current study is aimed at understanding the impact of the initial conditions on the evolving

turbulent mixing environment. The present study is an effort to bridge the gap currently between the laser-driven experiments which have studied the impact of initial conditions (with limited data) and work done in the area of Rayleigh-Taylor-driven flows. The experimental data can be used for code validation and development and tuning of new theoretical models studying variable-density flows.

CHAPTER 2: Experimental Facility

2.1 Inclined Shock Tube Facility

The experiments for the studies in the current work will be carried out in the inclined shock tube facility at Georgia Institute of Technology. This facility is a variable-inclination (0-90^o), downward firing shock tube, 9 m long with an 11.43 cm x 11.43 cm internal cross-section (Figure 11, Figure 12). The walls of the shock tube are two inches thick and made of 4140 steel heat treated to a hardness of RC32 (yield strength > 100 ksi) in order to withstand the dynamic pressure after reshock (6 MPa). The threads on the bolts is the expected failure point. The shock tube was designed to allow for strong shocks ($M > 3$) when helium is fired into atmospheric air. The diaphragm between the driver and driven section is ruptured by an x-blade. A quick-release clamping mechanism and hydraulics system allow for a large number of experiments to be run (20-30 shots/day). A large number of experiments are important especially for convergence of turbulence statistics. The test-section of the shock tube features overlapping windows for interfaces longer than 15.24 cm. Alternatively, a 49.5 cm long acrylic window can be used to image especially long interfaces which occur at high Atwood numbers and after reshock. Simultaneous velocity and density fields are measured using the particle image velocimetry and planar-laser induced fluorescence, respectively. The beams of two Nd: YAG lasers, 135 mJ/pulse at 266 nm and 250 mJ/pulse at 532 nm, are combined and diverged within the shock tube to create a sheet which illuminates the center plane of the shock-tube for these measurements. Nd: YAG is the type of crystal the laser uses. It stands for neodymium-doped yttrium aluminum garnet.

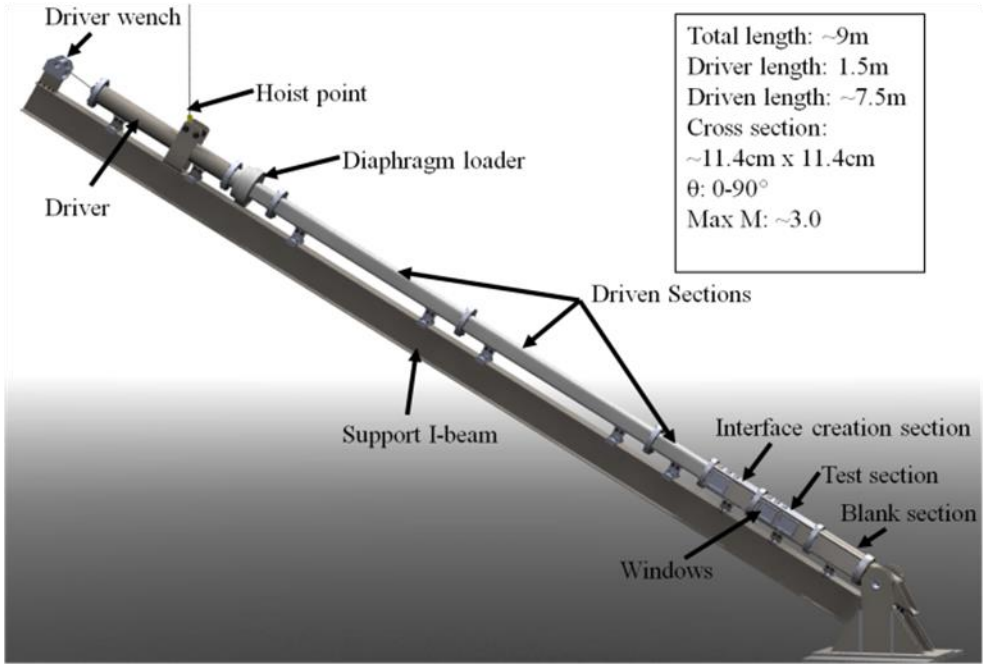

Figure 11: SolidWorks render of inclined shock tube with specifications annotated [67].

A unique feature of the inclined shock tube facility is the hydraulic diaphragm loader assembly (Figure 13). The assembly consists of a collar, hydraulic clamp, and hydraulic return rams. The collar slips over the flanges of the driver and driven sections and locks into place. The collar weighs on the order of 30 lbs. and can be lifted into place by one person. Once the collar is in place, the hydraulic clamp is pressurized by a hydraulic pump to approximately 2,500 psi. The hydraulic clamp presses an internal face on the driver-side flange onto the diaphragm placed between the driver and driven flanges. O-rings are used to ensure a seal is made between the flange and the diaphragm material, which can be metal or plastic. When the user wishes to remove the diaphragm, the hydraulic clamp is de-pressurized, and the hydraulic return rams are pressurized. The hydraulic return rams push the hydraulic fluid out of the internal cavity in the hydraulic clamp and into a holding container. After a sufficient number of experimental runs (20-30), the holding container will become full, and the fluid must be transferred back into

the hydraulic pump reservoir. An improvement on this system would be to implement a closed system where the hydraulic fluid would automatically transfer back into the hydraulic pump reservoir. It should be noted that this hydraulic diaphragm loader was designed by the Sturtevant group at Caltech in the 1980s.

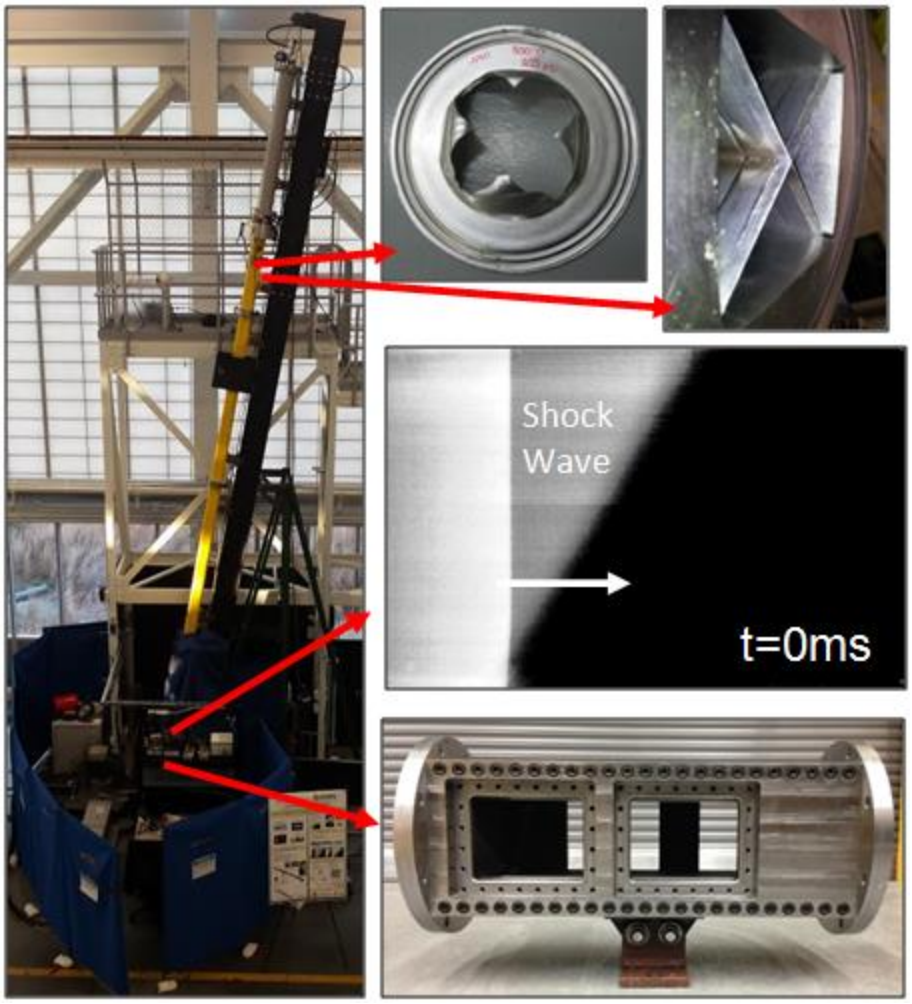

Figure 12: Georgia Tech shock tube facility. Left: Shock tube inclined at 80°, Top right: Ruptured diaphragm and X-blade, Middle right: PLIF image of inclined interface with shock wave, Bottom right: Single test section with overlapping windows.

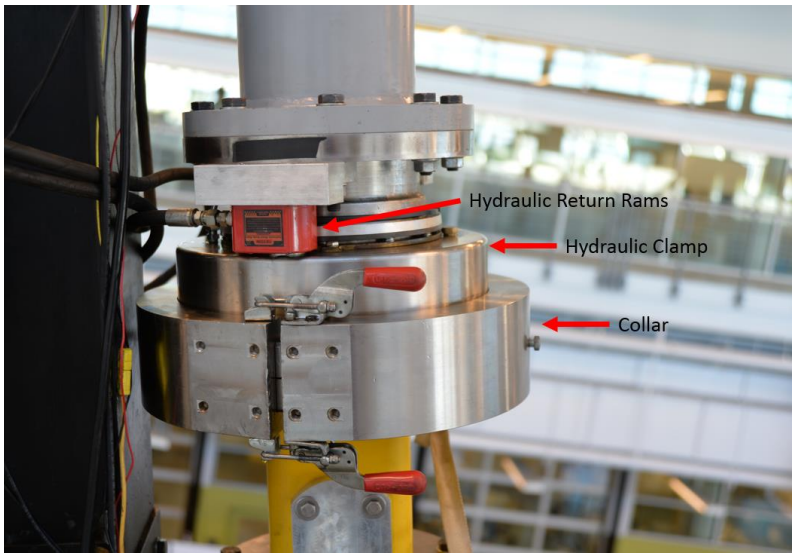

Figure 13: Hydraulic diaphragm loader assembly.

The top of the driver has three valves, each for a specific purpose with unique capabilities (Figure 14). The driver fill valve is a solenoid valve capable of controlling pressures at least up to 2,000 psi. A manual ball valve upstream of this valve is used to throttle the flow into the driver during filling to ensure that the diaphragm does not rupture prematurely. As a rule of thumb, the driver should fill at a rate of about 5-10 psi/second to avoid causing premature damage to the diaphragm. All of the hoses shown in Figure 14 are hydraulic hoses rated for several thousand psi. A steel pipe is used to route the gas to the driver as it provides a higher flow rate than most hoses available on the market. The boost valve is a high-flowrate solenoid valve rated to 7,500 psi which allows for a sudden mass influx into the driver so that the diaphragm can be ruptured in a repeatable way. Generally, the driver will be filled to about 70% of the break pressure, and the boost valve will push the diaphragm past the breaking point. The boost valve is open for about 500 ms for Mach 1.55 experiments. The relief valve is an electrically-actuated ball valve which allows the shock tube to be vented after an experiment. It is

also a safety mechanism. If the driver is filled for an experiment, but for some reason the operator does not wish to perform the experiment, the driver can be safely vented using the relief valve.

The winch in Figure 14 is used to pull the driver up and out of its resting place on the driven section so that the diaphragm can be accessed. The winch has a wired controller which the user can reach when standing on the platform next to the shock tube. If the winch were to lose power, it fails in the current position. A bolted design for the winch was used so that it can be exchanged for a different one in the event that the driver design changed. Furthermore, the entire design of the shock tube is modular for the same reason.

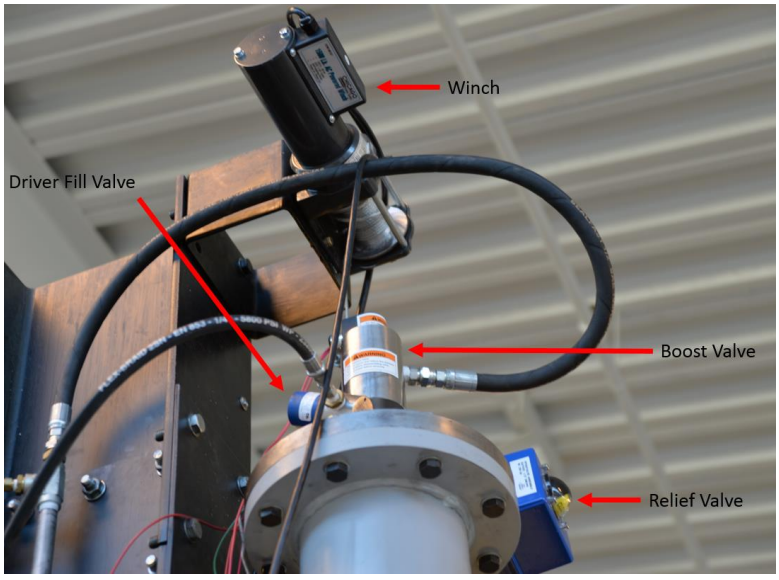

Figure 14: Winch and valves attached to the top of the driver.

Before the gases enter the test section, they go through mixing chambers (Figure 15). The light gas is divided into two streams. One stream goes through an acetone bubbler and into a mixing chamber. The second stream goes through a fog machine, and

then into the same mixing chamber. The two mixtures are mixed within the chamber using an electric fan. The heavy gas also goes through the fog machine before entering its mixing chamber. The only difference is that the heavy gas is not seeded with acetone.

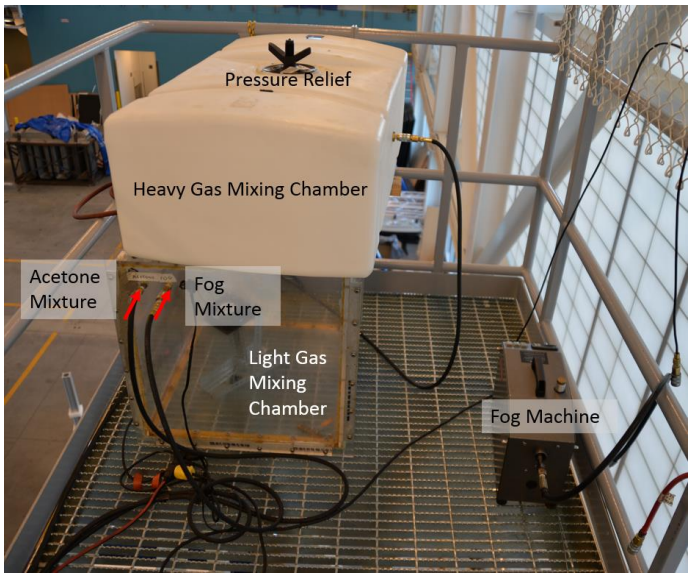

Figure 15: Mixing chambers that gases go through before entering the test section and fog machine.

A custom acetone bubbler is used to seed the light gas with acetone for PLIF imaging (Figure 16). The light gas enters through the top of the bubbler and is routed through a copper tube with small holes in it near the bottom of the bubbler. The gas then bubbles up through the acetone. It creates an acetone/gas mixture in the volume of the bubbler above the acetone. This mixture is carried away from the bubble and into the mixing chamber. Since the saturation of acetone in a gas varies with temperature, the temperature of the acetone in the bubbler is held constant by using an electric heater which receives feedback from a thermocouple placed in the acetone bath. The feedback control loop is achieved using LabVIEW software.

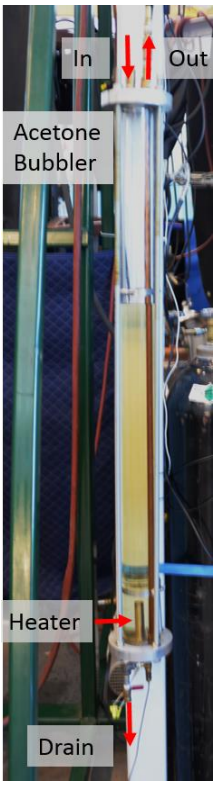

Figure 16: Acetone bubbler equipped with heater for seeding light gas with acetone.

Once the gases are seeded and inside the shock tube, they need to be illuminated with a monochromatic light source, in this case a laser, so that they can be imaged. The equipment layout for the lasers is shown in Figure 17. The 532 nm and 266 nm lasers are placed perpendicular to each other for the beam combination. A beam splitter is used to allow the 532 nm to pass through unimpeded while the 266 nm reflects at a 90° angle. The two laser beams can then enter the shock tube while traveling parallel to one another. Dual-wavelength mirrors which are 45° relative to the incoming beams are used to redirect the laser beams into the plane of the inclined shock tube. It is important that the mirrors are 45° relative to the beam so that > 90% of the laser energy can be retained. This constraint means that two mirrors needed to be used (Figure 18). Other angles of reflection are much less effective. The timing of the laser pulses is controlled by

synchronizers, one synchronizer per laser. The synchronizers communicate with both the TSI and LabVIEW software. They can easily accommodate microsecond accuracy.

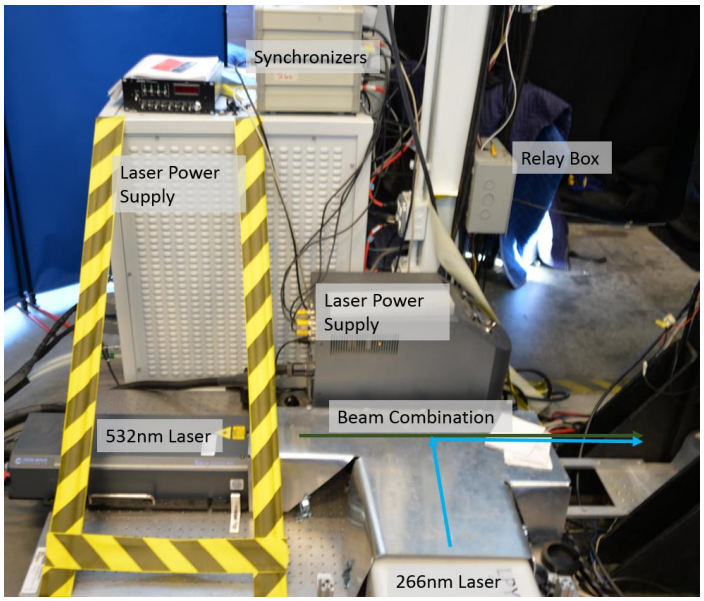

Figure 17: Lasers-related equipment used for non-intrusive, laser-based diagnostics.

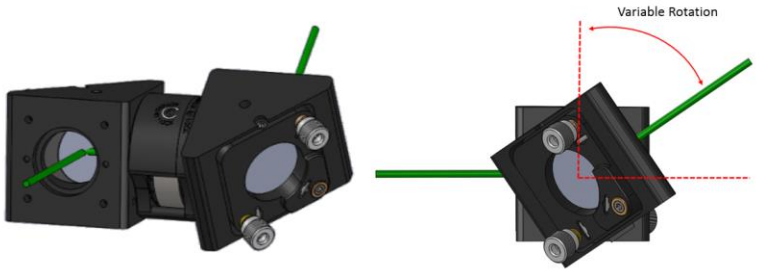

Figure 18: Lens assembly for dual-wavelength mirrors which allows the laser beams to come into the plane of the inclined shock tube.

The lasers illuminate the center plane of the shock tube which is then imaged using CCD (charge coupled device) cameras (Figure 19). The sensor size is 36.3 mm x 24.2 mm with a pixel resolution of 6600 x 4400 pixels. The cameras are operated in single-tap mode which yields a dynamic range of 14-bit (intensity range of 16,383). This operating mode is best for these PLIF measurements because the sensor will give a more uniform result which will not be saturated easily. The downside to single-tap mode is that

the frame rate is slower, but because this is a single-shot experiment, the frame rate is not a concern. Each camera uses a 50 mm f/1.2 Nikon lens. The large aperture allows for a large portion of the PLIF signal to be captured. The full aperture capability is neither needed nor used for PIV measurements. The minimum frame straddling time for PIV is 990 ns. Since two different wavelengths of light will be emitted from the gases, light filters must be used on the cameras to differentiate the signals. A bandpass filter is used on the PIV camera which passes 532 nm. A notch filter is used on the PLIF camera which does not pass 532 nm. Since the two cameras are both attempting to capture the same field of view, one of the cameras must be angled. The PLIF camera was chosen to be angled since the signal was found to remain strong even when angled. Therefore, a scheimpflüg mount was used on the PLIF camera so that it can keep the center plane in focus. The scheimpflüg condition was calculated so that the precise angle between the lens and the sensor could be known. The calculation acts as a guide, but the angle that actually brings the full plane into focus is found through multiple iterations of setting the angle and attempting to focus on the calibration target.

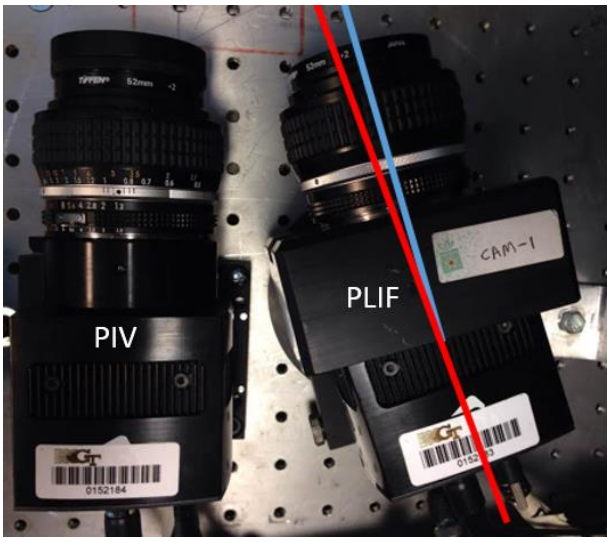

Figure 19: 29 MP CCD cameras used for simultaneous PIV/PLIF measurements. PLIF camera utilizes a scheimpflüg mount. Centerline of CCD (red) and of lens (blue) labeled.

The cameras and lasers are all triggered off of dynamic pressure transducers (DPTs) which are mounted before the test section. Specifically, the equipment is triggered off of the first DPT in the upstream set (Figure 20). The set of transducers are mounted 10 cm apart so that the speed of the shock wave and hence the Mach number can be calculated since the speed of sound in the medium can also be calculated. A DPT is also mounted at the very bottom of the shock tube to measure the strength of the shock wave as it impacts the bottom wall. The downstream pressure transducers are mounted on a removable window flange. They mount flush to the inside of the shock tube so that they will not disturb the physics of the problem being studied. The signals from the DPTs are received by PCB Piezoelectric signal conditioners and then routed to National Instruments hardware using BNC cables.

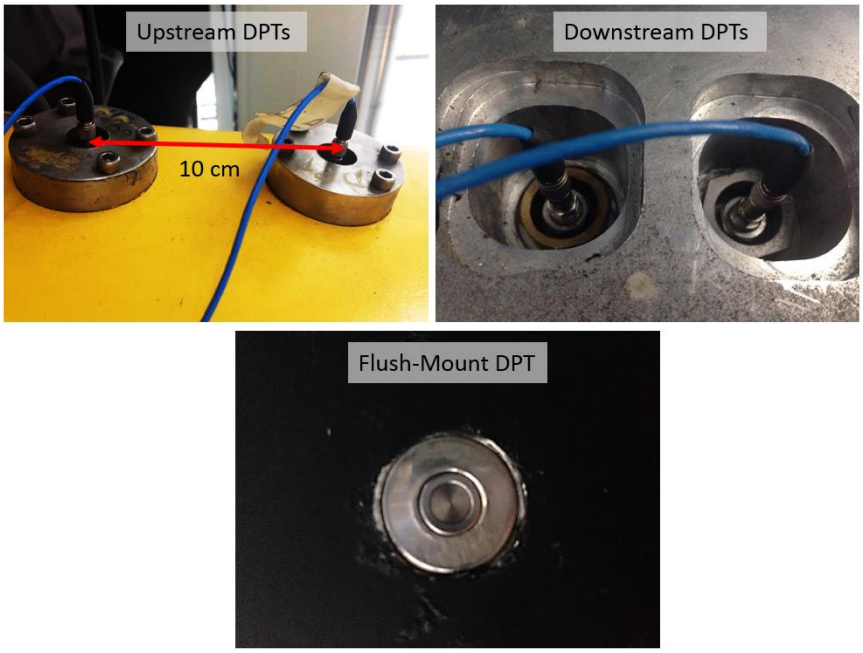

Figure 20: Upstream and downstream sets of dynamic pressure transducers (DPTs). The DPTs are mount flush on the inside of the shock tube.

All of the hardware used to read the signals are shown in Figure 21. A custom power supply and signal exchange interface were built to control the mass flow controllers. Furthermore, a LabVIEW code was written which allows the user to select a desired mass flow rate. Up to three mass flow controllers can be controlled using this custom system. National Instruments (NI) BNC 2110 boards are used to read and produce both digital and analog signals. This is used for reading pressure transducers, and controlling valves, heater, etc. A separate USB device is used to read the thermocouples. The BNC boards connect to a NI power supply and then to the computer through a PCIe card. As mentioned before, the DPT signals are conditioned by the PCB signal conditioners.

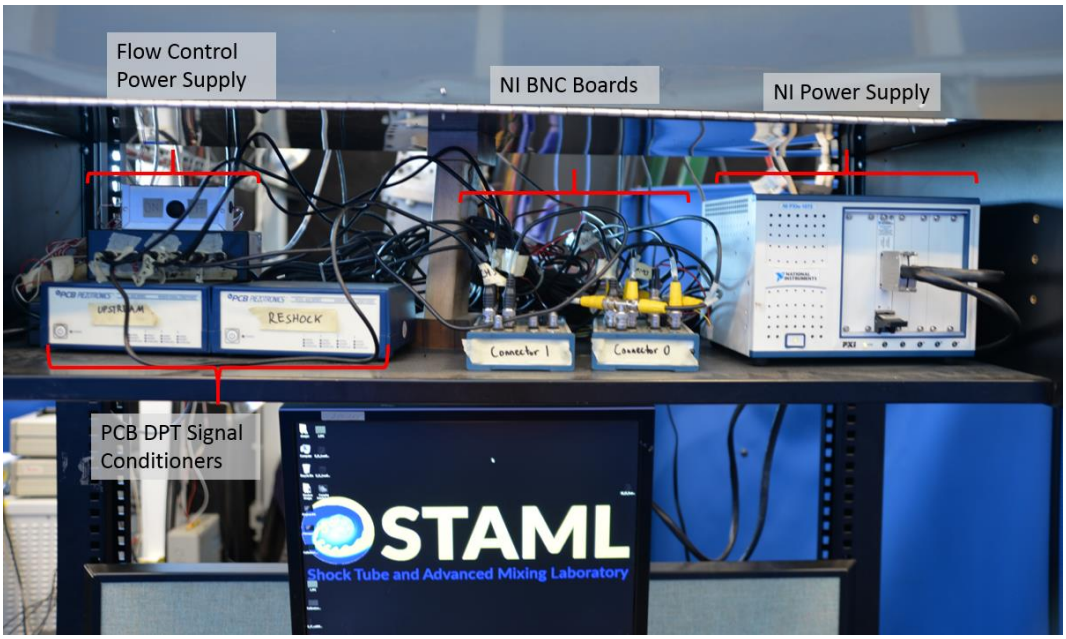

Figure 21: Hardware for conditioning and reading signals.

2.2 Simulation of Inclined Interface Perturbation

A simulation of the inclined interface perturbation was performed to further characterize the perturbation as well as provide a baseline for future simulations of more complex interface perturbations. For example, moving pistons have been considered as a perturbation technique. This would require a dynamic mesh which is able to move with the solid objects. The simulation was performed with Star-CCM+, a commercial CFD software produced by CD-adapco™. CCM stands for "computational continuum mechanics." This software is comparable to more well-known software packages such as ANSYS Fluent. The angle of inclination was set to 60° and the Atwood number to 0.23 by choosing nitrogen as the light gas and carbon dioxide as the heavy gas. Details of the problem setup will follow.

2.2.1 Problem Setup

First, the geometry of the test section was modeled in sufficient detail to allow for an accurate simulation of the initial condition (Figure 22).

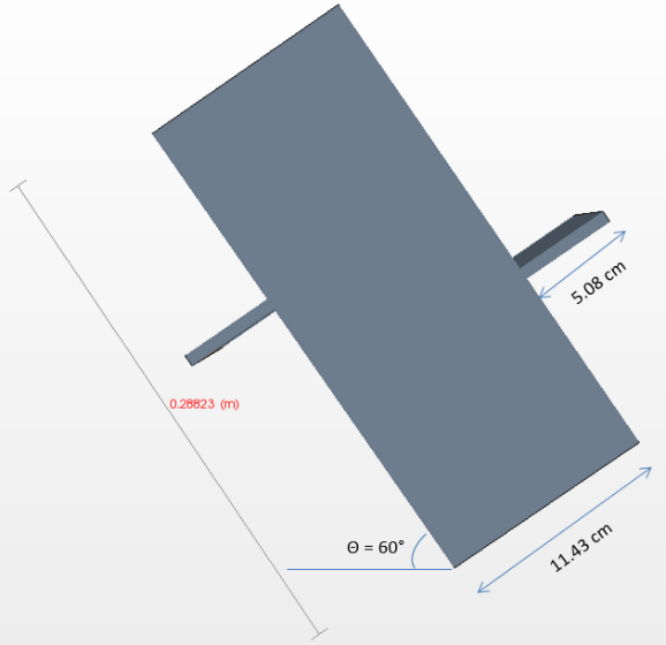

Figure 22: Test section geometry for simulation of inclined interface initial condition. Angle of inclination is 60°.

The interface exit ports in the walls of the shock tube were modeled to be perpendicular and 5.08 cm long. The full 11.43 cm x 11.43 cm cross section of the shock tube was included so that z-perturbations could be added in the future. Only 0.29 m of the test section was modeled in the streamwise direction due to limitations in processing power. In the future, it may be interesting to model a greater length of the shock tube so that the effect of gravity waves may be studied.

A polyhedral volume mesh was used with a refinement near the interface. A total of 4.5 million cells were used. Of those cells, 3.5 million were in the region surrounding the interface. A cross-sectional view of the center z plane mesh is shown in Figure 23.

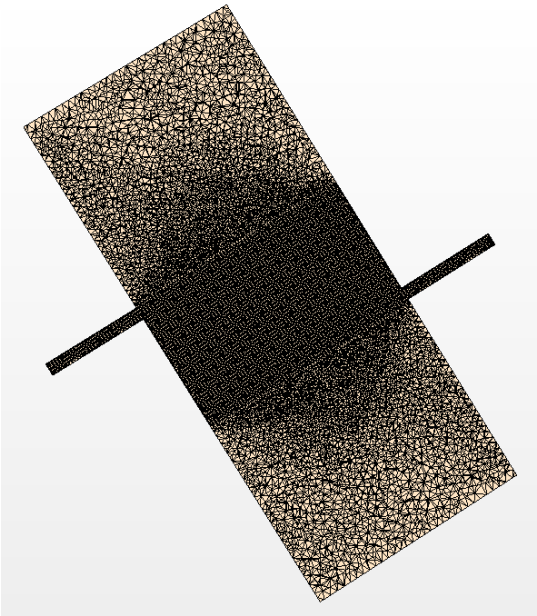

Figure 23: Cross-sectional view of polyhedral volume mesh.

Next, boundary conditions representative of the experiments were chosen. The inlets at the top and bottom of the shock tube were chosen to have specified mass flow conditions (Figure 24). This is because during the experiments the mass flow rates are controlled with mass flow controllers and custom LabVIEW software. The outlet conditions are both pressure conditions set to atmospheric pressure. All of the walls were set to be rigid and no slip.

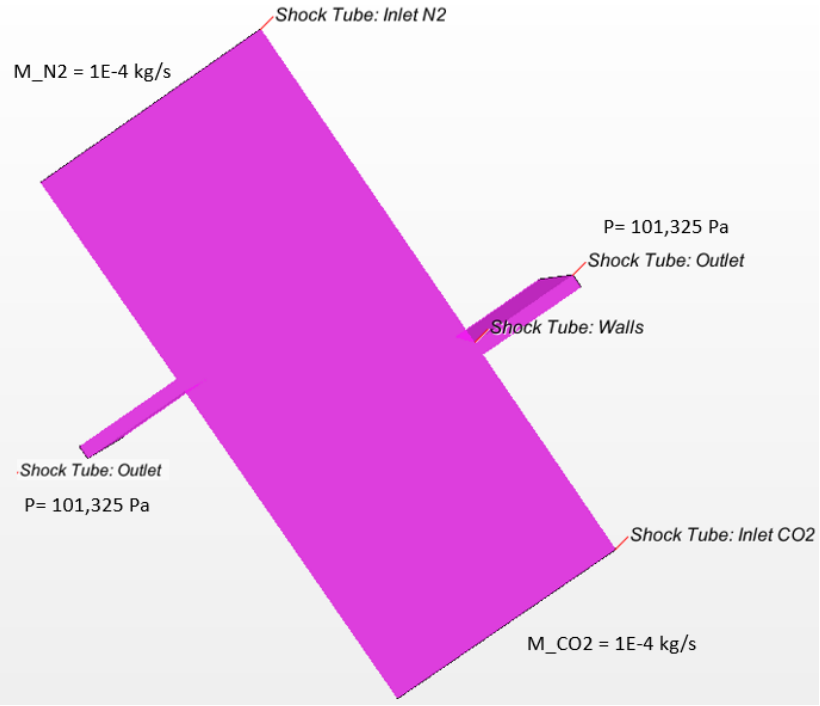

Figure 24: Mass flow inlet and pressure outlet boundary conditions with values indicated.

It was important to choose physical models which would correctly represent the physics of this problem. Because the fluids were moving at speeds much less than Mach 0.3, a constant-density, laminar model was appropriate. Gravity was enabled so that a stable, planar interface could form. A multi-component gas model was used which included nitrogen as the light gas and carbon dioxide as the heavy gas. Both gases are inert, so a non-reacting model was chosen. The flow, fluid temperature, and species were all set to segregated. Finally, the simulation is steady and three dimensional.

2.2.2 Simulation Results

The first quantity of interest is the diffusion thickness. This was estimated to be 0.9 cm from the density field (Figure 25). This compares well with the experimentally determined diffusion thickness of 0.96 cm (Figure 26).The density field is shown with a "jet' color map, where red represents the density of carbon dioxide (1.802 kg/m^3) and

blue represents the density of nitrogen (1.1453 kg/m^3). Only the center plane is represented in this density field. The frame of reference is rotated so that gravity acts in the downward direction.

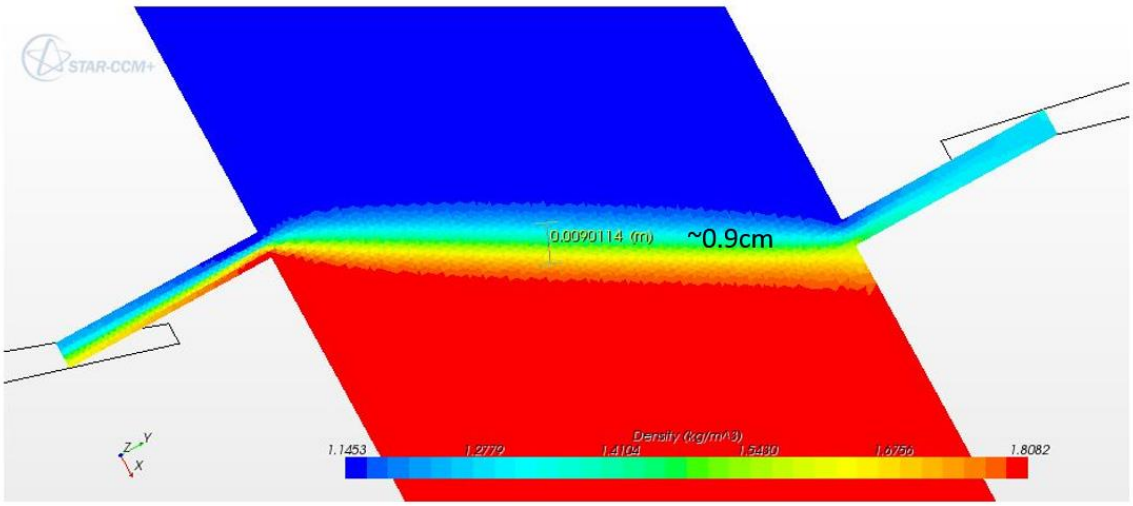

Figure 25: Density field with diffusion thickness estimated for inclined interface.

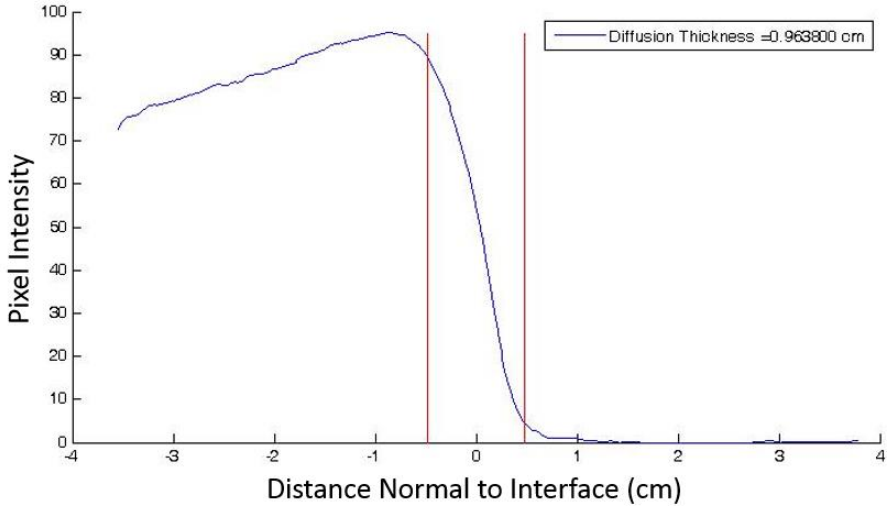

Figure 26: Pixel intensity plotted versus perpendicular distance from interface in a PLIF image. Diffusion thickness calculated from 5% -95% bounds to be 0.96 cm.

Lastly, the velocity field was considered. The velocity fields for the simulation and experiment are shown in Figure 27. The velocities seen in the simulation were on the order of cm/s – some velocities reached near 10 cm/s near the interface exit slots.

Qualitatively comparing the flow patterns seen in the simulation and experiment, it can be seen that in both the carbon dioxide favors the bottom slot. This makes sense as it is a heavier gas. The vorticity field for the center plane was also found and shown in Figure 28. As expected, the highest vorticity occurs near the interface and near the exit slots. In the center of the flow far from the interface, the vorticity is close to zero.

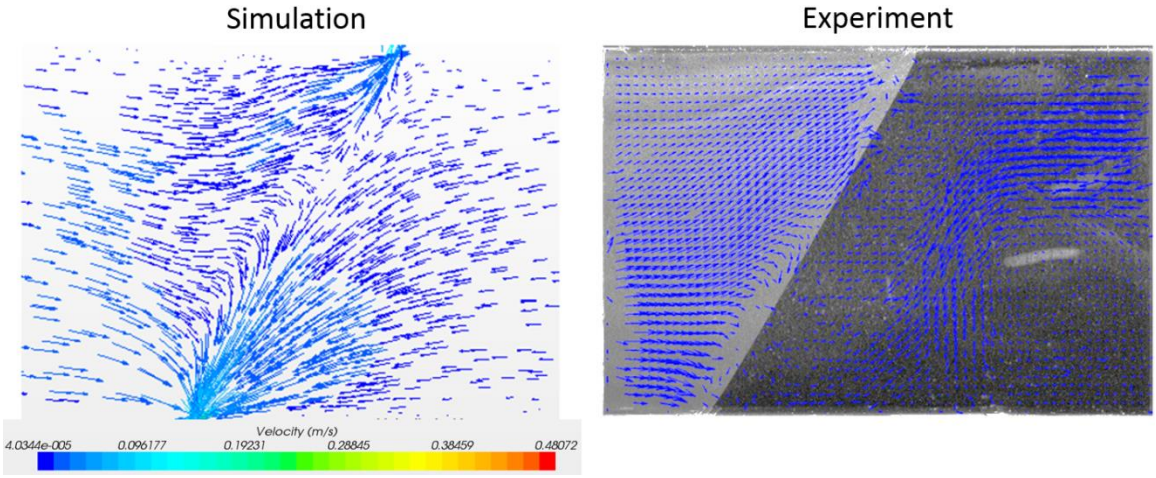

Figure 27: Velocity fields for the simulation and experiment. Both shown for the center plane.

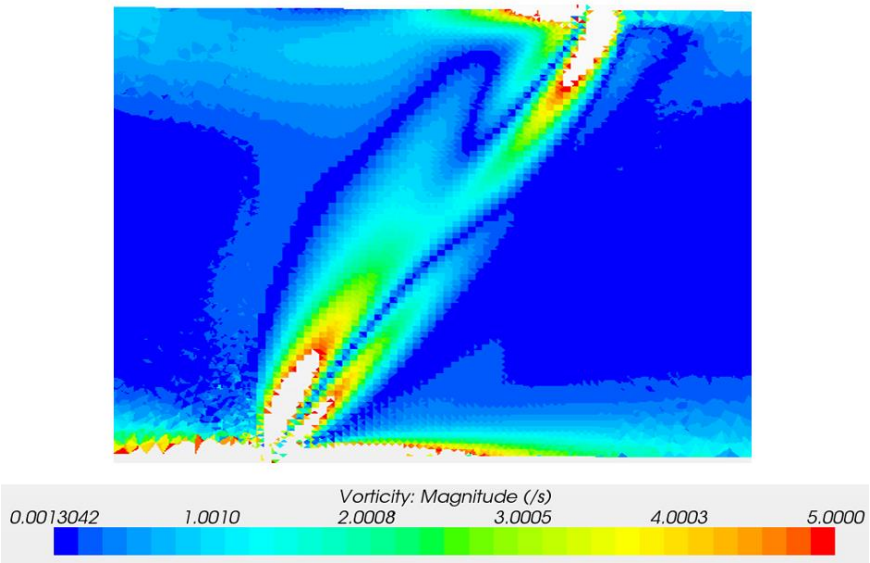

Figure 28: Vorticity field for the center plane of the inclined interface.

2.3 Test Section Design for Complex Interface

A new test section was designed in order to create a complex interface for the present experimental work. The design techniques used by the original designer of the inclined shock tube were used to ensure that the test section would be able to withstand a Mach 3 shock wave [75]. As shown in Figure 29, the test section was built to allow gases to be injected near the interface to create a counter-flow condition which will lead to shear along the interface. If a light (heavy) gas is injected into the heavy (light) gas, then non-boussinesq effects can be created as well. A key feature of this design is that the slots are parallel to the interface (this required 4-axis CNC machining). Overlapping windows were used so that the interface could be imaged as more locations. Two sets of slot configurations were included so that the complex interface could be built at 60° or 80°.

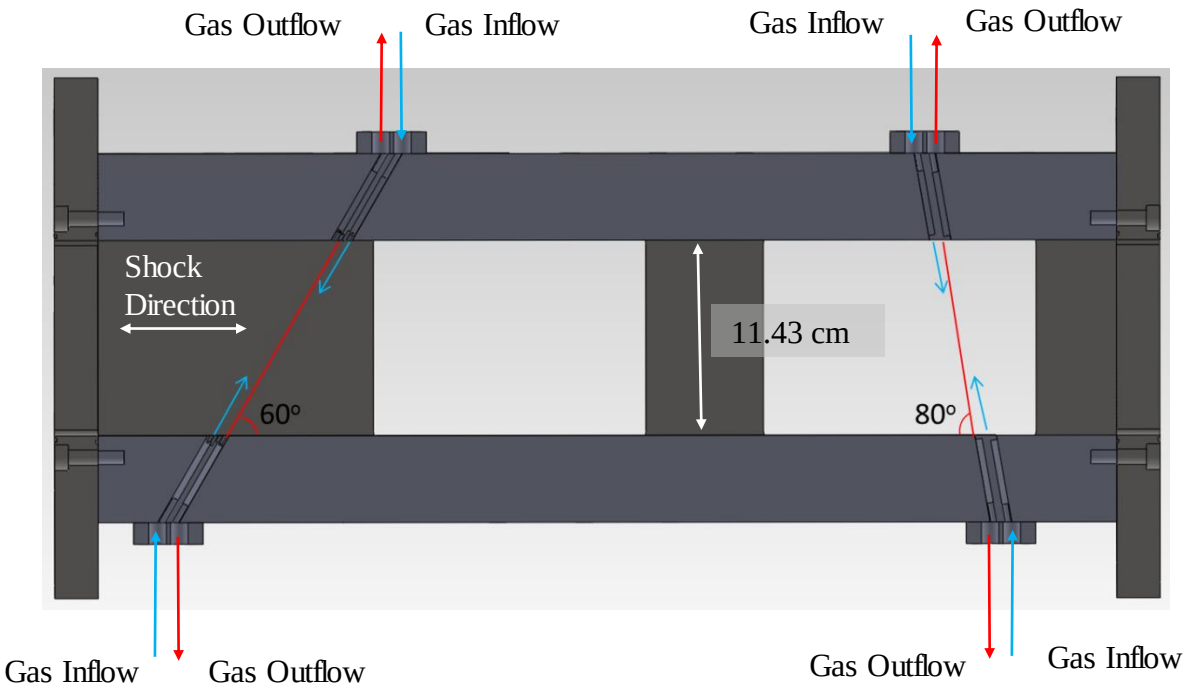

Figure 29: Design for test section (cross-sectional view) to create complex interface at 60° and 80° (as-built version shown in Figure 12).

A close-up view of the manifold used to create the counter-flow condition along with an example complex interface is shown in Figure 30. It was found that since the surface area of the manifold in contact with the high-pressure environment was small, the manifold could be made of aluminum 6061-T6. The face of the manifold which faces toward the inside of the shock tube is perforated with 1/16" diameter holes which limit the pressure loss experienced by the shock wave as it passes over the manifold. The perforations also act as flow straighteners. As seen in Figure 30, the complex interface has shear and buoyancy effects due to the flow configuration previously mentioned.

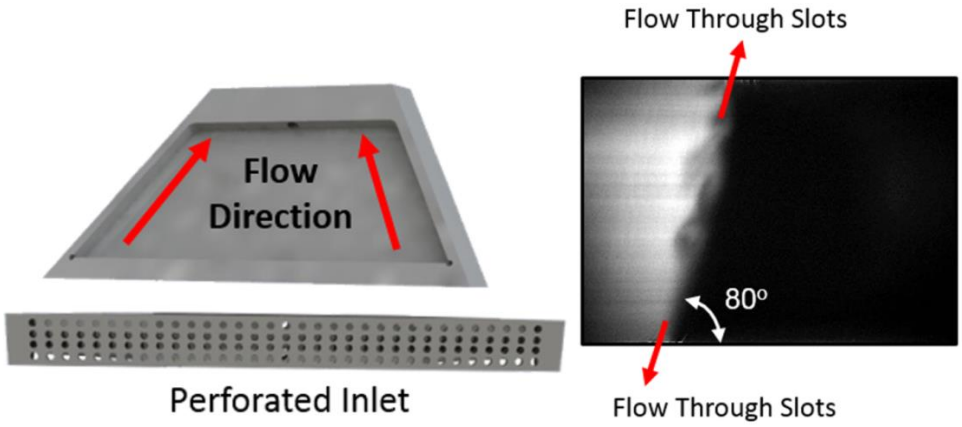

Figure 30: Left: Manifold for creating counterflow near the interface, Right: Example complex interface PLIF image for the 80° case.

The precise knowledge of initial conditions is the most important aspect of this experimental work. There are two types of initial conditions which have been investigated: (1) inclined interface and (2) complex interface. The heavy gas is introduced into the bottom of the setup, and light gas is introduced into the setup just below the end section. The gases meet at the pressure-controlled, narrow outflow exit slot built along the entire length of the interface side (Figure 31). During the experiments, the

gases are flowed continuously for ten minutes (three complete fills of the tube) in order to achieve sufficient gas purity on both sides of the interface. These ports are sealed to allow suction and to control the initial diffusion thickness. For the multi-mode experiments, we have used counter-flow shear at the interface to set up a complex interface as shown in Figure 31. A custom manifold with a perforated inlet is used to allow the gases to flow in and out of the shock tube near the interface. A collection of 100 PLIF images were used to show that the maximum standard deviation is 0.1.

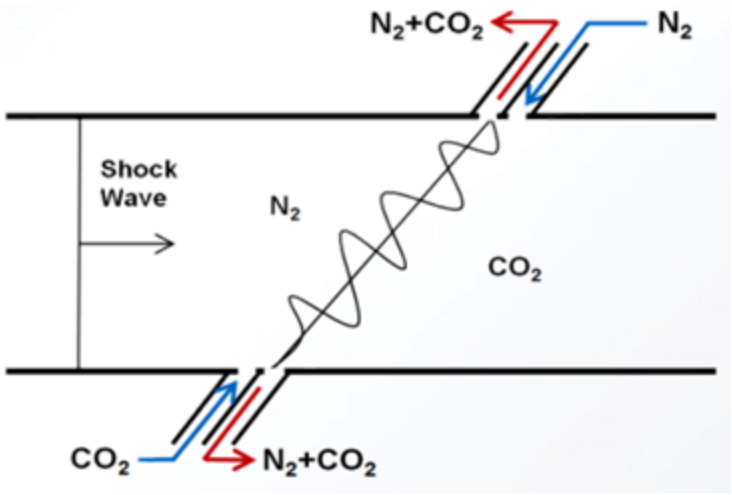

Figure 31: Schematic of the test section for creating the complex interface.

CHAPTER 3: Experimental Methods

3.1 PIV Measurements

For PIV measurements, the heavy and light gases are both seeded with glycerin fog particles using a Pea Soup fog machine. Settling tanks are used to thoroughly mix the gases with the particles before they enter the shock tube. Glycerin fog particles have a longer life than glycol fog particles and are less likely to condense on surfaces. Although our group does not have the necessary equipment to measure the particle size, the UK Atomic Energy Authority has measured the particle size distribution using laser aerosol spectrometry. The particle size was found to range in size between 0.09 μm to 0.5 μm, with a mean particle size of 0.2 μm. The ability of the particles to track the fluid flow was investigated recently. Given the estimated relaxation time of the particles in the heavy gas, the particles should fall less than 200 nm behind the flow [65]. This distance corresponds to approximately 1% of the pixel size. Since Gaussian subpixel interpolation only allows for 10% of a pixel resolution, the particle lag should have a minimal effect. The particles are illuminated with a dual-cavity New Wave Research Gemini PIV laser capable of 200 mJ per pulse at 532 nm. The laser beam passes through a plano-concave lens as it diverges into a laser sheet down the center of the shock tube. The thickness of the light sheet was estimated using a piezoelectric pulse energy meter. The optics are being optimized to achieve a 0.7 mm thick light sheet. Images are acquired with a TSI PowerView 29-MP CCD camera with no pixel binning. The time separation between PIV images is chosen such that the bulk particle movement is 20 pixels so that velocity fluctuations can be accurately captured. The PIV image pairs were processed with Insight 4G^{TM} with a starting spot size of 64 x 64 pixel and 24 x 24 pixel final spot size with 50%

overlap. This interrogation window results in a vector spacing of 372 μm. Global and local vector validation using absolute velocity and a median test are implemented between passes as well as after the final pass. The uncertainty associated with the vector fields is calculated using the primary peak ratio (PPR), which is the ratio of the primary peak in the correlation map and the second highest peak [76]. The PPR for the latest PIV data was on the order of 1% uncertainty. Uncertainty estimates of turbulence quantities will be calculated using propagated uncertainty analysis [44]. The equation for uncertainty based on the PPR is

Equation 5

$$|u|^2 = Mexp\left(-\frac{1}{2}\left(\frac{PPR-1}{s}\right)^2\right)^2 + \left(A \cdot PPR^{\beta}\right)^2 + C^2$$

where M, s, A, β, and C are fitting coefficients [76]. This equation models three independent sources of uncertainty, including the stated uncertainty as a function of the PPR and a Gaussian term for outliers. Xue, Charonko, and Vlachos provide an in-depth discussion of the development, use, and validation of this model using synthetic data sets [76], [77].

Figure 32 shows an example PLIF image and a view of the vortical structure which shows smaller rollups forming. Vectors are also overlaid on an image for reference. Figure 33 shows a sample particle field along with the associated relative uncertainty. The majority of the uncertainty in the field is below 1%. The uncertainty is calculated using Insight 4G™ from the primary peak ratio.

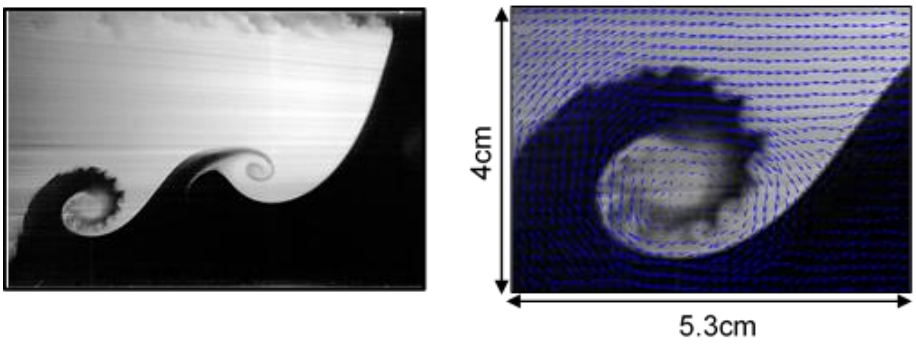

Figure 32: Left: Raw PLIF image for N_2/CO_2, M=1.55, θ=60°; Right: Vectors overlaid on vortex structure.

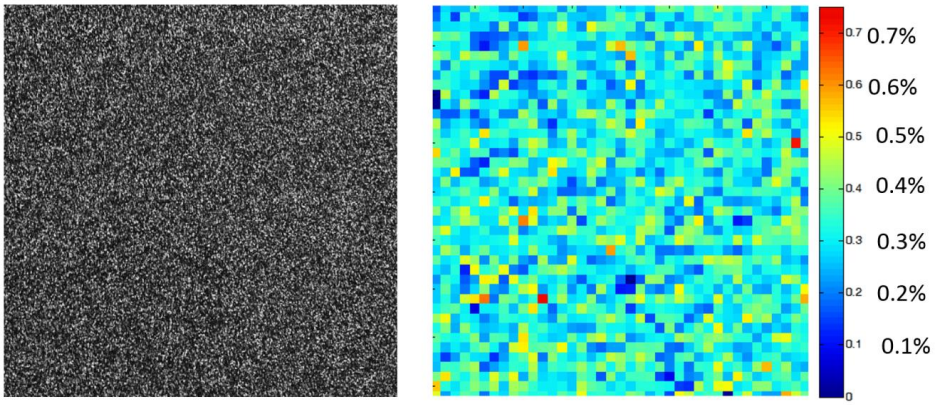

Figure 33: Left: Preprocessed sample PIV particle field for inclined interface N_2/CO_2, M=1.55, θ=80°; Right: Associated PIV relative uncertainty calculated using the primary peak ratio (PPR).

3.2 PLIF Measurements

For PLIF measurements, only the light gas is seeded with acetone. A custom acetone seeder is used to achieve a controlled concentration of acetone which allows for a linear response between fluorescence and the incident intensity. In order to minimize the temperature effects associated with acetone evaporation, the acetone bubbler is kept at constant temperature using a heater with temperature feedback. The acetone, which absorbs wavelengths between 225 nm and 320 nm, is excited using a dual-cavity Litron laser capable of 120 mJ per pulse at 266 nm. The shot-to-shot variation in the laser output

is tracked with a piezoelectric energy meter which measures the energy of a small portion of the laser beam during each experiment. Only experiments which are within a predefined tolerance of laser energy variation are used for quantitative data. The acetone fluorescence emission is captured with an unintensified TSI PowerView 29-MP CCD camera with 2 x 2 pixel binning. This binning yields a spatial resolution of 73 μm/pixel.

Seeding the light gas with acetone will result in a small change in properties. Selected relevant properties are listed in Table 1 for a gas commonly used as the light gas in experiments in the current work (nitrogen). The three scenarios listed in the table are for when pure nitrogen is used, when 12 parts pure nitrogen and 1 part nitrogen saturated with acetone is used, and lastly for nitrogen saturated with acetone. When a saturated acetone mixture is used, the decrease in Atwood number is significant (63%); however, when a 1:12 ratio is used, the change in Atwood number is small (4%). The goal is to study the physics without changing them, so a small Atwood number change is desirable. Although adding acetone to the gas causes the speed of sound to decrease, the increase in density allows the acoustic impedance to increase.

Table 1: Acetone-induced property changes in light gas (nitrogen). All values calculated referenced from EES software. Atwood number is calculated with carbon dioxide as the heavy gas.

	Pure Nitrogen	1:12 Acetone Mix	Saturated Acetone Mix
Density (kg/m^3)	1.166	1.188	1.455
Specific Heat Ratio	1.400	1.369	1.193
Atwood Number	0.225	0.216	0.117
Speed of Sound (m/s)	352.3	345.2	291.2
Acoustic Impedance (kg/m^2s)	379.3	410.1	423.7

3.2.1 PLIF Image Correction

In addition to correction of lens effects, variation among sensor pixels, and background noise, there are several corrections applied to the raw PLIF image to yield the concentration field [78]. Since the laser sheet is created using a plano-concave lens, the intensity in the PLIF images must be corrected for divergence. The transformed image intensity is corrected using

Equation 6

$$i^{trans} = i\frac{y_{int} - 1}{y_{int} - y}$$

where i is the intensity in the original image, y_{int} is the vertical location of the plano-concave lens (in pixels) relative to the top of the image, and y is the current vertical location, also relative to the top of the image.

With the knowledge that the light gas is pure ($\xi = 1$) far from the interface, the attenuation can be removed with the differential form of the Beer-Lambert law

Equation 7

$$\frac{dI}{ds} = -\varepsilon C_0 \xi I$$

where I is pixel intensity along the light ray, ε is the attenuation coefficient, C_0 is the pure light gas acetone concentration, ξ is normalized acetone concentration (C/C_0) a distance s along light ray [78]. The pixel intensity recorded by the CCD camera is

Equation 8

$$i = gC_0 \xi I$$

where g is a constant which describes the collection efficiency of the camera and optics system. Integrating Equation 7 yields

Equation 9

$$I_2 - I_1 = -\varepsilon C_0 \xi \int_1^2 I ds$$

substituting Equation 8 into Equation 9 gives

Equation 10

$$\frac{i_2}{g C_0 \xi_2} - \frac{i_1}{g C_0 \xi_1} = -\frac{\varepsilon}{g} \int_1^2 i ds$$

At this point it is important to realize that at the reference profile, $C = C_0$, so $\xi = 1$. The intensity at the reference profile in the free intensity region is defined to be i_1 and i_2 to be the intensity at any other location in the field. After rearranging, the concentration of acetone is

Equation 11

$$\xi = \frac{i(x,y)}{i_0(x) - \varepsilon C_0 \int_o^y i(x,y) dy}$$

It was found that since a large-amplitude perturbation is being studied, a diagonal reference profile was more appropriate than a horizontal one. An example diagonal reference profile can be seen in Figure 35. Therefore, if a diagonal free intensity region is also used, it must be compensated to account for the information at the top of the image (the dotted line in Figure 35). Since $\xi = 1$ in the pure gas at the top of the image, the difference between the intensity at the top and another location is given by

Equation 12

$$i_0(x) - i(x,y) = \varepsilon C_0 \int_0^y i(x,y) dy$$

Also, since the concentration in the light gas is constant throughout

Equation 13

$$i(x,y) = i_0(x) e^{-\varepsilon C_0 y}$$

Therefore, the compensated reference profile in the free intensity region is

Equation 14

$$i_0(x) = \langle i(x,y)e^{-\varepsilon C_0 y}\rangle_y$$

where the angled brackets indicate a spanwise average. The slope in the pure region will then be a constant $(-\varepsilon C_0)$.

The laser striations are removed by filtering a narrow band of wavelengths within Fourier space [59]. The first step in the process is to mirror the image to make a 3 x 3 array which will be periodic when taking the Fourier transform (Figure 34). A Hanning window is applied to this mirrored and padded image to remove any spectral leakage caused by non-periodicity in the image [58]. After taking the Fourier transform of this modified image, the laser striations appear as a bright horizontal band in Fourier space (Figure 34). This band is filtered and replaced with interpolated values from semicircles in Fourier space. The final step is to use the inverse Fourier transform to bring the image back to Real space.

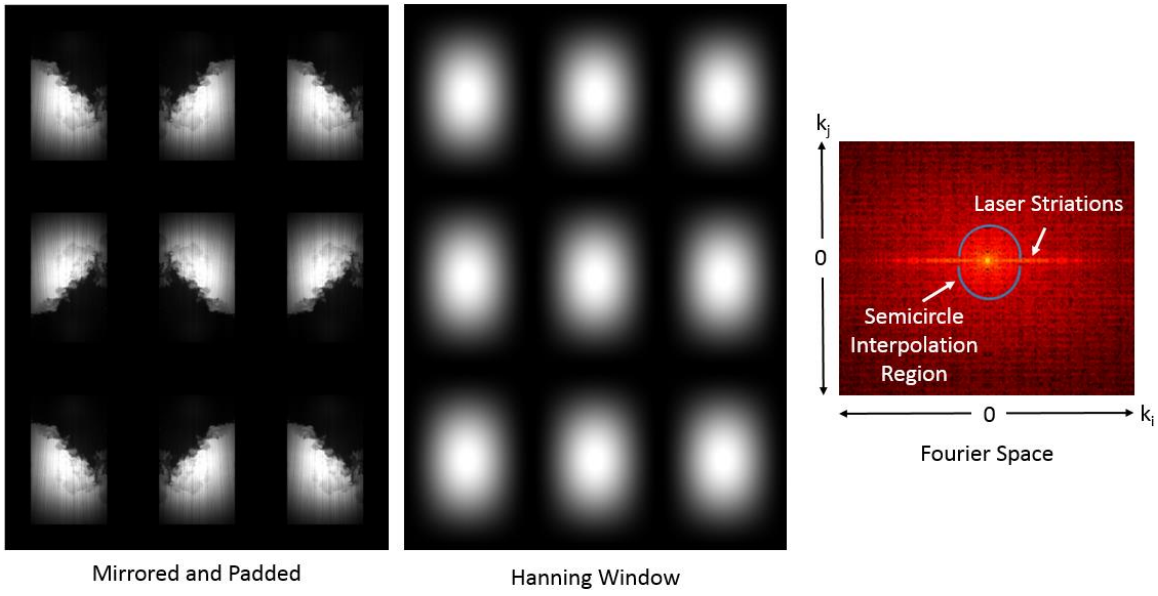

Figure 34: Notch filtering steps to remove laser striations shown graphically.

Figure 35 shows the main steps associated with the PLIF image correction. The image is first transformed so that the laser striations are straight. During the image transformation the bottom of the image is made larger so that the top of the image appears smaller in the spanwise direction by amounts dx_1 and dx_2 labeled in Figure 35. The values of these parameters depend on the location of the plano-concave lens used to create the light sheet. Then, after correcting for divergence, Beer-Lambert's law of attenuation is applied. In the final step, the laser striations are removed by filtering them in Fourier space. A close-up view of the mixing region is shown on the right of Figure 35 to demonstrate that features are preserved while the striations are removed. The concentration field can then be used to generate quantitative plots which describe scalar mixing. Because the flow dynamics are coupled with the scalar mixing, simultaneous PLIF/PIV measurements are required to gain a full understanding of the fluid instability. Simultaneous PLIF/PIV measurements will be discussed next.

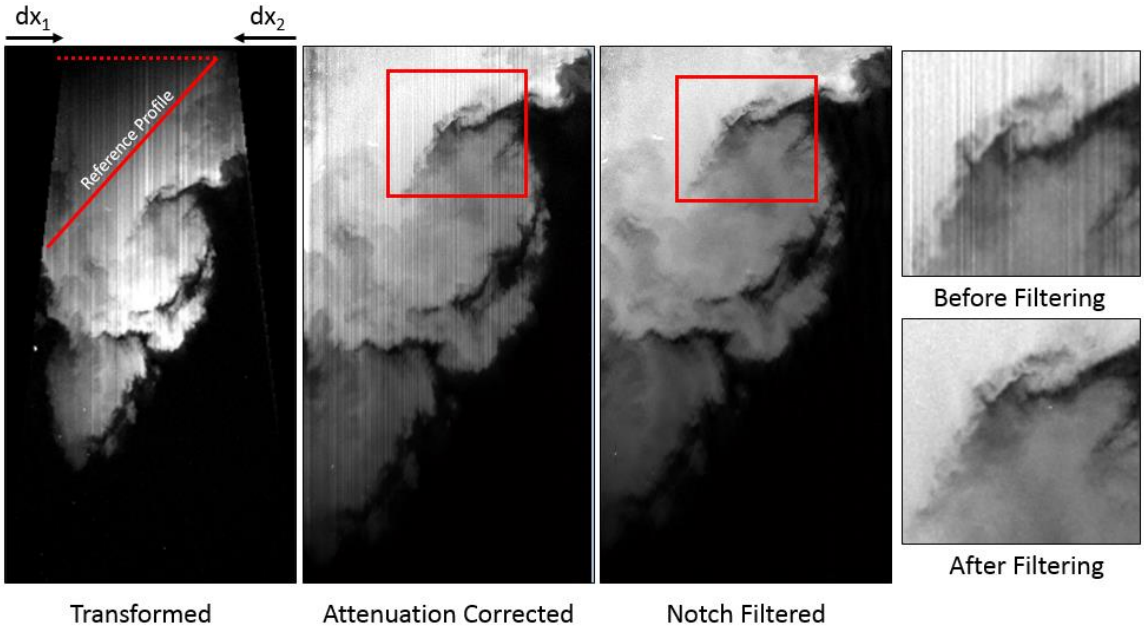

Figure 35: PLIF image correction steps shown graphically. Reference profile and transformation parameters are shown for reference. The notch filtered image is the final concentration field result.

3.3 Simultaneous PLIF/PIV Measurements

Acquiring PLIF and PIV data simultaneously requires a few modifications to the experimental facility. Since two lasers are used to provide the two wavelengths required for simultaneous measurements, a beam splitter is used to combine the laser beams. The combined beams then pass through a set of dual-wavelength mirrors which reflect > 90% of the laser beams at the angle of the inclined shock tube. The beams are transformed into a sheet using a plano-concave lens just before the fused silica window on the bottom of the shock tube. The sheet transformation is performed as close to the imaging location as possible to ensure that the laser sheet is as thin as possible. Filtering optics are used on the two lenses mounted on the CCD cameras to allow for separate measurements of the PLIF and PIV signals. The camera receiving the PLIF signal uses a notch filter which removes 532 nm as the center wavelength and a full width at half maximum (FWHM) of 26.6 nm. This allows most of the PLIF signal to be captured, the majority of which is between 420 nm and 520 nm. The camera receiving the PIV signal uses a bandpass filter with passes 532 nm as the center wavelength and has a FWHM of 10 nm. An additional complication is that since two cameras are facing the same window with the same field of view, one of the cameras must be tilted. The images coming from the tilted camera are corrected using a dewarping algorithm within Insight 4G^{TM}. Before this transformation is performed, calibration images are taken with a dual-plane calibration plate in the field of view (Figure 36). The dewarped images compare well with images from a camera which is not tilted. A sample set of transformed images is provided in Figure 37.

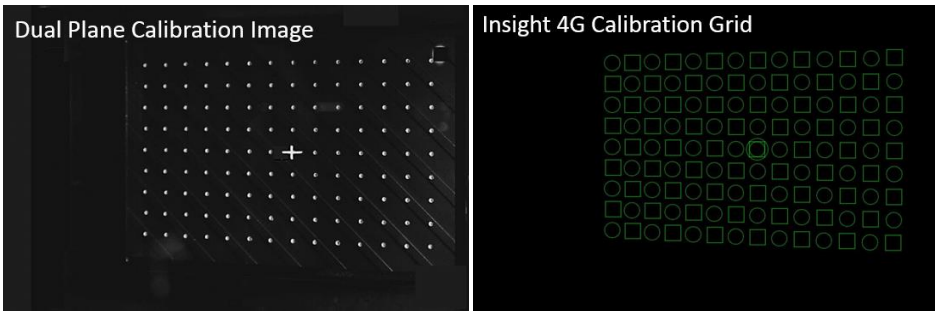

Figure 36: Left: Dual plane calibration image with point spacing of 1 cm in streamwise and spanwise directions, Right: Insight 4G calibration grid where squares and circles are on different planes.

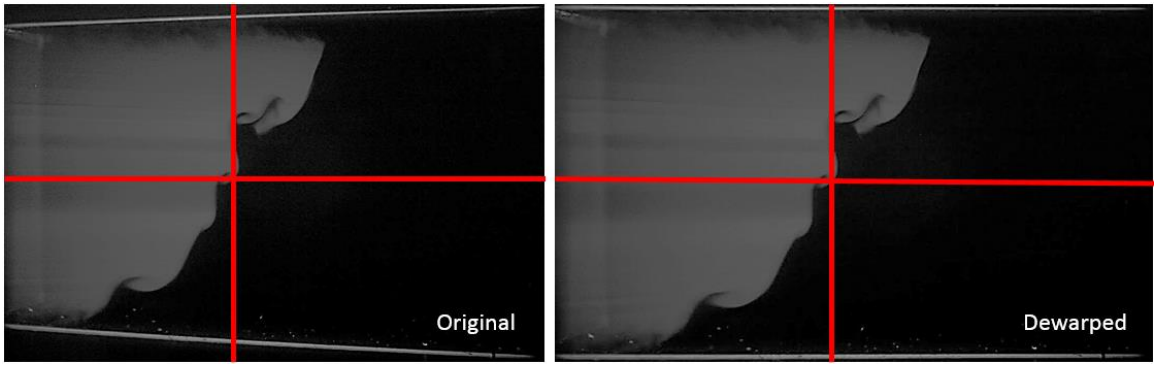

Figure 37: Original (left) and dewarped (right) raw PLIF images. Dewarping transformation performed with Insight 4G™.

CHAPTER 4: Experimental Results and Discussion

Although studying the complex initial condition before and after shock is the main focus of the current work, other experimental studies were carried out to better understand the RMI under a wide space of experimental parameters both before and after reshock.

4.1 Reshock Study

The goal of this study is to investigate the effects of reshock interaction time and vortex scales and distribution on the development of the inclined-interface Richtmyer–Meshkov instability. The developing interface of the inclined-interface RMI will be reshocked at three different stages of development (Table 2), each with a different level of vortex scales and distribution. A qualitative study will be presented through high temporal resolution Mie scattering images. Mixing width and interface length will be measured from the Mie scattering images to determine the interface growth rate, and particle image velocimetry will be used to map the velocity of the flow to generate vorticity fields and circulation data for a qualitative comparison. The Kolmogorov scale and Taylor microscale for the experimental cases will be calculated and used to analyze the turbulent kinetic energy spectra for each case. Finally, the turbulent kinetic energy spectra will be ensemble-averaged and normalized, and compared between the experimental cases.

Table 2: Definition of experimental cases.

	Case 1	Case 2	Case 3
IC to bottom wall	0.52 m	1.07 m	1.61 m
Development time	1.64 ms	3.50 ms	5.11 ms

4.1.1 Qualitative Results

Qualitative Mie scattering images were obtained for each of the three cases. All of the images were processed to remove background noise and vertical lines created by discontinuities in the wall facing the camera. Furthermore, the contrast between the region of unseeded CO_2 and the seeded N_2 was enhanced. The full-field view of the acquired Mie scattering images are presented in this section without cropping the boundary layers visible near the side walls. In Case 3, the interface stretched to the point that overlapping windows were required to capture the whole flow field featuring the interface. When this occurred, the images from two cameras were combined to make a single image. A discussion of the RMI before reshock is presented in previous work of McFarland et al. [75].

The qualitative images are summarized in Figure 38 for before and after reshock. Before reshock, Case 1 only shows inflection points, whereas Case 2 begins to show immature vortex structures, and Case 3 shows well-developed vortex structures with secondary vortices forming. These fractal-like Kelvin–Helmholtz rollups have been observed by Peng et al. [79] and result in increased vorticity deposition as well as a transition to turbulence. After reshock, feature C in Figure 38 grows larger and protrudes farther when moving from Case 1 to Case 3. Similarly, other features grow and develop with case progression. Case 3 begins to show multiple levels of intensity near the interface which suggest more mixing is occurring. However, PLIF would be a more appropriate diagnostic to determine scalar mixing and is investigated later in this work.

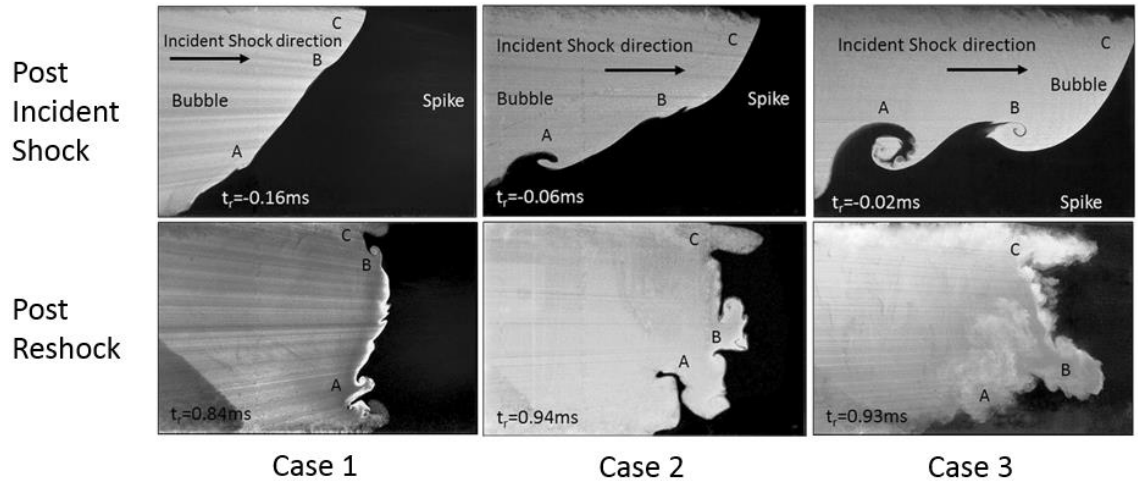

Figure 38: Three stages of development before and after reshock. All images were taken using Mie scattering diagnostic. Times are given relative to the time of reshock.

4.1.2 Quantitative Results

Mixing Width Data

The Mie scattering images provide an estimate of the mixing at the interface by calculating the mixing width, as the 5% and 95% divisions between the two gases. To calculate the mixing width, the boundary layers are cropped, and the image is converted into a binary image using an intensity threshold. The intensity threshold is the pixel intensity below which a pixel will be changed to zero and above which it will be converted to one. The threshold was chosen to accurately represent the fluid interface. Once the image is purely black and white, the columns of pixels where the image is 5% and 95 % white are determined starting from the edge of the image and progressing inward, and the pixel distance between the columns is recorded. The pixel distance is converted into a dimensional distance using the calibration image. The mixing width measurements for the images in the three experimental cases are presented with data from initial shock development in Figure 38. The mixing width data are used to calculate the

mixing width growth rate by applying a linear regression to the data points after reshock that follow a linear trend for all three cases. These growth rates, as shown in Table 3, show that the interface stretches during the initial development. The growth rates after reshock are slightly higher for more developed cases.

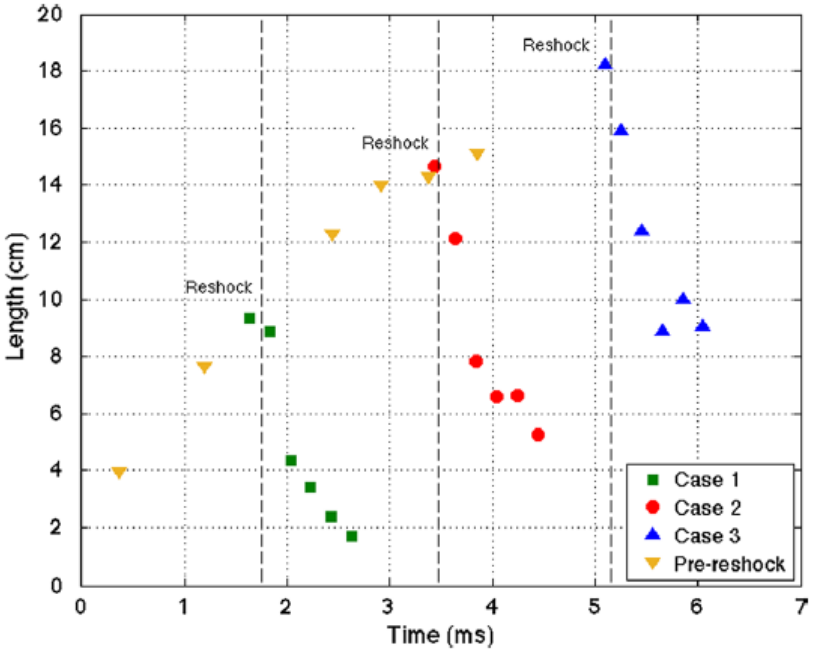

Figure 39: Mixing width data for Cases 1, 2, and 3.

Table 3: Interface growth rates for all three cases before and after reshock.

Case	Before or after reshock	Mixing width growth rate (m/s)	Interface length growth rate (m/s)
1	Before	29.7	44.16
	After	-83.76	15.61
2	Before	29.7	44.16
	After	-92.27	85.41
3	Before	29.7	44.16
	After	-97.75	-33.96

Vorticity, Circulation, and Enstrophy

All of the vector sets were generated using TSI Insight^{TM} 4G and post processed using Matlab. The delta *t* between PIV images was chosen so that the interface would travel approximately 8 pixels or 0.1944 mm, given a pixel size of 0.1143 mm. Because the interface velocity was found to be approximately 250 m/s, the time between PIV frames was 5 μs. The post-reshock velocity was calculated to be approximately 40 m/s, which yielded a delay time of approximately 25 μs. The vectors were created using a recursive Nyquist grid with a starting spot size of 36-by-36 pixels and a final spot size of 26-by-26 pixels, fast Fourier transform (FFT) correlation, and a Gaussian mask with a signal-to-noise threshold of 1.2. Holes in the vector field were filled using linear interpolation. For the pre-reshock cases, between 2 and 5 % of the vectors were interpolated, and for the post-reshock cases, between 10 and 15 % of the vectors were interpolated.

The vorticity was calculated from the curl of the 2D velocity field for all three experimental cases. The "gradient" function in Matlab was used. The calculated numerical derivatives produced a noisy vector field. The PIV process creates velocity vectors that are in an array based on the final spot size. The array spacing can prevent gradients from being accurately represented if noise is present in the velocity vectors. To obtain more accurate derivatives, empty spaces in the vector fields were filled using linear interpolation of nearby values and then the field was smoothed using a median filter with a bin size of 11-by-11 pixels. In Figure 40, the boundary layers are clearly identifiable in the vorticity field as layers of positive and negative vorticity. The boundary layers were cropped for all of the calculations in this work.

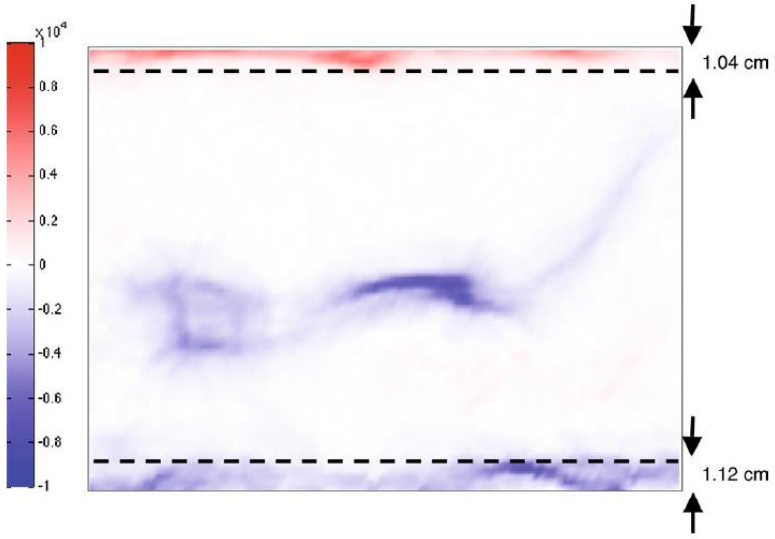

Figure 40: A vorticity field for Case 3 pre-reshock showing the boundary layers which are cropped.

The vorticity fields for all three cases before and after reshock are presented in Figure 41. Beginning with the least temporally developed case, Case 1, the interface before reshock, as shown in Figure 41 A, has no defined vortex structures but does possess many inflection points. This shape is also evident in Figure 41 B where the interface is portrayed as a diffuse line of negative vorticity that is devoid of defined vortex structures, but shows stronger vorticity in areas corresponding to the inflection points of the interface. After reshock, the interface is shown as a diffuse line of positive vorticity with regions of stronger vorticity which correspond to the developed structures formed from the pre-reshock inflection points. The vorticity at the interface is reversed due to the additional baroclinic torque. Furthermore, the inflections present before reshock begin to manifest themselves as small structures that can be seen in the vorticity plot post-reshock (Figure 41 D).

The pre-shock vorticity plot for Case 2 shows the small vortex structure that is starting to form near the trailing edge of the interface as well as the small protrusion that

is starting to extend from the interface. After the reshock interaction, the second application of baroclinic torque reverses the direction of the vorticity of the interface. This pocket of negative vorticity corresponds to the structure that was a defined vortex structure prior to reshock. Similar to the structure that is shown in the Mie scattering image in Figure 41, the areas of large vorticity correspond to the structures of the interface. The line of negative vorticity is also present after reshock for this case where the initial conditions are more developed.

Case 3 is the most developed pre-reshock interface and as such, has larger regions of strong vorticity within the diffuse representation of the interface. The multiple large structures in the pre-reshock interface are converted into pockets of negative vorticity by the second application of baroclinic torque and turns the bulk of the interface from negative to positive vorticity. The large areas of both negative and positive vorticity support the mixing that is inferred from the Mie scattering images.

The vorticity data collected for multiple runs for each case both before and after reshock were integrated over the flow field to determine the total enstrophy and circulation present, as shown in Table 3. The circulation is

Equation 15

$$\Gamma(t) = \iint_S \vec{\omega} \cdot d\vec{S}$$

where $\vec{\omega}$ is the vorticity and $d\vec{S}$ is a differential area element. Enstrophy is a measure of the rotational energy in the flow field at a given time and location.

Equation 16

$$\Omega(t) = \frac{1}{2} \iint_S \vec{\omega}^2 \cdot d\vec{S}$$

Enstrophy calculations for experiments at the same time were ensemble-averaged.

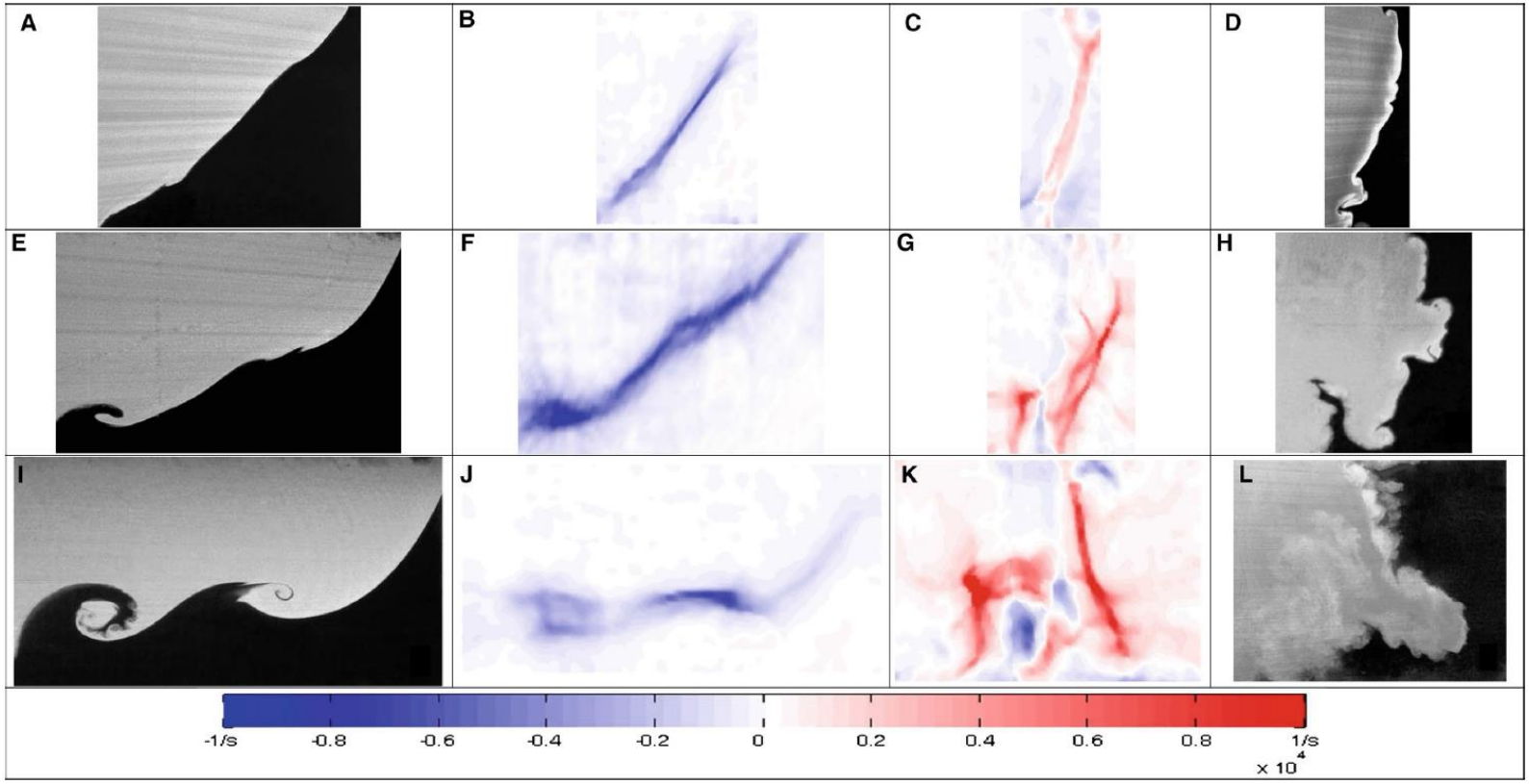

Figure 41: Vorticity fields for the entire flow field with corresponding Mie scattering images: Case 1 before (a, b) and after (c, d) reshock interaction, Case 2 before (e, f) and after (g, h) reshock.

Table 4: Circulation and enstrophy statistics for all three cases before and after reshock.

Case	Before or after reshock	Number of experiments	Ensemble average Enstrophy $(m/s)^2$	Ensemble average circulation (m^2/s)	Standard deviation (m^2/s)	Coefficient of variance (%)
1	Before	10	6.27×10^{-3}	-3.218	0.119	3.71
	After	10	6.81×10^{-3}	3.893	0.307	7.88
2	Before	8	6.83×10^{-3}	-3.845	0.147	3.82
	After	10	1.83×10^{-2}	7.246	0.283	3.91
3	Before	9	1.21×10^{-2}	-3.742	0.212	5.66
	After	8	3.55×10^{-2}	8.862	0.312	3.52

The enstrophy increases after reshock which shows that there is more local rotation occurring in the post-reshock flow fields. As the large, coherent structures of the interface break down during the post-reshock development and smaller-scale structures develop, the rotational motion of the flow is enhanced locally as it is dissipated from the larger scales. Case 1 has fewer coherent structures than the other cases post-reshock, and therefore, its post-reshock enstrophy is found to be less than that of Cases 2 and 3. As expected, Case 3 is found to have more post-reshock enstrophy than Case 2.

Velocity Statistics

Important to understanding turbulent flows are Reynolds stresses or turbulent stresses which depend on velocity fluctuations, both streamwise and spanwise, and account for turbulent fluctuations in fluid momentum. The Reynolds stresses in a Richtmyer–Meshkov fluid mixing layer were recently studied by Balakumar et al.[43]. The streamwise velocity fluctuation is defined as

Equation 17

$$u' = u - \bar{u}$$

where u is the streamwise velocity and $\bar{u}$ is the spatially averaged streamwise velocity. The spanwise velocity fluctuation definition is of the same form.

The variation in streamwise and spanwise velocity fluctuations was plotted across the mixing width for each case before and after reshock (Figure 42). All of the variances were ensemble-averaged over ten separate experiments. The streamwise velocity variance pre-reshock is an order of magnitude larger than the spanwise velocity variance, which indicates that there is anisotropy present in the flow field in the direction of shock propagation. The nonzero cross correlation ($\overline{u'v'}$) between the streamwise and spanwise velocity fluctuations indicates that there is shear present
in the flow which leads to the Kelvin–Helmholtz rollups visible in the Mie scattering images. Furthermore, in Case 3 pre-reshock there is a bimodal distribution in $\overline{u'^2}$ due to the two vortex structures that form. There is a trend of increasing streamwise velocity fluctuation variance from Case 1 to Case 3. Moreover, the streamwise velocity fluctuation variance increases by a factor of four after reshock for Cases 2 and 3, but remains nearly unchanged for Case 1. For the most developed case, Case 3, the maximum streamwise velocity fluctuation before reshock is ~7 % of the bulk fluid velocity.

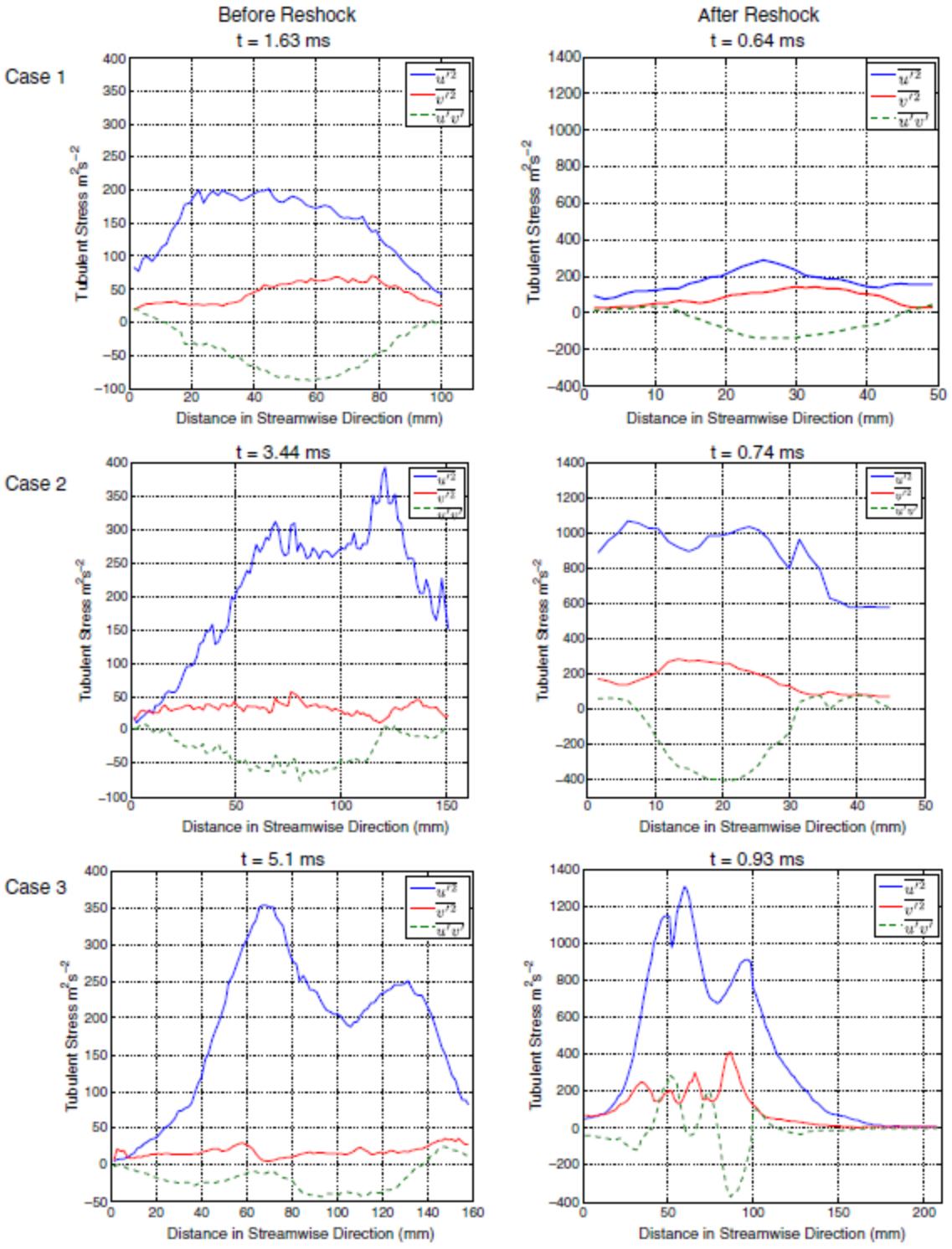

Figure 42: Variances of velocity fluctuations across the mixing width in the streamwise direction before and after reshock interaction for Cases 1, 2, and 3 (the post-reshock times are relative to when reshock happens, whereas the pre-reshock times are relative to the incident shock time).

2-D Turbulent Kinetic Energy

An approximation of the turbulent kinetic energy (TKE) spectrum using available 2D data was used to quantify the scales over which energy is distributed. The method used to calculate the spectra presented in this work is similar to the method used by Latini et al. [80] with the exception that density weighting was not employed. First, vorticity plots for each case were examined and the boundary layers (clearly visible in the vorticity plot) were cropped. Because only half of a wavelength is studied in the inclined shock tube, the PIV data were reflected across the bottom, horizontal boundary (the floor of the shock tube). This resulted in one full wavelength, which is periodic when taking the Fourier transform. The u' and v' components of turbulent kinetic energy are given by

Equations 18

$$K_{u'} = \frac{1}{2}\overline{u'^2}$$

$$K_{v'} = \frac{1}{2}\overline{v'^2}$$

where u' and v' are the streamwise and spanwise components of the fluctuating velocities, respectively. The energy spectra components were computed by taking the FFT of each column of fluctuating velocities in the spanwise direction and multiplying it by its complex conjugate

Equations 19

$$[E_{u'}]_i = FFT(u') \cdot conj(FFT(u'))$$

$$[E_{v'}]_i = FFT(v') \cdot conj(FFT(v'))$$

where $[E_{u'}]_i$ is the u' component of the energy spectra for the i^{th} column. The energy spectra were calculated by adding the u' and v' components.

Equation 20

$$[E]_i = \frac{1}{2}[[E_{u'}]_i + [E_{v'}]_i]$$

After the energy spectra were averaged across all the columns, only the first half was retained due to the Nyquist sampling frequency restraint. This procedure was performed on approximately ten instantaneous realizations for each case; thus, the overall average used 4340 columns of velocity data, including mirrored ones.

Figure 43 compares the average spectra for all three cases before and after reshock. In all cases, the reshock wave causes an amplification of turbulent kinetic energy which is seen at all wavenumbers. Cases 2 and 3 TKE is amplified by approximately one order of magnitude. WENO simulations [72] of a 3D reshocked RMI also showed approximately one decade of amplification of TKE upon reshock. Case 1 has a much smaller increase in TKE because fewer small scales have formed. Cases 1 and 2 pre-reshock begin to follow a $k^{-5/3}$ power law for a small range of wavenumbers, whereas Case 3 pre-reshock follows this trend for a larger range. As the interface is given a longer time to develop prior to reshock, it approaches a turbulent state. The complexity of the Case 3 interface leads to a redistribution of energy over a large range of scales upon reshock. After reshock, all three cases follow a $k^{-5/3}$ power law for a larger range of wavenumbers, with Case 3 following this trend for the largest range (approximately one decade). This trend indicates that energy contained at large wavenumbers is converging toward an isotropic state [81]. The sharp decline at the highest wavenumbers is due to aliasing effects. Energy in the dissipation range cannot be measured here due to limitations in PIV resolution.

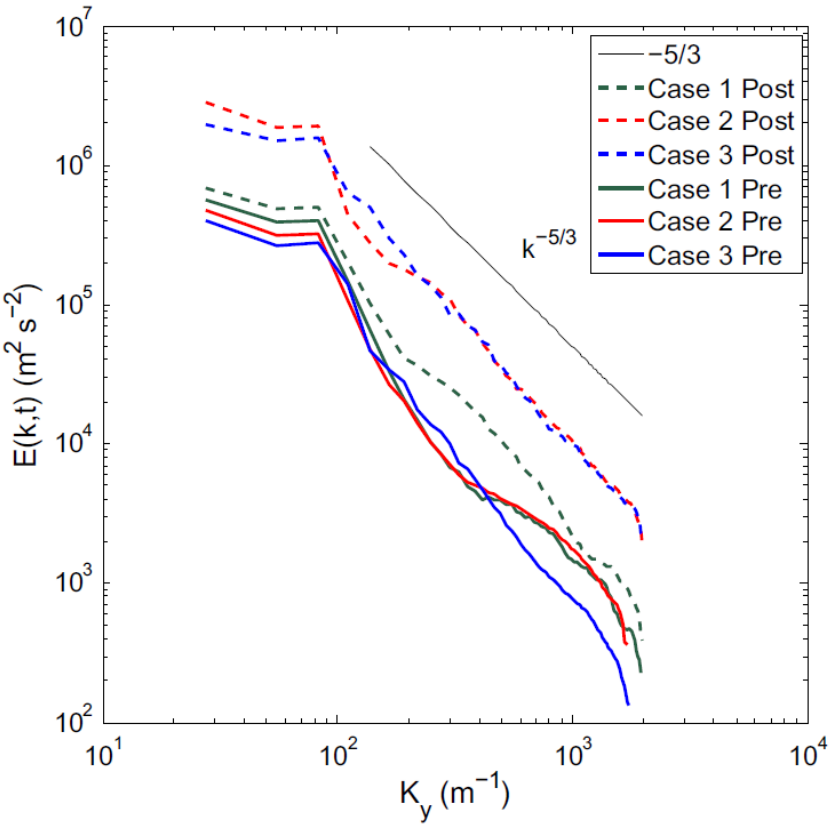

Figure 43: Ensemble-averaged approximate turbulent kinetic energy spectra for all three cases for before and after reshock with $k^{-5/3}$ fiducial.

4.2 Parametric Study

A parametric study was conducted which was designed to determine the effect of Atwood number, Mach number, and inclination angle, as well as to experimentally validate a scaling law which has only been validated with simulations until now. Changing the angle allows the baroclinic torque to be modified while holding all others parameters constant, a unique capability of this facility. Four cases were chosen which effectively swept the parameter space (Table 5).

Table 5: Parametric study parameters.

Gas Pair	Mach Number	Angle
N_2/CO_2	1.55	60°
N_2/CO_2	1.55	80°
N_2/CO_2	2.01	60°
N_2/SF_6	1.55	60°

4.2.1 Inclined Interface Growth Model

McFarland et al. [67] developed a growth model to scale growth rates for both linear and nonlinear perturbations. Traditionally, the linear growth regime has been defined as $\eta/\lambda << 1$, where η is the amplitude, and λ is the wavelength. The wavelength for the perturbation in the current study is twice the width of the shock tube since only half of a triangular wave is studied. The starting point for the new growth model was the Richtmyer impulsive growth model which was developed in 1960 based on his contemporary's work in 1950 [14].

Equation 21

$$\dot{\eta}_0 = k[v]A'\eta_0'$$

where $\dot{\eta}_0$ is the interface growth rate, k is a scaling constant, $[v]$ is the interface velocity jump, A' is the post-shock Atwood number, and η_0' is the post-shock initial amplitude.

The first attempt at developing a new scaling model was to adapt the Richtmyer impulsive model. The name of the new model is the adapted Richtmyer impulsive model (ARIM) [67]. The equations that define the model are

Equations 22

$$\tau = k\dot{\eta}_0(t - t^*)$$

$$\bar{\eta} = k(\eta - \eta_0')$$

$$\dot{\eta}_0 = k\eta_0'A'[v]$$

$$t^* = \lambda/(2w_i \tan\theta)$$

$$\eta_0' = \eta(t^*)$$

where τ is nondimensionalized time, t^* is an offset time which ensures the initial ARIM amplitude is zero, $\bar{\eta}$ is a nondimensionalized amplitude which is also offset by the post-shock amplitude, λ is the perturbation wavelength, w_i is the incident wave speed, and θ is the angle of the interface. A detailed motivation and development of this model can be found in the work by McFarland et al. [67].

The ARIM scaling was not found to fully capture the effects of interface geometry and initial nonlinear compression, so it was modified to become the inclined interface scaling (IIS). A parameter which changed was the nondimensionalized time

Equation 23

$$\tau = \frac{A(t - t^*)}{t_{char}}$$

where t_{char} is a characteristic time calculated using the shock wave speed (w_i) and a characteristic or "effective" length ($\lambda_E = \lambda \tan\theta$) [67]. Another difference in this model is that a different offset time was used which takes secondary compression waves into account. This model will be investigated using the experimental data collected in this study.

4.2.2 Qualitative Results

Qualitative and uncorrected PLIF images are shown in this section. The first case shown in Figure 44 and Figure 45 is for nitrogen over carbon dioxide at an inclination angle of 60° and a Mach number of 1.55. This is the same as Case 3 in the reshock study except that it is now being studied with the PLIF diagnostic. As before when the Mie

scattering diagnostic was used, two vortex structures form before reshock occurs. The reshock wave is seen traversing the interface in Figure 45. It is curved due to the difference in the speed of sound in the two gases. The phase inversion of the bubble and spike is complete by 1.55 ms. The series extends to 3.55 ms, which is still before the expansion waves from the driver reach the interface.

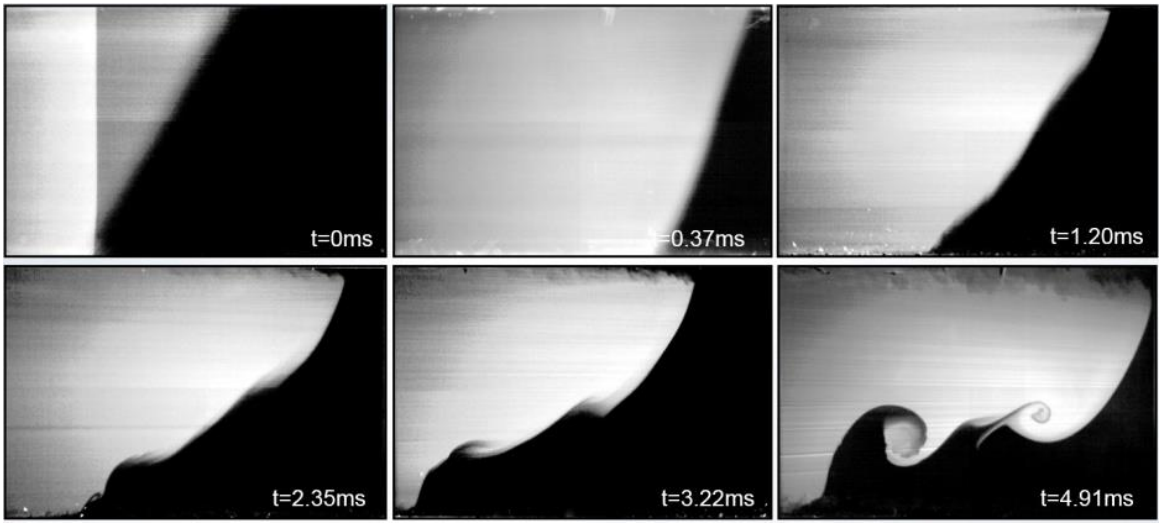

Figure 44: N_2/CO_2, M-1.55, θ-60°, PLIF image set before reshock.

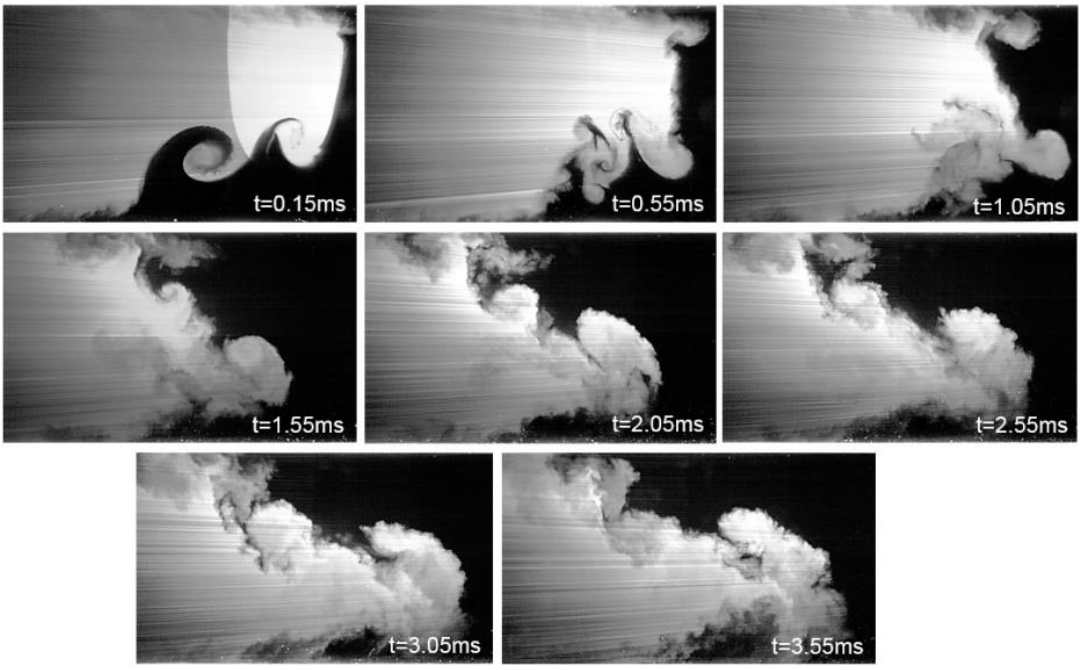

Figure 45: N_2/CO_2, M-1.55, θ-60°, PLIF image set after reshock.

The second case considered changes the angle of inclination from 60° to 80° (Figure 46 and Figure 47). This is similar to the "tilted-rig" test problem which is based on experiments performed at AWE in the late 1980's which has subsequently become a test bed problem for numerical modelers [82]. The 80° inclination angle results in a 10° tilt angle off of the vertical (90°). Before reshock, there are multiple vortex structures which are beginning to form but are not well-developed. Unlike the first case, little evidence is seen of secondary vorticity deposition. After reshock, this interface looks very similar to the one in case one, suggesting that there may be a loss of memory of initial conditions.

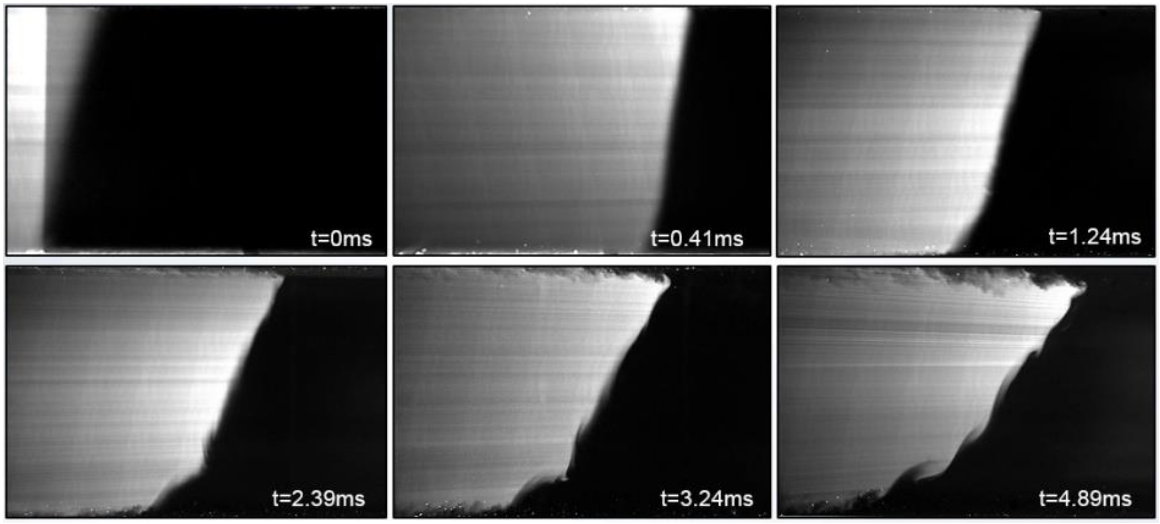

Figure 46: N_2/CO_2, *M*-1.55, θ-80°, PLIF image set before reshock.

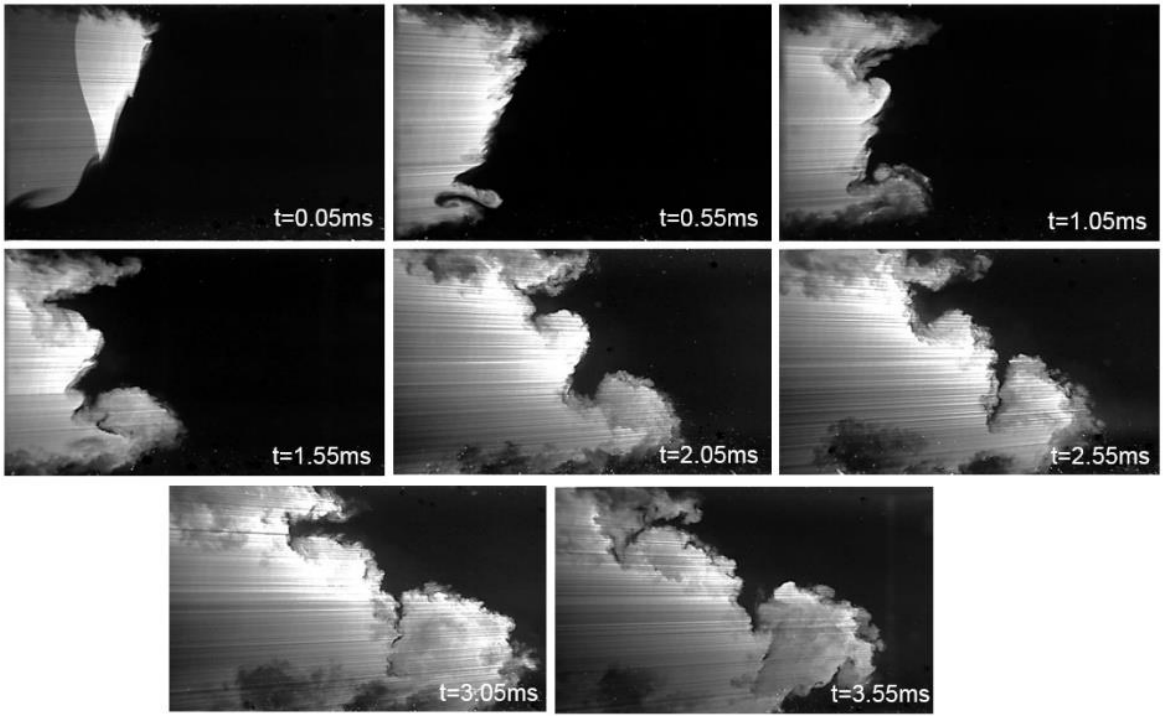

Figure 47: N_2/CO_2, *M*-1.55, θ-80°, PLIF image set after reshock.

The next parameter which changed relative to the first case is the Mach number, which is now 2.01 (Figure 48). The interface traveled much quicker in this case and reaches the farthest downstream imaging location in only 2.66 ms. It appears that at late time three or four vortex structures form. The two structures near the tip of the bubble appear to be merging. If this case were to be studied using PIV, the author would recommend using solid particles, since the higher temperature post incident shock and reshock will cause many oil-based seed particles to disappear. Images are not provided for after reshock for this case since the long acrylic window used for reshock experiments have not yet been tested at the higher pressures associated with Mach 2.01 experiments.

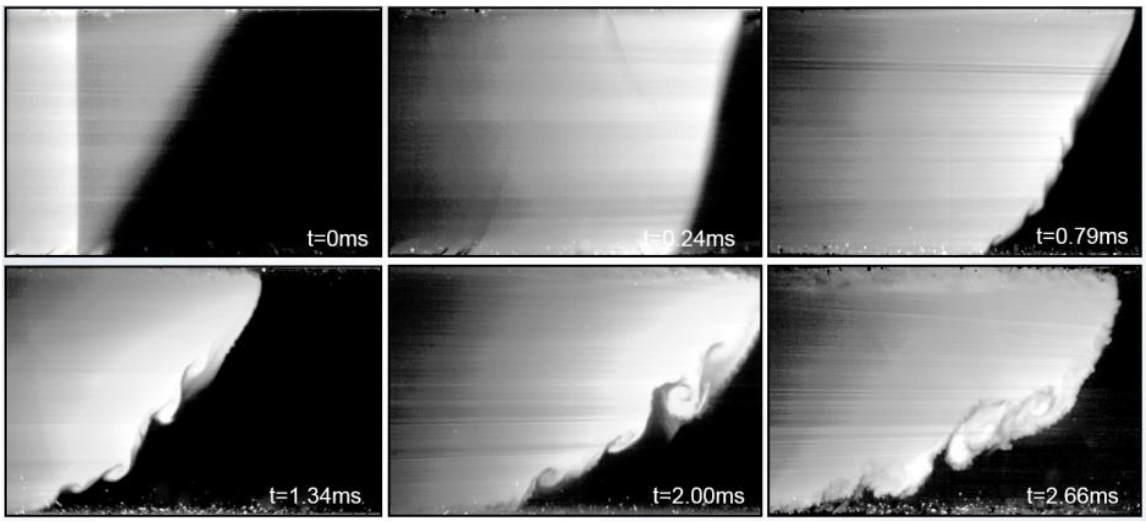

Figure 48: N_2/CO_2, M-2.01, θ-60°, PLIF image set before reshock.

The last case utilizes a higher density-contrast by placing nitrogen over sulfur hexafluoride (SF_6), which results in an Atwood number of 0.67 (Figure 49 and Figure 50). This increase in the density mismatch is expected to lead to an increase in stretching as predicted in Richtmyer's impulsive growth model [14]. By 1.68 ms, the spike has grown to be very narrow, while the bubble appears to have two vortex structures forming. At the latest time before reshock three vortex structures are visible, although they do not have well-defined cores as in the first case. Most of the perturbations are damped out after reshock (Figure 50).

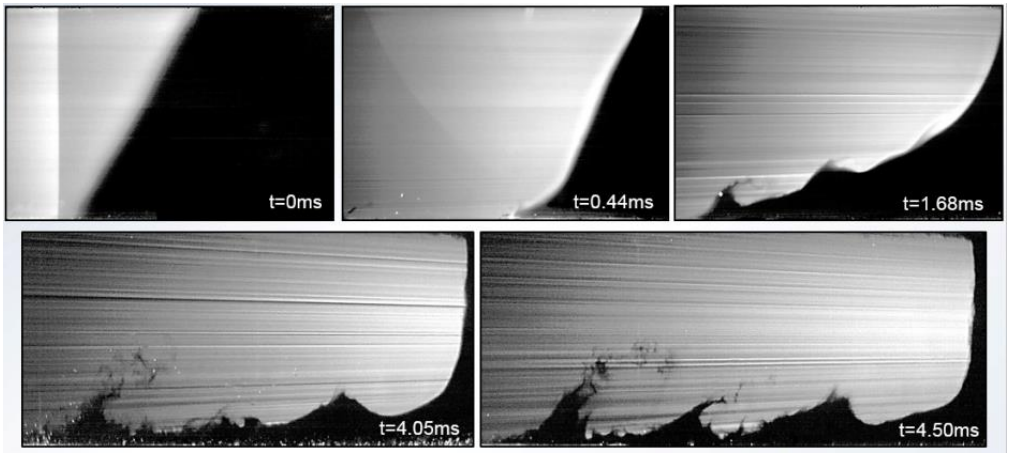

Figure 49: N_2/SF_6, M-1.55, θ-60°, PLIF image set before reshock.

Figure 50: N_2/SF_6, M-1.55, θ-60°, PLIF image after reshock (t~8 ms).

4.2.3 Quantitative Results

The quantitative results will seek to validate the inclined interface scaling relationship referenced earlier as well as Ares simulations performed by McFarland et al. at Lawrence Livermore National Laboratory (LLNL) [70]. The first quantitative measure considered is the integral mix width defined as

Equation 24

$$h = \int \langle Y_{N_2} \rangle \langle Y_{CO_2} \rangle dx$$

where Y is the mass fraction of either of the species. This is an alternative to the 5% to 95% mixing width definition used earlier. Figure 51 shows that good agreement is found between the experiments and Ares simulations. A maximum deviation of 10% between experiment and simulation is found after reshock.

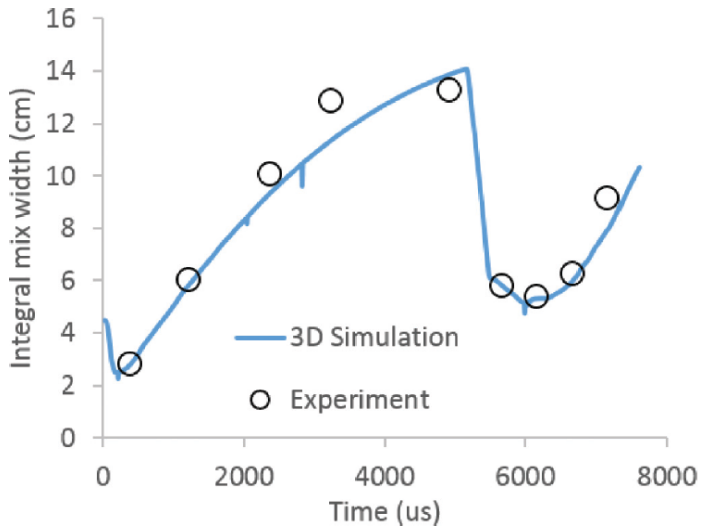

Figure 51: Integral mixing width comparison for experiment and Ares simulation (N_2/CO_2, M-1.55, θ-60°) [70].

The unscaled mixing width for all four cases is shown in Figure 52. After reshock, the mixing widths for the first and second cases (where angle is changed) reach almost the same value and follow the same trends, suggesting a loss of memory of the initial conditions. Jacobs et al. [54] also found that when different random initial perturbations were shocked, the post incident shock mixing widths departed, but after reshock, the results were much more consistent. Ares simulations of the 60° and 80° simple inclined interfaces also show integral mix widths which converge after reshock [70]. Only the 80° case ($\eta/\lambda \ll 1$) experiences linear growth before reshock as expected.

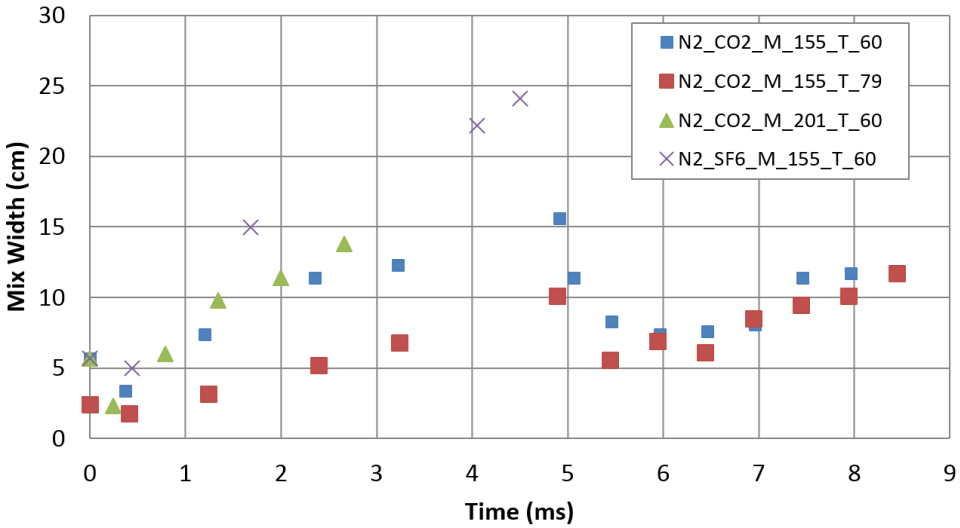

Figure 52: Parametric mixing width data plotted for four cases. The mixing width and time are not scaled.

The mixing width scaled using the inclined interface scaling technique discussed earlier is shown in Figure 53. All of the non-linear cases collapse well at late time. However, the model appears to have some deficiencies with regard to early time scaling of the higher-Atwood number case. As discussed by McFarland et al. [67], the model is sensitive to the details of the initial shock refraction problem and may not be properly accounting for high-Atwood number effects. The linear case (80°) follows a separate trend as expected.

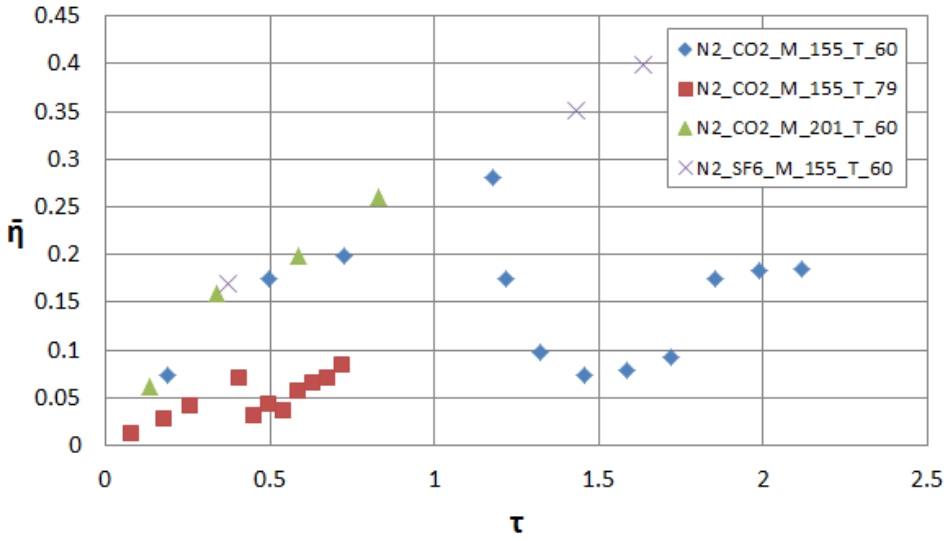

Figure 53: Parametric mixing width data plotted for four cases. Both the mixing width and time are nondimensionalized.

Positive, negative, and total circulation for the first case is plotted against Ares simulations in Figure 54. A full description of 3D Ares simulations is given in [69]. Circulation increases initially but then levels out to a nearly constant value until late time before reshock. A sharp increase in circulation is seen at reshock. This is due to the additional application of baroclinic torque by the reshock wave. Simulations show good agreement with experiments both before and after reshock. Some of the discrepancies may be due to the resolution limits of the cameras used for PIV.

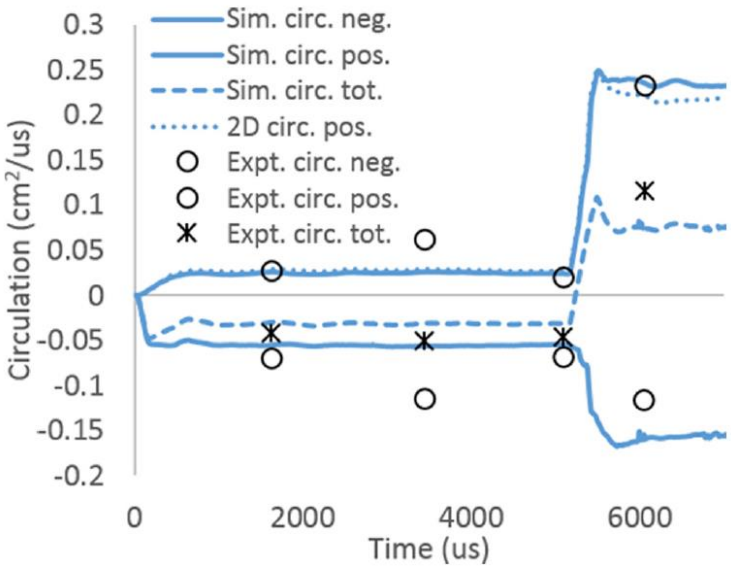

Figure 54: Positive, negative and total circulation for experiment and Ares simulation (N_2/CO_2, M-1.55, θ-60°) [82].

The last comparison with simulations is for 2D turbulent kinetic energy (Figure 55). The two times chosen for comparison (5.1 ms and 6.2 ms) are for before and after reshock, respectively. The data from experiments is an ensemble average from 10 experimental trials. The simulation data extends to higher wavenumbers because of the superior resolution compared to experiments (1.6 mm resolution for experiments). The slope that the simulation follows at high wavenumbers is most likely not physical but due to numerical effects. The experimental data appears to develop an inertial range even before reshock, whereas simulations do not until after reshock, although this is difficult to say with limited data. It could be that the simulations are not fully capturing some aspect of the experiments.

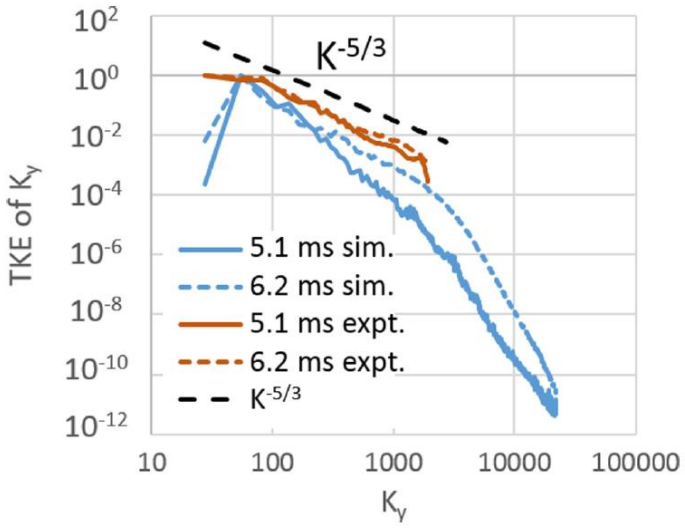

Figure 55: Normalized turbulent kinetic energy spectra for simulation and Ares simulation (N_2/CO_2, M-1.55, θ-60°) [82].

4.3 Complex Interface Study

The complex interface study was conducted to determine the effect of initial conditions on late-time compressible turbulent flow fields. In these types of flow the mixing is coupled to the dynamics. This type of mixing is what Dimotakis [50] referred to as Level-2 mixing, which is typically separated from Level-1 mixing based on baroclinic vorticity (resulting from pressure and density gradients) or by temperature and entropy gradients. The mixing studied here could not be categorized as Level-3 mixing since the fluid does not change. When the material mixing at the interface is coupled with the velocity field, it is important to be able to make simultaneous measurements of both scalar and vector quantities which describe the overall evolution of the flow field. This study will start by characterizing the initial conditions and then investigate the interface evolution using simultaneous diagnostics.

4.3.1 Initial Condition Characterization

The complex interface was created by counter flowing both heavy and light gases as described earlier in Figure 31. The flowrates which were used are recorded in Table 6. The bypass flowrate for nitrogen includes both the pure stream as well as the one seeded with acetone. It was found that the interface was becoming exceedingly diffuse and structures were not well formed unless a vacuum pump was used to reduce the residence time of each gas in the shock tube. Suction was applied to the interface exit slots so that the driven pressure was ~ 0.2 psig.

Table 6: Flowrates used to create complex interface.

Gas	Bypass (LPM)	Jet (LPM)
Nitrogen	26	3
Carbon Dioxide	9	2.5

The velocity and vorticity fields for an instantaneous realization of the initial condition are shown in Figure 56. The jets near the interface create two layers of positive and negative vorticity. In contrast, the inclined interface initial condition simply has a patch of positive vorticity near the top slot and a negative one near the bottom slot.

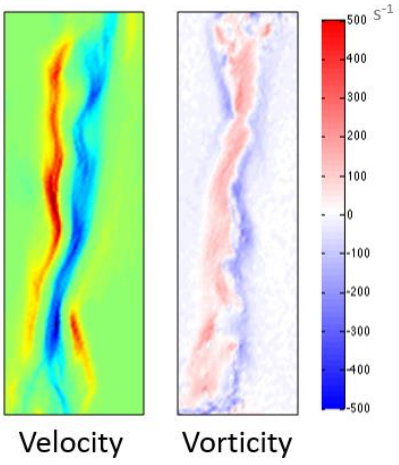

Figure 56: Velocity and vorticity fields for complex initial condition.

A set of 100 PLIF images of the initial condition were taken and used to compute the standard deviation of the pixel intensity near the interface in order to assess the statistical steadiness of the initial conditions. The maximum standard deviation was found to be 0.1. Since variations in laser power also increase the standard deviation, this is a conservative estimate of the interface variation.

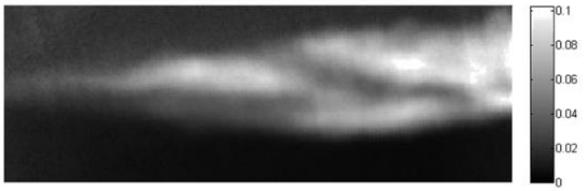

Figure 57: Standard deviation of 100 PLIF images of complex initial condition. Maximum value is 0.1.

Another way the complex interface can be quantified is through a Proper Orthogonal Decomposition (POD), also called Principal Component Analysis (PCA) or Singular Value Decomposition (SVD). This is an orthogonal transformation which converts a set of observations into a set of linearly uncorrelated variables. It allows the modal content to be extracted from an ensemble of signals, which can be scalars or vectors. The first mode or component is defined so that it accounts for the largest amount of variability in the data set. Berkooz, Holmes, and Lumley [83] provide an excellent overview of the use of POD analysis for studying turbulent flows.

The basics of POD analysis can be explained very simply using fundamental concepts of linear algebra. If M is a matrix whose entries came from a field of real numbers, then the singular value decomposition is

Equation 25

$$M = U\Sigma V^*$$

where U is an $m \times m$ unitary matrix, Σ is an $m \times n$ diagonal matrix (positive real numbers), and V^* is an $n \times n$ unitary matrix, where V^* is the conjugate transpose of V. The Σ matrix holds what are called the singular values of M. For the analysis in the current work, a built-in Matlab function called "svd" was used to calculate the snapshot SVD.

The first three modes from the POD analysis of 300 scalar fields for the complex initial condition are shown in Figure 58. Mode 0 is the first and dominant mode. This mode shows that the underlying inclined interface perturbation is the most prominent feature. Higher-order modes show vortices shedding from the interface as well as mushroom structures resulting from the unstable density stratification caused by the fluid injection. The first 50 modes are plotted in Figure 59. If the modes are plotted cumulatively (red triangles), it is clear that the first 50 modes describe ~90% of the scalar information content (the analog to energy if a vector field were used). The interface could be reconstructed using the first 50 modes and used as a "representative" interface that best describes the most important modes.

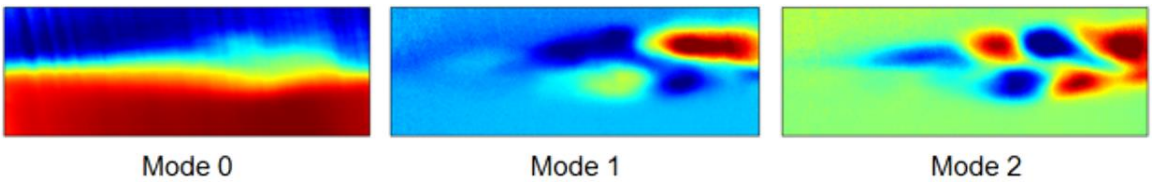

Figure 58: First three POD modes plotted using jet color map. Mode 0 is the dominant mode.

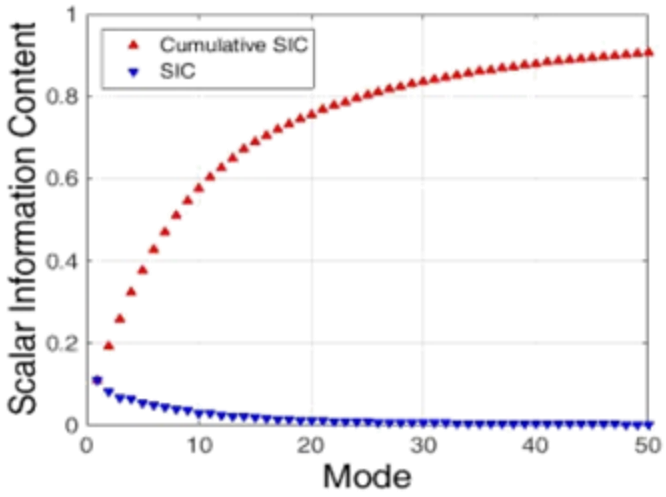

Figure 59: Scalar information content calculated using the snapshot POD method and 300 PLIF images. Only the first 50 modes are shown.

4.3.2 Qualitative Results

It is useful to consider the qualitative evolution of complex interface and compare it to previous cases to understand the effect of angle and modal content. Figure 60 presents PLIF images for inclined interface at two angles (60° and 80°) as well as the complex interface (80°). Comparing the two inclined cases, there is clearly more vorticity deposited in the 60° case. This makes sense because the only thing that changed between the two cases is the angle, which changed the strength of the baroclinic term in the vorticity equation. The increase in circulation expected when changing the angle from 80° to 60° is expected to be 2.9 times (sin(30°)/sin(10°)). The experimental increase in circulation was found to be 2.6 times. This difference between the analytical and experimental results can be partially attributed to experimental uncertainty and resolution. It is expected that the analytical and experimental results would compare better at earlier time before the strength of the vorticity has had time to decay. After reshock, it appears that the memory of the initial conditions has been erased.

The complex interface has approximately the same mixing extent as its inclined counterpart, but visibly shows an increase in mixing. Furthermore, the underlying inclined interface perturbation for the complex case is still visible even at late time. This suggests that there may be some signature of the initial condition in a case which undergoes greater mixing and may be transitioning to a turbulent state.

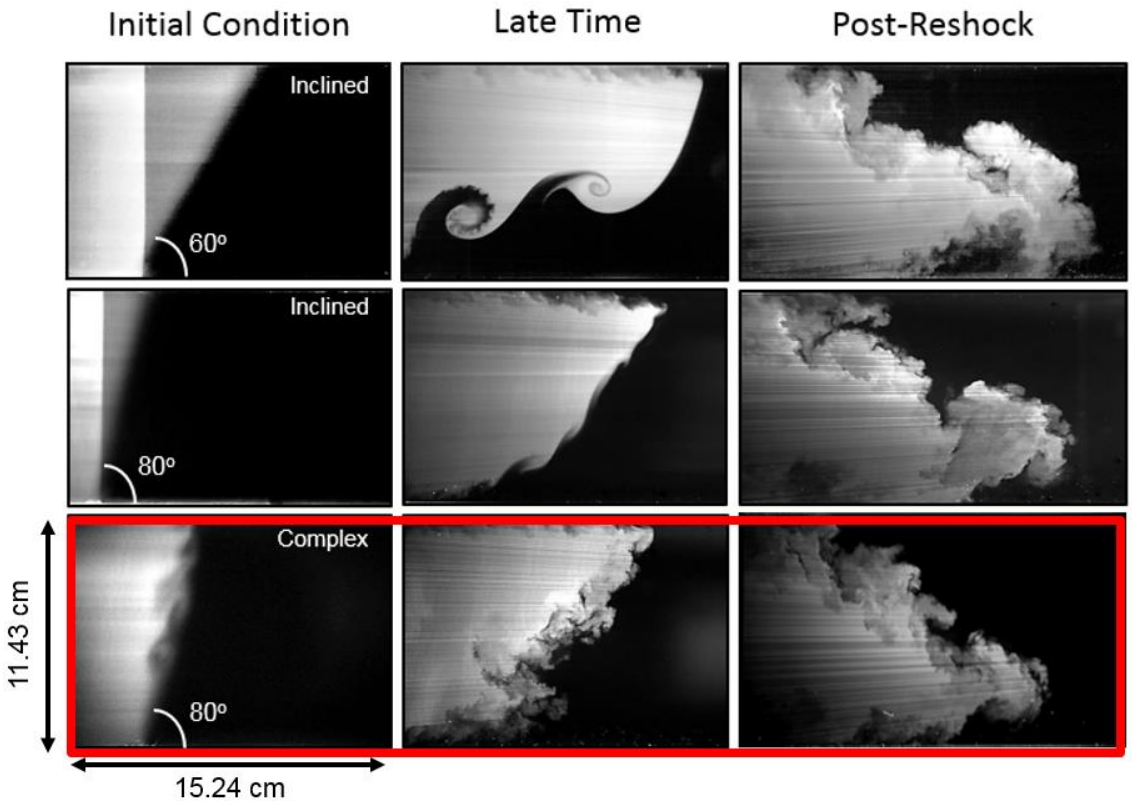

Figure 60: PLIF image set presenting the effect of angle and modal content on interface evolution before and after reshock.

4.3.3 Quantitative Results

Next quantitative results will be presented based on the velocity and concentration fields which were collected simultaneously. A discussion of how the data can be used to inform a variable-density turbulence model from LANL will also be included.

Vorticity Deposition After Incident shock

Figure 61 shows the vorticity fields for the inclined and complex interfaces for the initial condition as well as at late time. The inclined interface features two pockets of vorticity (positive and negative) with no overlap initially. This vorticity is very weak, however, and the majority of vorticity deposited by the incident shock is negative. In contrast, the complex interface has two strips of vorticity which reach across the span of the shock tube. This is caused by the counter-flowing jets. Because there is a complex density field which interacts with the incident shock, there is both positive and negative vorticity deposited. The vorticity present at the initial condition does not strongly affect the post-shock vorticity distribution. Rather, the initial vorticity distribution affects the density gradients, which will affect the vorticity deposition.

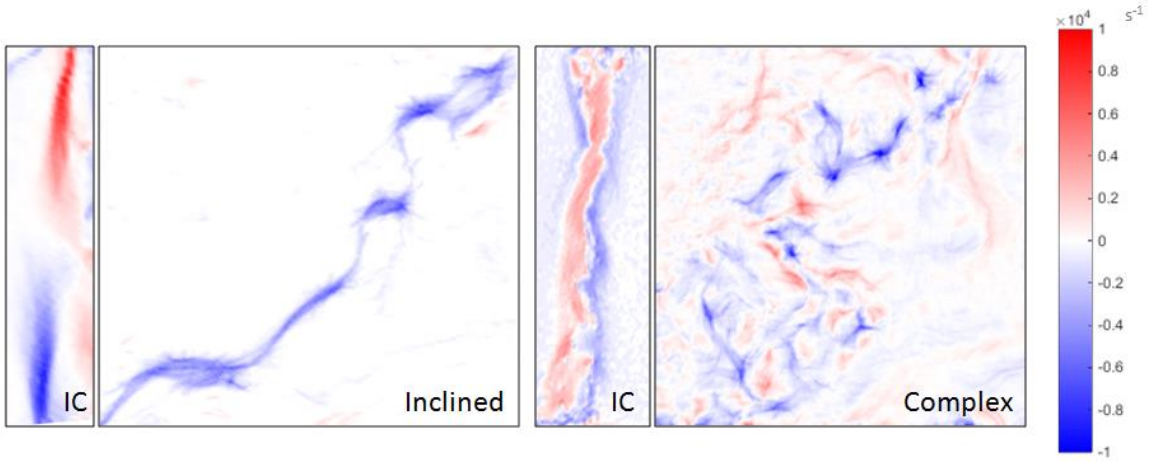

Figure 61: Vorticity fields for the inclined and complex interfaces post incident shock (~4.75 ms) with representative initial conditions. Initial condition vorticity plots use a different scales for better visibility. Experimental conditions: N_2/CO_2, M-1.55, θ-80°.

One way to quantify the differences in vorticity distribution seen in Figure 61 is to plot a histogram of the vorticity (Figure 62). The inclined case has a much longer tail which captures the large amount of negative vorticity deposited. This results in a larger

skewness. The complex case has a lower skewness due to the more even deposition of positive and negative vorticity. There is a large peak near zero because the entire field was included when calculating the histogram (much of the field has near zero vorticity).

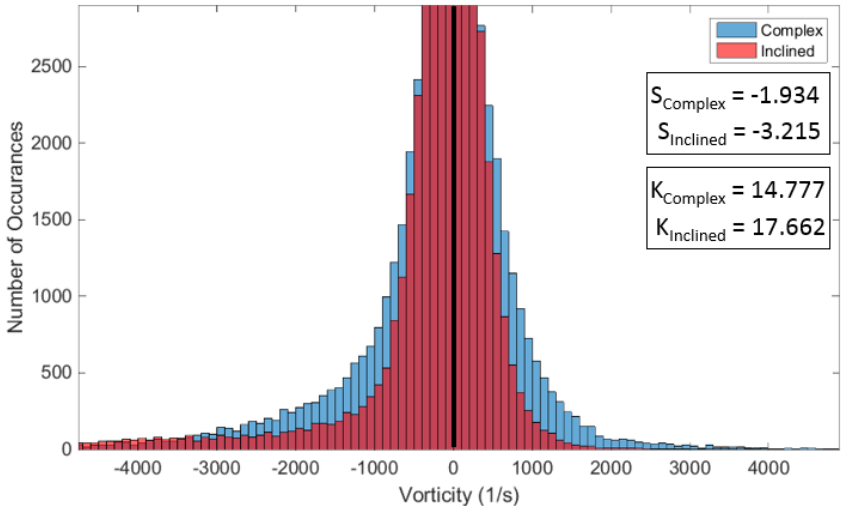

Figure 62: Histograms of vorticity for inclined and complex interfaces at late time (~4.75ms). Skewness (*S*) and kurtosis (*K*) are labeled.

Another way to understand the distribution of vorticity is by averaging the vorticity in the spanwise direction and plotting this versus streamwise distance (Figure 63). The spanwise average of vorticity tends to be quite low (< 1000 1/s) because there are many values near zero which factor into the average. The inclined case shows a steady trend of negative vorticity over much of the mixing width with spikes at the vortex structures. In contrast, the complex case shows many peaks which rise into the positive range of vorticity. This reflects the pockets of positive and negative vorticity seen in Figure 61. The pockets of negative vorticity dominate the positive, and this is seen in Figure 63 as the blue line remains below zero over the majority of the streamwise distance.

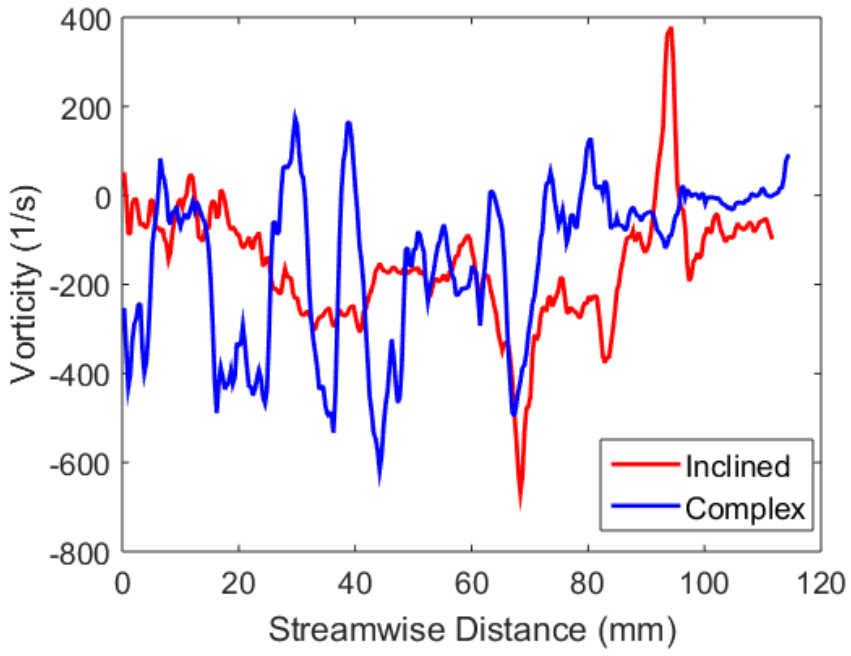

Figure 63: Spanwise average vorticity versus streamwise distance for inclined and complex cases before reshock (4.75 ms).

The circulation statistics are tabulated in Table 7 for both the inclined and complex cases. Although the total circulation is similar (6.5% different), there is significantly more of each positive and negative circulation in the complex case, 38% and 14%, respectively. The large increase in positive circulation deposition is expected given the complex initial condition which creates a large variety of density gradients in many directions for the incident shock to interact with. However, since the complex interface still has the underlying inclined interface perturbation, the negative component of circulation still dominates.

Table 7: Circulation statistics for inclined and complex interface at late time (~4.75ms).

Case	Number of experiments	Component	Ensemble average circulation (m^2/s)	Standard deviation (m^2/s)	Coefficient of variance (%)
Inclined	5	Positive	1.062	0.057	5.3
		Negative	-2.659	0.101	3.8
		Total	-1.598	0.112	7.0
Complex	20	Positive	1.553	0.119	7.6
		Negative	-3.052	0.135	4.4
		Total	-1.498	0.101	6.8

Post-Incident Shock Turbulence Statistics

Turbulence statistics were collected after the incident shock at late time, just before reshock occurs. Reynolds stress or turbulent stress is a component of the total stress tensor in a fluid after averaging the Naiver-Stokes equations. The turbulent stresses in both the spanwise and streamwise directions are plotted in Figure 64. The streamwise component for the inclined case is stronger than its spanwise counterpart by approximately four times, indicating that there is still some anisotropy in the direction of the shock. The complex case shows a similar streamwise component, but with a stronger spanwise component. Even so, there is still some anisotropy present. Near the center of the mixing width, the r.m.s. value of the streamwise velocity fluctuation reaches approximately 3% of the bulk fluid velocity. These fluctuations should rise above the noise level since the PIV uncertainty measurements have shown the PPR uncertainty to be 0.7% or less. The cross-correlation ($\overline{u'v'}$) is also plotted for both cases and is related to the generalized Reynolds shear stress. In both cases, the streamwise and spanwise components are negatively correlated.

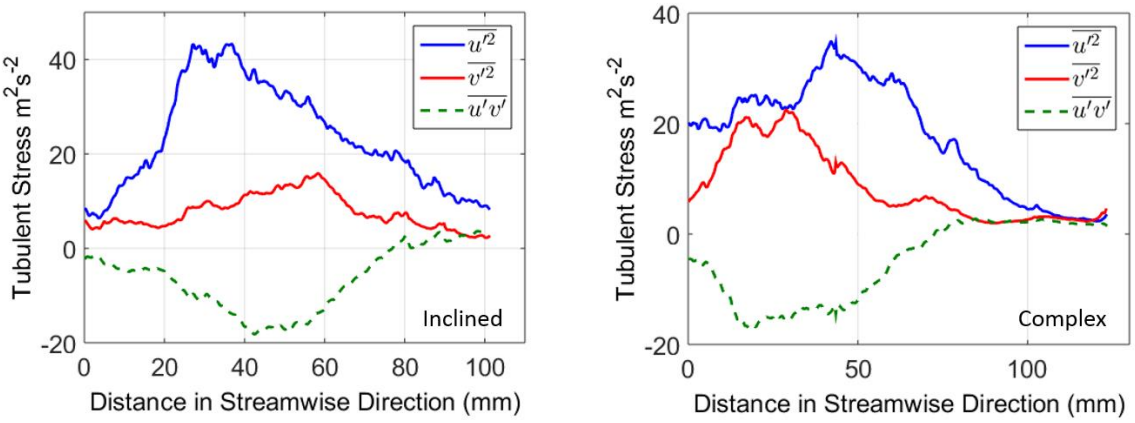

Figure 64: Turbulent stresses for inclined and complex interface at late time (4.75ms).

The 2D turbulent kinetic energy was also calculated for the two cases using the method described previously (Figure 65). The streamwise and spanwise components are plotted separately. In each case, the streamwise component is more energetic, which can also be seen from the velocity variances (Figure 64). However, the separation in energy between the two components is slightly less for the complex case. Both cases appear to be developing an inertial range, although the complex case follows $k^{-5/3}$ more closely for a longer range of wavenumbers. There is still debate within the RM/RT community regarding what slope the inertial range should follow. The inertial range is observed over approximately one and a half decades of wavenumbers. At the highest wavenumbers, a steep decline in energy is observed due to a combination of resolution and moderate Gaussian filtering performed during vector processing. Although it looks similar to a dissipation range, this range is not captured in these experiments. Good repeatability is observed between runs in the ensemble data set as shown in Figure 66.

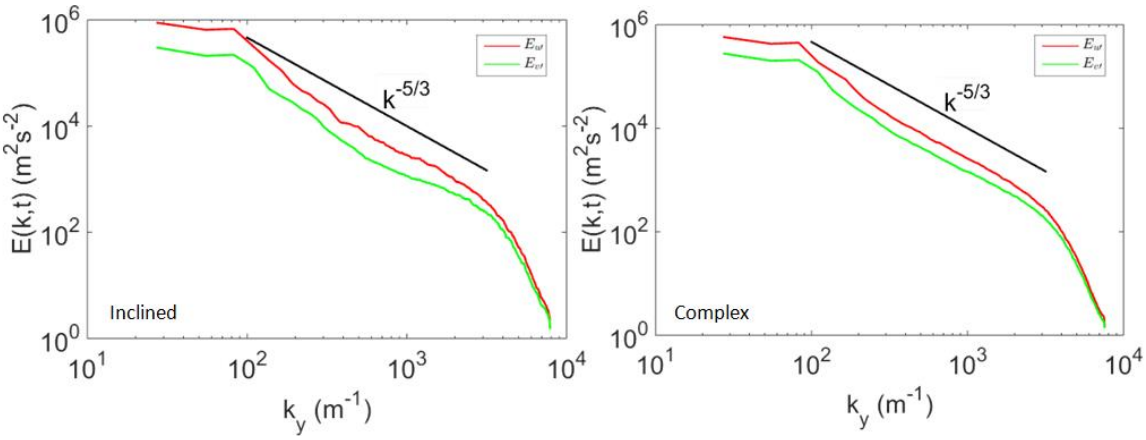

Figure 65: 2D TKE for inclined and complex interfaces at late time (4.75ms) with $k^{-5/3}$ fiducial. Ensemble averaged using 5 and 20 experimental runs for the inclined and complex cases, respectively.

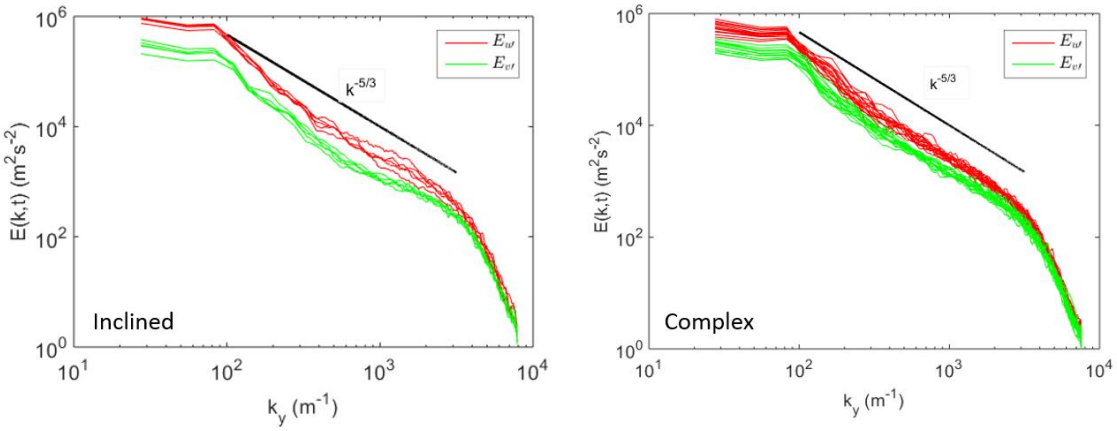

Figure 66: Ensemble sets of 2D TKE (streamwise component) for inclined and complex interfaces at late time (4.75ms) with $k^{-5/3}$ fiducial.

Scalar Mixing Statistics

The mole fraction fields for the inclined and complex cases are presented in Figure 67. The mole fraction varies from one (pure nitrogen seeded with acetone) to zero (pure carbon dioxide). At the initial time, the complex interface has more long wavelength, small amplitude modal components than the inclined interface. The complex

interface also has visible more mixing at late time, although the two cases look similar after reshock.

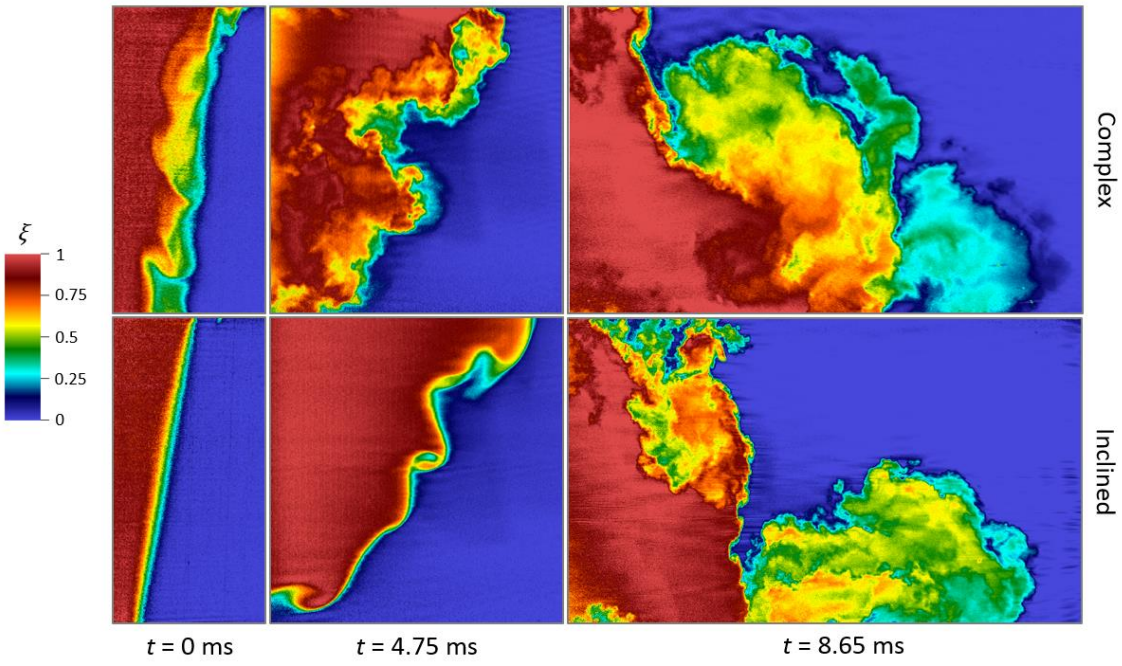

Figure 67: Mole fraction fields for the inclined and complex cases at three times. The first time is before incident shock; the second is after incident shock; and the last is after reshock.

Next, scalar mixing statistics will be presented. There are several quantities which are useful in describing scalar mixing. The most coarse way of approximating the extent of mixing is through the mixing width or integral mix width (Equation 24). The amount of molecular mixing which occurs is described by the mixedness

Equation 26

$$\theta = \frac{\int_{-\infty}^{\infty} \langle Y_{N_2} Y_{CO_2} \rangle dx}{\int_{-\infty}^{\infty} \langle Y_{N_2} \rangle \langle Y_{CO_2} \rangle dx}$$

where Y denotes a mass fraction and $\langle \cdot \rangle$ denotes a spanwise average. Mixedness is unity for a fully homogenous flow field and goes to zero as the field departs from this fully mixed state. It is the ratio of mixed fluid to entrained fluid. Mixedness approaches 0.8 for

fully developed three-dimensional mixing [84]. Another parameter which can be used to describe small-scale mixing is mixed mass per unit depth

Equation 27

$$m = \int \rho dA$$

where ρ is density between the 5% and 95% bounds of the density range and A is area. If three-dimensional density data were available, then a volume integral would be used in place of the area integral. The densities which are used to convert the concentration field to a density field are calculated using one-dimensional gas dynamics.

Table 8 contains the ensemble mixing statistics for the inclined and complex cases before and after reshock. The inclined case experiences a large increase in mixedness after reshock; however, the complex case has a high mixedness before reshock and remains nearly unchanged after reshock. The complex case has more mixed mass and slightly a slightly larger mixing width for both times.

Table 8: Ensemble averaged mixedness, mixed mass, and integral mix width for the inclined and complex cases before (4.75 ms) and after (8.65 ms) reshock (RS). Ensemble averages are from five experiments.

	Inclined		Complex	
	Before RS	After RS	Before RS	After RS
Mixedness	0.50	0.79	0.72	0.69
Mixed Mass (g/cm)	0.13	0.51	0.19	0.55
Integral Mix Width (cm)	3.99	8.95	5.32	9.28
Mix Width (cm)	5.28	10.54	6.76	12.57

The range of scales over which mixing is occurring is characterized by investigating the Power Spectral Density (PSD) of the density field. Figure 68 shows the PSD of the inclined and complex cases before and after reshock. The ensemble averages

are shown in Figure 69. Good repeatability is observed with much of the variation occurring at high wavenumbers. Both cases appear to develop an inertial range for at least one decade before reshock. There is a steep decline from the initial large wavelength. Aliasing effects are observed at high wavenumbers; these effects are less prominent after reshock. An amplification in the PSD is expected due to the large increase in density after reshock and was observed in both cases. The complex case has more energy than the inclined case at high wavenumbers before and after reshock.

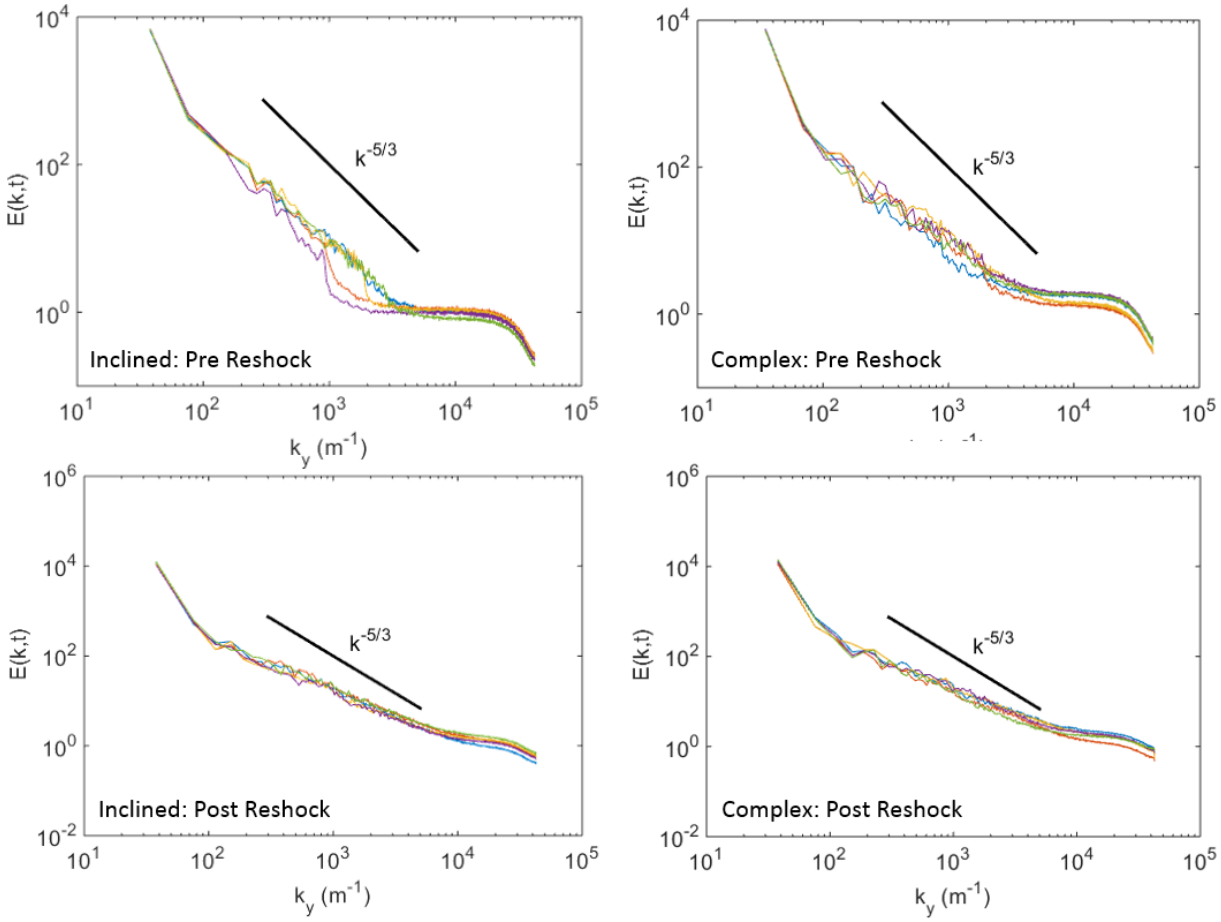

Figure 68: Power Spectral Density (PSD) for the inclined and complex cases before and after reshock. $k^{-5/3}$ fiducial included for reference.

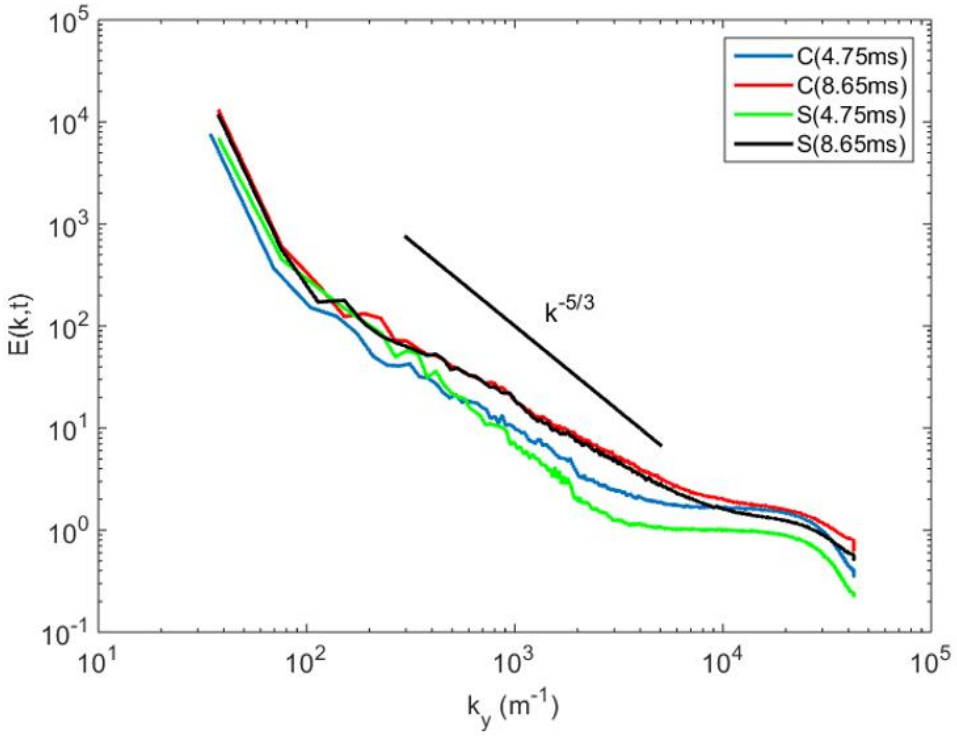

Figure 69: Ensemble average PSD for each of the complex (C) and simple (S) inclined cases.

Variable-Density Turbulence Model

Turbulent mixing which is induced by shock-driven or buoyancy-driven hydrodynamic instabilities have several defining characteristics that separate them from classical turbulent flows. This makes modeling such flows difficult. Some of the characteristics include anisotropy from the source of acceleration and boundary conditions, and also baroclinic effects and vorticity production at material interfaces [1]. Traditional turbulence models struggle with initializing turbulence field variables in these types of flows, and this is considered a serious problem.

Work was done at Los Alamos National Laboratory (LANL) in 1992 to develop a variable-density turbulence model which handles multicomponent systems to be implemented into their numerical codes [51]. Applications include RT, KH, and RM

mixing problems. The model accounts for mixing and Fick's Law diffusion but not demixing. The model is called BHR after the authors' last names: Didier **B**esnard; Francis **H**arlow; Rick **R**auenzahn; and Charles Zemach. (It is unknown to the current author why Charles Zemach was not included when naming the model.) It is an extension of the traditional $k-\epsilon$ model. The equations define both a length scale (S) as well as the density-velocity correlation (a)

Equations 28

$$S = \frac{k^{3/2}}{\epsilon}$$

$$a = \frac{\overline{\rho' u'}}{\bar{\rho}}$$

where k is turbulent kinetic energy, ϵ is turbulent dissipation, ρ is density, and u is velocity. These quantities are solved for separately from mass, momentum, and k conservation equations.

Two of the most important parameters to tune the model coefficients are a and b. The density self-correlation (also called the density-specific volume correlation), b, is defined as

Equation 29

$$b = -\overline{\rho' \left(\frac{1}{\rho}\right)'}$$

This quantity appears in the source term in the a equation as well as in other second-moment turbulence model equations. The transport equation for the density self-correlation is

Equation 30

$$\underbrace{\frac{\partial b}{\partial t}}_{\text{Rate of change of } b} + \underbrace{(\bar{\boldsymbol{u}}\cdot\nabla)b}_{\text{Convective Transport}} + \underbrace{\frac{b+1}{\bar{\rho}}\nabla\cdot\bar{\rho}\boldsymbol{a}}_{\text{Production}} + \underbrace{\bar{\rho}\nabla\cdot\left(\overline{\left(\frac{1}{\rho}\right)'\boldsymbol{u}'}\right)}_{\text{Transport}} - \underbrace{2\bar{\rho}\overline{\left(\frac{1}{\rho}\right)'\nabla\cdot\boldsymbol{u}'}}_{\text{Allows for decay of } b} = 0$$

For a fully homogeneous flow field, b will be zero (molecular mixing parameter will be one), and will depart from zero for a non-mixed field. It has no upper bound although the molecular mixing equivalent would be zero. The exact value of what b should be is not well understood and needs to be studied using experiments. The experiments should ideally involve either RT, KH, or RM instabilities and variable-density turbulence. The current work is ideal for tweaking this model since the experiments involve both RMI and KHI and are variable-density, tending towards an inertial range suggestive of a turbulent state.

Figure 70 shows the density-self correlation for the inclined and complex cases before and after reshock. Instantaneous realizations show significant differences compared to the ensemble averages shown in Figure 71. The greatest variability occurs near the extents where b approaches zero. A higher density self-correlation is observed for the inclined case compared to the complex case before reshock as expected. The inclined case also experiences a decrease in b after reshock because of the increase in mixing. However, the complex case actually sees an increase in b after reshock because of the spike penetrating into the bubble. The density self-correlation is sensitive to small experimental variation. If the small spike in b for the complex case is overlooked, both cases have similar magnitudes after reshock. Furthermore, the distribution in b spreads after reshock, which was also observed by Balakumar et al. [85].

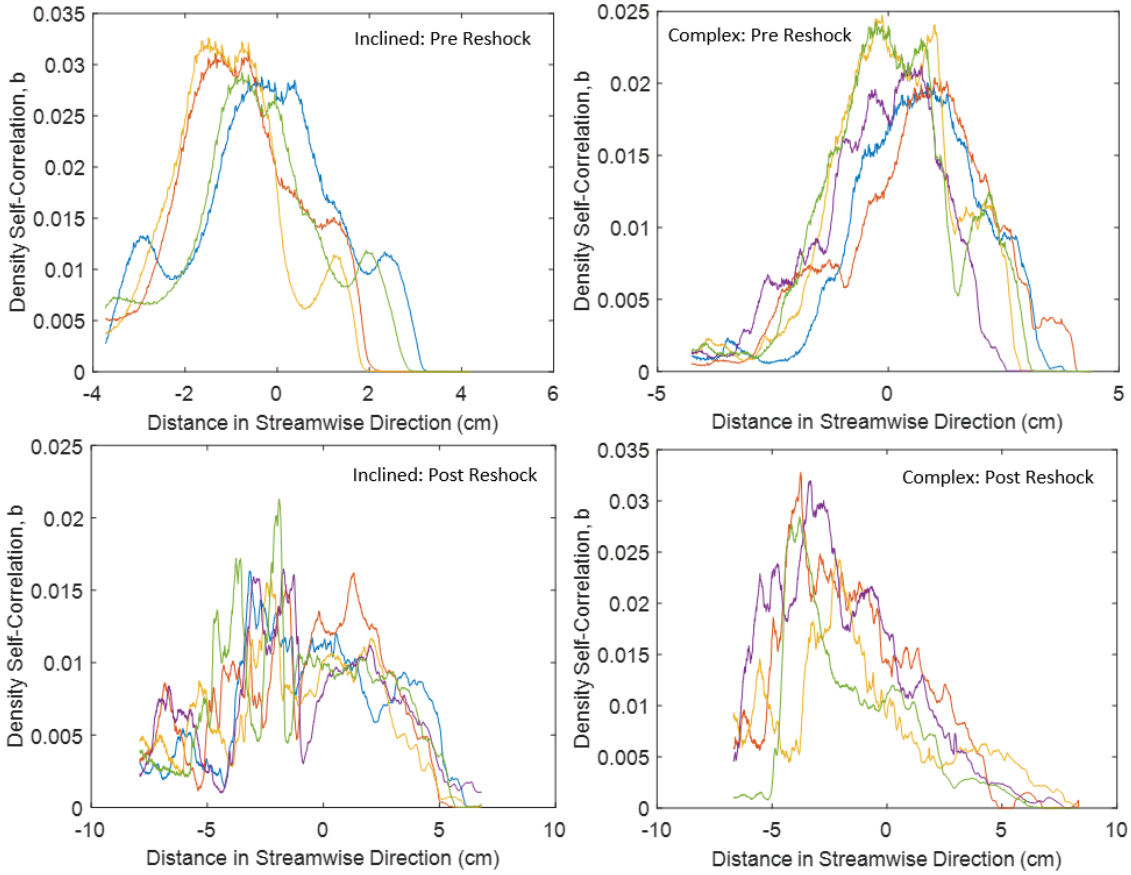

Figure 70: Density self-correlation for the inclined and complex cases before and after reshock.

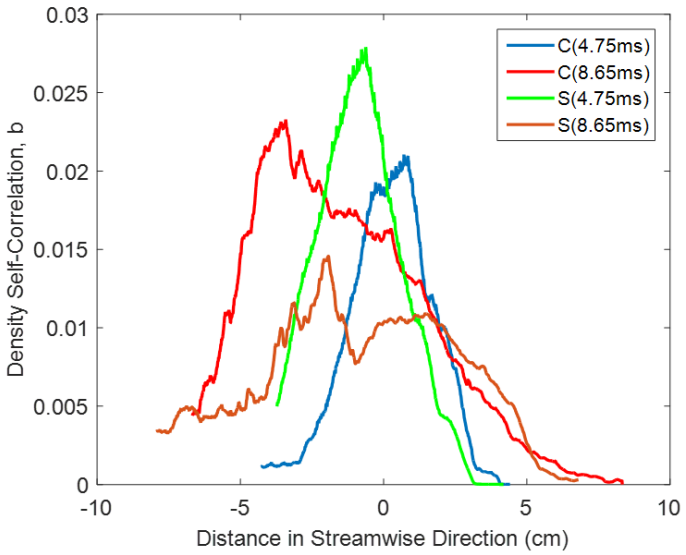

Figure 71: Ensemble average density self-correlation for complex (C) and simple (S) inclined cases before and after reshock.

CHAPTER 5: Conclusions and Future Work

5.1 Reshock Study Conclusions

From the Mie scattering image time series for Cases 1, 2, and 3, it can be determined that a more developed pre-reshock interface results in a more mixed post-reshock interface. Although the mixing width decreases after reshock, the interface length continues to increase because the reshock wave amplifies small-scale perturbations on the pre-reshock interface. Although the same amount of energy is deposited by the first shock for all three cases, there are different amounts of energy deposited by the second shock (reshock). The more developed the interface, the more energy is deposited by reshock due to the larger surface area with a density gradient, which provides a larger $\nabla\rho \times \nabla P$. The most developed interface also receives more vorticity deposition. After reshock, the sign of the vorticity near the interface changes because of the additional baroclinic torque applied by the reshock wave. Velocity statistics show that the cross-correlation ($\overline{u'v'}$) is negative over much of the mixing layer, which means that there is shear and anisotropy present. All three cases begin to develop an inertial range after reshock, but only Case 3 begins to develop this range before reshock. Case 3's vorticity is better distributed compared to the other two cases, which is why it develops an inertial range faster and follows a $k^{-5/3}$ power law longer.

5.2 Parametric Study Conclusions

The parametric study, which included both linear and nonlinear initial conditions, provided for validation of a scaling technique as well as for comparison to Ares simulations. The nonlinear 60^o case and the linear 80^o case showed considerable differences in development prior to reshock; however, after reshock their mixing widths converged. This finding suggests that reshock erases the memory of nonlinearity. Other experimentalists in this field have also found this to be true with other initial conditions. These two cases are the first to show precise control of the baroclinic term in the vorticity equation which is a unique capability of the inclined shock tube facility. The theoretical prediction of circulation increase with decreasing angle compared well with the experimental findings. Increasing the Mach number left the mixing width nearly unchanged but should have increased the circulation deposition , which will be studied with PIV in the future. Increasing the Atwood number resulted in much greater interface stretching which also tended to damp small-scale perturbations. Inclined interface scaling was able to collapse the data before reshock.

5.3 Complex Interface Study Conclusions

In summary, a new perturbation technique was created which imposed large-wavelength, small-amplitude perturbation on the underlying inclined interface perturbation. Statistical measures show some level of repeatability. The initial condition characterization with POD suggests that only the first 50 modes are required for accurate interface reconstruction. PIV measurements revealed a very different vorticity distribution for the complex case compared to the inclined case. Although the complex case had more positive circulation deposition, negative circulation still dominated. This is because of the underlying inclined interface perturbation. The complex case also developed a larger inertial range as seen in the TKE spectrum. This suggests that the complex case is approaching homogenous, isotropic turbulent environment. Streamwise and spanwise Reynolds stress components were closer in magnitude for the complex case, which indicates the flow is becoming less anisotropic. The complex case exhibited greater mixing as quantified with mixed mass and mixedness. Large-scale flow structures allowed the complex case to have a higher peak in the density self-correlation after reshock. The density self-correlation profiles will be useful for initializing variable-density turbulence codes which can be used to simulate the hydrodynamics found in ICF and begin to answer the question if the RMI is partly responsible for limiting energy output.

5.4 Future Work

Further developments are still needed to improve simultaneous PLIF/PIV results. Solid particles will be explored as they are expected to yield better results after reshock, especially for higher Mach numbers which create higher temperatures that can evaporate oil particles. Stereo PIV will be implemented to gain the third component of velocity. This also will be more important after reshock when the flow exhibits greater three dimensionality. The PIV particles can also be replaced with thermographic particles to gain information about velocity and temperature simultaneously. If this were combined with the PLIF diagnostic, then quantitative PLIF/PIV would be possible even for high Mach numbers.

Other initial conditions will also be investigated. It would be beneficial to create fully turbulent initial conditions so that shocked turbulence could be studied. Then turbulence statistics could be collected and monitored after the shock interaction. This information, combined with the complex interface study in this work, would provide insights into initial condition dependence in RM unstable flows.

An improved laser window for the test section should also be developed to allow for scanning of the interface in the third dimension. This is especially important for initial conditions which have more modal content in the third dimension, such as the complex interface. In order to scan an interface which is not static, a higher repetition rate laser will most likely be required. The repetition rate required can be determined by first estimating the residence time of dominant structures seen in the initial condition perturbation.

APPENDIX A: LABVIEW PROGRAMS

Several additions were made to existing LabVIEW programs which are used to operate the inclined shock tube facility. Figure 72 shows the front panel of the shock tube control "vi," which stands for "virtual instrument." Parts of the program which have been updated are outlined in a red box. Starting in the upper right-hand corner, there are three lines for controlling MKS mass flow controllers. It allows the user to enter a set point and continuously monitor the actual flow rate. The code for this is shown in Figure 74. Also on the right-hand side of Figure 72 is a graph used to display the voltage of a photodiode which can be connected to the fog mixing tank. The photodiode readout has been used to monitor the fog seeding density. In the center of Figure 72 is a control for the boost tank pressure. For a given Mach number, the pressure of the boost tank should be the same for each experiment. This allows the user to enter a boost tank pressure, and a feedback loop in LabVIEW will control a solenoid valve which will in turn control the pressure in the boost tank. The code for this control is displayed in Figure 73. The last update in Figure 72 is a driver relief valve. This controls an electrically-actuated ball valve mounted on the top of the driver. This can be used to vent the driver if it is pressurized but the user does not desire to fire a shock. One last change was made to a different tab of the shock tube control vi which allows for the oscillation of the interface valves (Figure 75). Oscillating the valves has been investigated as a technique to create a multimodal initial condition and may be of use to future experimentalists.

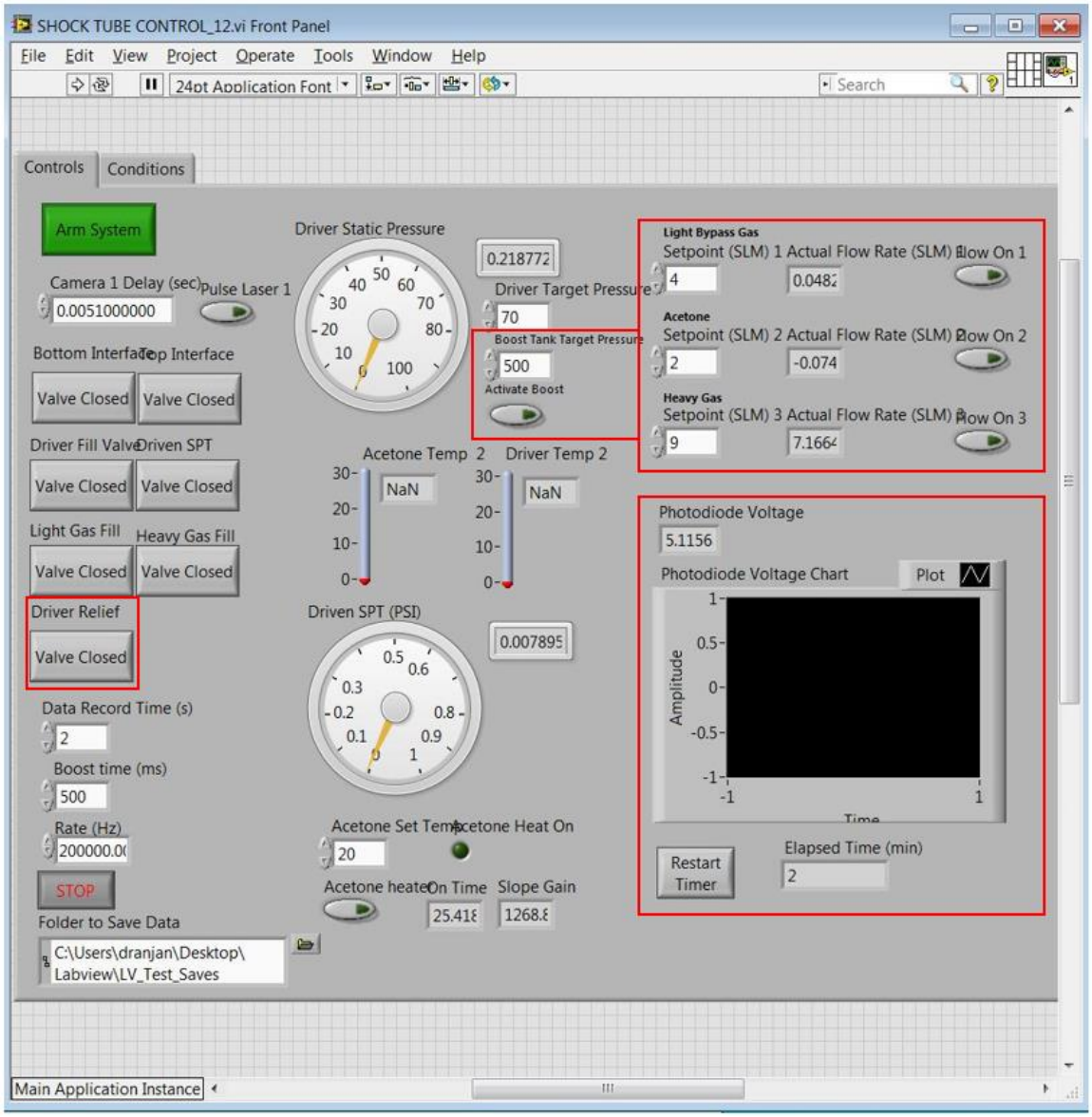

Figure 72: LabVIEW program front panel for controlling the shock tube. Updated parts of the program are outlined in red.

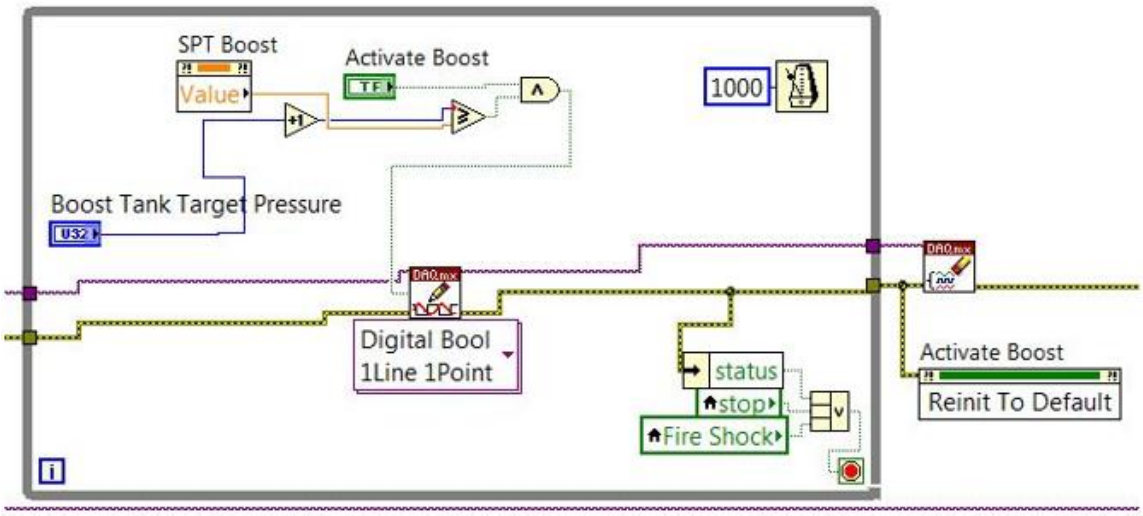

Figure 73: LabVIEW code for controlling the pressure of the boost valve.

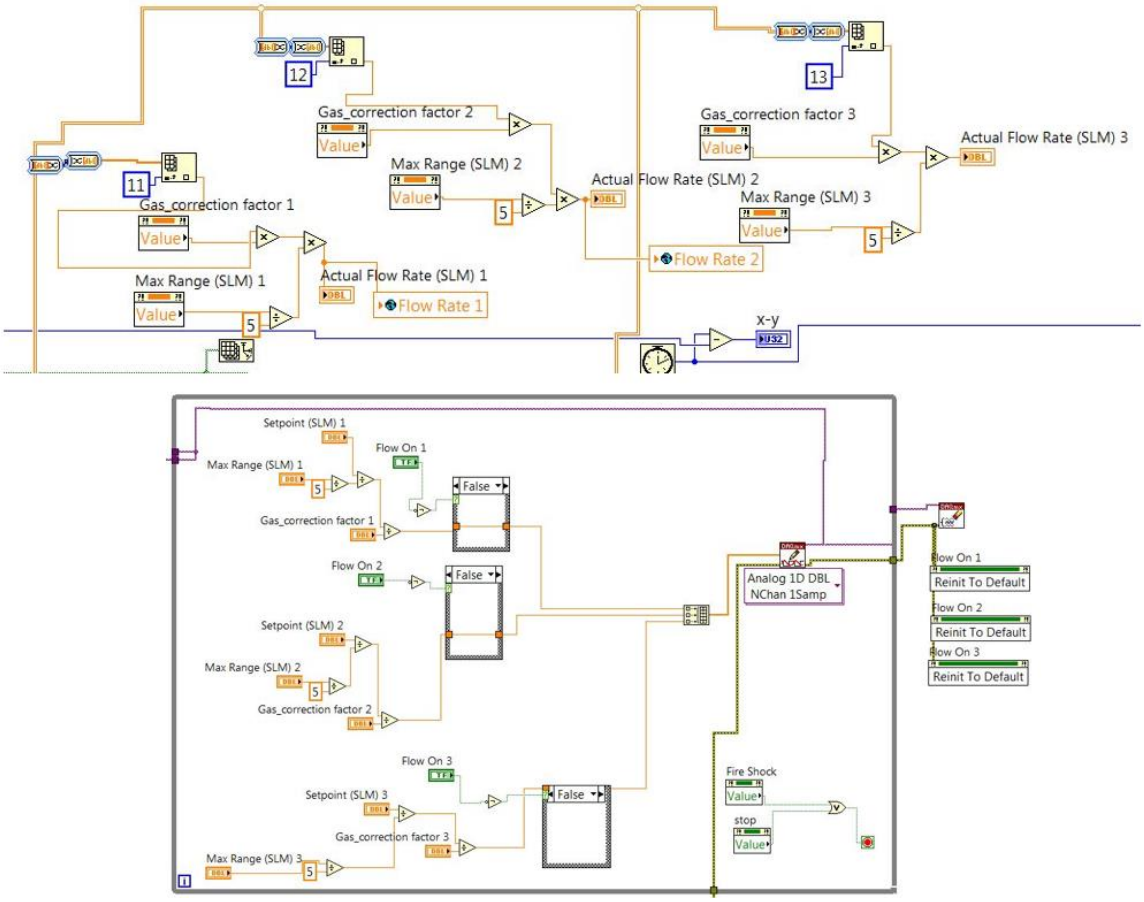

Figure 74: LabVIEW code for setting and controlling the MKS mass flow controllers.

Figure 75: LabVIEW front panel and code for oscillating the valves. This was one of the first techniques tried to perturb the interface.

REFERENCES

[1] A. Banerjee and M. J. Andrews, "3D simulations to investigate initial condition effects on the growth of Rayleigh–Taylor mixing," *International Journal of Heat and Mass Transfer*, vol. 52, pp. 3906-3917, 2009.

[2] B. Hammel, T. Bernat, G. Collins, S. Haan, O. Landen, B. MacGowan, *et al.*, "Recent advances in indirect drive ICF target physics at LLNL," in *Proc 17th Int. Conf. Yokohama*, 1998.

[3] J. A. Paisner, J. D. Boyes, S. A. Kumpan, W. H. Lowdermilk, and M. S. Sorem, "Conceptual design of the national ignition facility," in *Solid State Lasers for Application to Inertial Confinement Fusion (ICF)*, 1995, pp. 2-12.

[4] S. D. V. Dyk, "What are Supernovae?," 2014.

[5] K. Schawinski, S. Justham, C. Wolf, P. Podsiadlowski, M. Sullivan, K. C. Steenbrugge, *et al.*, "Supernova shock breakout from a red supergiant," *Science*, vol. 321, pp. 223-226, 2008.

[6] M. Marimon Mateu, "Study of an air-breathing engine for hypersonic flight," 2013.

[7] R. F. Benjamin, "Rayleigh-Taylor instability–fascinating gateway to the study of fluid dynamics," *The Physics Teacher*, vol. 37, pp. 332-336, 1999.

[8] G. Jagadeesh, G. D. Prakash, S. Rakesh, U. S. Allam, M. G. Krishna, S. M. Eswarappa, *et al.*, "Needleless vaccine delivery using micro-shock waves," *Clinical and Vaccine Immunology*, vol. 18, pp. 539-545, 2011.

[9] M. Delius, F. Ueberle, and W. Eisenmenger, "Extracorporeal shock waves act by shock wave-gas bubble interaction," *Ultrasound in medicine & biology*, vol. 24, pp. 1055-1059, 1998.

[10] W. Eisenmenger, "The mechanisms of stone fragmentation in ESWL," *Ultrasound in medicine & biology*, vol. 27, pp. 683-693, 2001.

[11] S. Gracewski, G. Dahake, Z. Ding, S. Burns, and E. C. Everbach, "Internal stress wave measurements in solids subjected to lithotripter pulses," *The Journal of the Acoustical Society of America*, vol. 94, pp. 652-661, 1993.

[12] S. O. Glossary, "Schlumberger," *Retrieved from the internet< URL: http://glossary. connect. slb. com> Terms: Electrical Stability Test, Electrical Resitivity, Invert Emulsion*, 2010.

[13] M. B. Prime, W. T. Buttler, S. K. Sjue, B. J. Jensen, F. G. Mariam, D. M. Oró, *et al.*, "Using Richtmyer–Meshkov Instabilities to Estimate Metal Strength at Very High Rates," in *Dynamic Behavior of Materials, Volume 1*, ed: Springer, 2016, pp. 191-197.

[14] R. D. Richtmyer, "Taylor instability in shock acceleration of compressible fluids," *Communications on Pure and Applied Mathematics*, vol. 13, pp. 297-319, 1960.

[15] E. Meshkov, "Instability of the interface of two gases accelerated by a shock wave," *Fluid Dynamics*, vol. 4, pp. 101-104, 1969.

[16] W. Thomson, "XLVI. Hydrokinetic solutions and observations," *The London, Edinburgh, and Dublin Philosophical Magazine and Journal of Science*, vol. 42, pp. 362-377, 1871.

[17] A. Oberbeck, "Ueber discontinuirliche Flüssigkeitsbewegungen," *Annalen der Physik*, vol. 238, pp. 1-16, 1877.
[18] J. Strutt and L. Rayleigh, "Investigation of the character of the equilibrium of an incompressible heavy fluid of variable density," *Proc. London Math. Soc*, vol. 14, p. 8, 1883.
[19] G. Taylor, "The instability of liquid surfaces when accelerated in a direction perpendicular to their planes. I," in *Proceedings of the Royal Society of London A: Mathematical, Physical and Engineering Sciences*, 1950, pp. 192-196.
[20] R. W. Fox, A. T. McDonald, and P. J. Pritchard, *Introduction to fluid mechanics* vol. 7: John Wiley & Sons New York, 1985.
[21] R. G. Jahn, "The refraction of shock waves at a gaseous interface," *Journal of Fluid Mechanics*, vol. 1, pp. 457-489, 1956.
[22] M. Anderson, B. Puranik, J. Oakley, P. Brooks, and R. Bonazza, "Shock tube investigation of hydrodynamic issues related to inertial confinement fusion," *Shock Waves*, vol. 10, pp. 377-387, 2000.
[23] B. Blue, S. Weber, S. Glendinning, N. Lanier, D. Woods, M. Bono, *et al.*, "Experimental investigation of high-Mach-number 3D hydrodynamic jets at the National Ignition Facility," *Physical review letters*, vol. 94, p. 095005, 2005.
[24] C. Kuranz, R. Drake, E. Harding, M. Grosskopf, H. Robey, B. Remington, *et al.*, "Two-dimensional blast-wave-driven Rayleigh-Taylor instability: experiment and simulation," *The Astrophysical Journal*, vol. 696, p. 749, 2009.
[25] E. Harding, J. Hansen, O. Hurricane, R. Drake, H. Robey, C. Kuranz, *et al.*, "Observation of a kelvin-helmholtz instability in a high-energy-density plasma on the omega laser," *Physical review letters*, vol. 103, p. 045005, 2009.
[26] P. Chapman and J. Jacobs, "Experiments on the three-dimensional incompressible Richtmyer-Meshkov instability," *Physics of Fluids (1994-present)*, vol. 18, p. 074101, 2006.
[27] C. Niederhaus and J. W. Jacobs, "Experimental study of the Richtmyer–Meshkov instability of incompressible fluids," *Journal of Fluid Mechanics*, vol. 485, pp. 243-277, 2003.
[28] K. Read, "Experimental investigation of turbulent mixing by Rayleigh-Taylor instability," *Physica D: Nonlinear Phenomena*, vol. 12, pp. 45-58, 1984.
[29] G. Dimonte and M. Schneider, "Turbulent Rayleigh-Taylor instability experiments with variable acceleration," *Physical Review E*, vol. 54, p. 3740, 1996.
[30] N. Yamashita and J. Jacobs, "The Experimental Study of Rayleigh-Taylor Instability using a Linear Induction Motor Accelerator," in *APS Division of Fluid Dynamics Meeting Abstracts*, 2009.
[31] M. Vetter and B. Sturtevant, "Experiments on the Richtmyer-Meshkov instability of an air/SF6 interface," *Shock Waves*, vol. 4, pp. 247-252, 1995.
[32] L. Erez, O. Sadot, D. Oron, G. Erez, L. Levin, D. Shvarts, *et al.*, "Study of the membrane effect on turbulent mixing measurements in shock tubes," *Shock Waves*, vol. 10, pp. 241-251, 2000.
[33] L. Houas and I. Chemouni, "Experimental investigation of Richtmyer–Meshkov instability in shock tube," *Physics of Fluids (1994-present)*, vol. 8, pp. 614-627, 1996.

[34] A. Aleshin, S. Zaitsev, and E. Lazareva, "Damping of perturbations at a shock front in the presence of a Richtmyer–Meshkov instability," *Sov. Tech. Phys. Lett,* vol. 17, pp. 493-496, 1991.

[35] D. Holder and C. Barton, "Shock tube Richtmyer-Meshkov experiments: inverse chevron and half height," *Proceedings of the Ninth IWPCTM,* 2004.

[36] J. H. Niederhaus, J. Greenough, J. Oakley, D. Ranjan, M. Anderson, and R. Bonazza, "A computational parameter study for the three-dimensional shock–bubble interaction," *Journal of Fluid Mechanics,* vol. 594, pp. 85-124, 2008.

[37] J. Niederhaus, D. Ranjan, J. Oakley, M. Anderson, J. Greenough, and R. Bonazza, "Computations in 3D for shock-induced distortion of a light spherical gas inhomogeneity," in *Shock Waves,* ed: Springer, 2009, pp. 1169-1174.

[38] N. Haehn, C. Weber, J. Oakley, M. Anderson, D. Ranjan, and R. Bonazza, "Experimental investigation of a twice-shocked spherical gas inhomogeneity with particle image velocimetry," *Shock Waves,* vol. 21, pp. 225-231, 2011.

[39] D. Ranjan, M. Anderson, J. Oakley, and R. Bonazza, "Experimental investigation of a strongly shocked gas bubble," *Physical review letters,* vol. 94, p. 184507, 2005.

[40] D. Ranjan, J. Niederhaus, B. Motl, M. Anderson, J. Oakley, and R. Bonazza, "Experimental investigation of primary and secondary features in high-Mach-number shock-bubble interaction," *Physical review letters,* vol. 98, p. 024502, 2007.

[41] D. Ranjan, J. Niederhaus, J. Oakley, M. Anderson, J. Greenough, and R. Bonazza, "Experimental and numerical investigation of shock-induced distortion of a spherical gas inhomogeneity," *Physica Scripta,* vol. 2008, p. 014020, 2008.

[42] S. Balasubramanian, G. Orlicz, K. Prestridge, and B. Balakumar, "Experimental study of initial condition dependence on Richtmyer-Meshkov instability in the presence of reshock," *Physics of Fluids (1994-present),* vol. 24, p. 034103, 2012.

[43] B. Balakumar, G. Orlicz, C. Tomkins, and K. Prestridge, "Simultaneous particle-image velocimetry–planar laser-induced fluorescence measurements of Richtmyer–Meshkov instability growth in a gas curtain with and without reshock," *Physics of Fluids (1994-present),* vol. 20, p. 124103, 2008.

[44] C. Tomkins, B. Balakumar, G. Orlicz, K. Prestridge, and J. Ristorcelli, "Evolution of the density self-correlation in developing Richtmyer–Meshkov turbulence," *Journal of Fluid Mechanics,* vol. 735, pp. 288-306, 2013.

[45] G. Orlicz, B. Balakumar, C. Tomkins, and K. Prestridge, "A Mach number study of the Richtmyer–Meshkov instability in a varicose, heavy-gas curtain," *Physics of Fluids (1994-present),* vol. 21, p. 064102, 2009.

[46] G. Orlicz, S. Balasubramanian, and K. Prestridge, "Incident shock Mach number effects on Richtmyer-Meshkov mixing in a heavy gas layer," *Physics of Fluids (1994-present),* vol. 25, p. 114101, 2013.

[47] K. Prestridge, P. Vorobieff, P. Rightley, and R. Benjamin, "Validation of an instability growth model using particle image velocimetry measurements," *Physical Review Letters,* vol. 84, p. 4353, 2000.

[48] C. Tomkins, K. Prestridge, P. Rightley, M. Marr-Lyon, P. Vorobieff, and R. Benjamin, "A quantitative study of the interaction of two Richtmyer-Meshkov-unstable gas cylinders," *Physics of Fluids,* vol. 15, pp. 986-1004, 2003.

[49] C. Tomkins, S. Kumar, G. Orlicz, and K. Prestridge, "An experimental investigation of mixing mechanisms in shock-accelerated flow," *Journal of Fluid Mechanics,* vol. 611, pp. 131-150, 2008.
[50] P. E. Dimotakis, "Turbulent mixing," *Annu. Rev. Fluid Mech.,* vol. 37, pp. 329-356, 2005.
[51] D. Besnard, F. Harlow, R. Rauenzahn, and C. Zemach, "Turbulence transport equations for variable-density turbulence and their relationship to two-field models," Los Alamos National Lab., NM (United States)1992.
[52] M. Jones and J. Jacobs, "A membraneless experiment for the study of Richtmyer–Meshkov instability of a shock-accelerated gas interface," *Physics of Fluids (1994-present),* vol. 9, pp. 3078-3085, 1997.
[53] R. Aure and J. W. Jacobs, "Particle image velocimetry study of the shock-induced single mode Richtmyer–Meshkov instability," *Shock Waves,* vol. 18, pp. 161-167, 2008.
[54] J. Jacobs, V. Krivets, V. Tsiklashvili, and O. Likhachev, "Experiments on the Richtmyer–Meshkov instability with an imposed, random initial perturbation," *Shock Waves,* vol. 23, pp. 407-413, 2013.
[55] R. V. Morgan, R. Aure, J. Stockero, J. Greenough, W. Cabot, O. Likhachev, *et al.,* "On the late-time growth of the two-dimensional Richtmyer–Meshkov instability in shock tube experiments," *Journal of Fluid Mechanics,* vol. 712, pp. 354-383, 2012.
[56] B. Motl, J. Oakley, D. Ranjan, C. Weber, M. Anderson, and R. Bonazza, "Experimental validation of a Richtmyer–Meshkov scaling law over large density ratio and shock strength ranges," *Physics of Fluids (1994-present),* vol. 21, p. 126102, 2009.
[57] P. Puranik, J. Oakley, M. Anderson, and R. Bonazza, "Experimental study of the Richtmyer-Meshkov instability induced by a Mach 3 shock wave," *Shock Waves,* vol. 13, pp. 413-429, 2004.
[58] C. Weber, N. Haehn, J. Oakley, D. Rothamer, and R. Bonazza, "Turbulent mixing measurements in the Richtmyer-Meshkov instability," *Physics of Fluids (1994-present),* vol. 24, p. 074105, 2012.
[59] C. R. Weber, N. S. Haehn, J. G. Oakley, D. A. Rothamer, and R. Bonazza, "An experimental investigation of the turbulent mixing transition in the Richtmyer–Meshkov instability," *Journal of Fluid Mechanics,* vol. 748, pp. 457-487, 2014.
[60] R. Mejia-Alvarez, B. Wilson, and K. Prestridge, "Simultaneous PIV/PLIF Measurements of Multi-mode Perturbed Initial Conditions of Single-Interface Richtmyer-Meshkov Mixing," in *29th International Symposium on Shock Waves 2*, 2015, pp. 1155-1160.
[61] G. Jourdan, L. Houas, L. Schwaederlé, G. Layes, R. Carrey, and F. Diaz, "A new variable inclination shock tube for multiple investigations," *Shock waves,* vol. 13, pp. 501-504, 2004.
[62] G. Layes, G. Jourdan, and L. Houas, "Experimental investigation of the shock wave interaction with a spherical gas inhomogeneity," *Physics of Fluids (1994-present),* vol. 17, p. 028103, 2005.

[63] D. Olmstead, C. Truman, P. Wayne, and P. Vorobieff, "Effects of inclination angle on a shock-accelerated heavy gas column," *Computational Methods in Multiphase Flow VIII,* vol. 89, p. 171, 2015.
[64] P. Wayne, D. Olmstead, P. Vorobieff, C. Truman, and S. Kumar, "Oblique shock interaction with a cylindrical density interface," *Computational Methods in Multiphase Flow VIII,* vol. 89, p. 161, 2015.
[65] J. McFarland, D. Reilly, S. Creel, C. McDonald, T. Finn, and D. Ranjan, "Experimental investigation of the inclined interface Richtmyer–Meshkov instability before and after reshock," *Experiments in fluids,* vol. 55, pp. 1-14, 2014.
[66] D. Reilly, J. McFarland, M. Mohaghar, and D. Ranjan, "The effects of initial conditions and circulation deposition on the inclined-interface reshocked Richtmyer–Meshkov instability," *Experiments in Fluids,* vol. 56, pp. 1-16, 2015.
[67] J. A. McFarland, J. A. Greenough, and D. Ranjan, "Computational parametric study of a Richtmyer-Meshkov instability for an inclined interface," *Physical Review E,* vol. 84, p. 026303, 2011.
[68] J. McFarland, J. Greenough, and D. Ranjan, "Investigation of the initial perturbation amplitude for the inclined interface Richtmyer–Meshkov instability," *Physica Scripta,* vol. 2013, p. 014014, 2013.
[69] J. A. McFarland, J. A. Greenough, and D. Ranjan, "Simulations and Analysis of the Reshocked Inclined Interface Richtmyer–Meshkov Instability for Linear and Nonlinear Interface Perturbations," *Journal of Fluids Engineering,* vol. 136, p. 071203, 2014.
[70] J. A. McFarland, D. Reilly, W. Black, J. A. Greenough, and D. Ranjan, "Modal interactions between a large-wavelength inclined interface and small-wavelength multimode perturbations in a Richtmyer-Meshkov instability," *Physical Review E,* vol. 92, p. 013023, 2015.
[71] B. J. Olson and J. Greenough, "Large eddy simulation requirements for the Richtmyer-Meshkov instability," *Physics of Fluids (1994-present),* vol. 26, p. 044103, 2014.
[72] O. Schilling and M. Latini, "High-order WENO simulations of three-dimensional reshocked Richtmyer–Meshkov instability to late times: dynamics, dependence on initial conditions, and comparisons to experimental data," *Acta Mathematica Scientia,* vol. 30, pp. 595-620, 2010.
[73] M. Hahn, D. Drikakis, D. Youngs, and R. Williams, "Richtmyer–Meshkov turbulent mixing arising from an inclined material interface with realistic surface perturbations and reshocked flow," *Physics of Fluids (1994-present),* vol. 23, p. 046101, 2011.
[74] D. Hill, C. Pantano, and D. Pullin, "Large-eddy simulation and multiscale modelling of a Richtmyer–Meshkov instability with reshock," *Journal of fluid mechanics,* vol. 557, pp. 29-61, 2006.
[75] J. A. Mcfarland, "Experimental and Computational Study of the Inclined Interface Richtmyer-Meshkov Instability," 2013.
[76] J. J. Charonko and P. P. Vlachos, "Estimation of uncertainty bounds for individual particle image velocimetry measurements from cross-correlation peak ratio," *Measurement Science and Technology,* vol. 24, p. 065301, 2013.

[77] Z. Xue, J. J. Charonko, and P. P. Vlachos, "Particle image velocimetry correlation signal-to-noise ratio metrics and measurement uncertainty quantification," *Measurement Science and Technology,* vol. 25, p. 115301, 2014.
[78] B. Collins and J. Jacobs, "PLIF flow visualization and measurements of the Richtmyer–Meshkov instability of an air/SF6 interface," *Journal of Fluid Mechanics,* vol. 464, pp. 113-136, 2002.
[79] G. Peng, N. J. Zabusky, and S. Zhang, "Vortex-accelerated secondary baroclinic vorticity deposition and late-intermediate time dynamics of a two-dimensional Richtmyer–Meshkov interface," *Physics of Fluids (1994-present),* vol. 15, pp. 3730-3744, 2003.
[80] M. Latini, O. Schilling, and W. S. Don, "Effects of WENO flux reconstruction order and spatial resolution on reshocked two-dimensional Richtmyer–Meshkov instability," *Journal of Computational Physics,* vol. 221, pp. 805-836, 2007.
[81] P. Ramaprabhu and M. Andrews, "Experimental investigation of Rayleigh–Taylor mixing at small Atwood numbers," *Journal of Fluid Mechanics,* vol. 502, pp. 233-271, 2004.
[82] V. Smeeton and D. Youngs, "Experimental investigation of turbulent mixing by Rayleigh-Taylor instability (part 3)," *AWE report number 0,* vol. 35, p. 1987, 1987.
[83] G. Berkooz, P. Holmes, and J. L. Lumley, "The proper orthogonal decomposition in the analysis of turbulent flows," *Annual review of fluid mechanics,* vol. 25, pp. 539-575, 1993.
[84] W. H. Cabot and A. W. Cook, "Reynolds number effects on Rayleigh–Taylor instability with possible implications for type Ia supernovae," *Nature Physics,* vol. 2, pp. 562-568, 2006.
[85] B. Balakumar, G. Orlicz, J. Ristorcelli, S. Balasubramanian, K. Prestridge, and C. Tomkins, "Turbulent mixing in a Richtmyer–Meshkov fluid layer after reshock: velocity and density statistics," *Journal of Fluid Mechanics,* vol. 696, pp. 67-93, 2012.